

©2011

ROBERT M PASTERNAK

ALL RIGHTS RESERVED

DEVELOPING A TIME-DYNAMIC, LABEL-FREE ASSAY FOR APOPTOSIS BASED
ON OPTICAL GABOR FILTERING

By

ROBERT M PASTERNAK

A Dissertation submitted to the

Graduate School-New Brunswick

Rutgers, The State University of New Jersey

and

The Graduate School of Biomedical Sciences

University of Medicine and Dentistry of New Jersey

in partial fulfillment of the requirements

for the degree of

Doctor of Philosophy

Graduate Program in Biomedical Engineering

written under the direction of

Nada N. Boustany

and approved by

New Brunswick, New Jersey

May, 2011

ABSTRACT OF THE DISSERTATION

Developing a Time-Dynamic, Label-Free Assay for Apoptosis Based on

Optical Gabor Filtering

by ROBERT M PASTERNAK

Dissertation Director:

Nada N. Boustany

Apoptosis is a fundamental process in the homeostasis and development of mammals, dysfunction of its regulation is implicated in human disease, and it is of growing interest as a possible therapeutic target (especially in cancer). An apoptosis assay that is sensitive, quantitative, and label-free would therefore be useful in cancer drug discovery by offering a direct, time-dynamic in-situ assessment of apoptotic response to drug candidates.

This thesis documents the development of optical Gabor filtering into an apoptosis assay. Optical Gabor filtering was developed as an improvement to optical scatter imaging (OSI) capable of optical scatter-based detection of object size and aspect ratio without the need for a predictive scatter model or extrinsic labeling. Two versions of the optical Gabor filtering instrument (LCD-based and DMD-based). By applying a series of Gabor filters with varying spatial frequencies and orientations, a series of filtered images can be generated and processed to extract morphological parameters of interest. The parameters of size, orientedness and aspect ratio are developed and tested using polystyrene microspheres, marine diatoms and collagen gelation, respectively. Orientedness and aspect ratio are employed as morphometric parameters to study dynamic morphological alterations in apoptosis.

Aspect ratio measurements in apoptotic iBMK cells show a differential aspect ratio response to apoptosis induction by bax/bak expressing and bax/bak knockout cell variants. To determine the biological source of these variations, multimodal image acquisition of fluorescently-labeled mitochondria alongside Gabor filtered data is used in apoptotic endothelial cells. Results of this study show a drop in orientedness 1-2 h post-STS treatment in mitochondria-rich regions (reconnoitered by fluorescence) concomitant with mitochondrial fragmentation but absent elsewhere. This dynamic is similar but not identical to that observed from iBMK cells. OSI imaging of apoptotic BAEC also revealed that a previously reported drop in optical scatter image ratio in the first hour of apoptosis is also associated with mitochondria-rich regions. In the future, the differences between optical responses of BAEC and iBMK apoptotic cells will be elucidated with fluorescent tracking of mitochondria-rich areas in iBMK. Classification and other computational methods could also be employed to directly evaluate the optical Gabor-filtered data in the future.

ACKNOWLEDGEMENT

I walked this journey called a dissertation for four years with friends and family, mentors and colleagues. I had the privilege to meet new people, and explore new places, and most of all, I had the opportunity to challenge my intellectual growth. I haven't made this journey alone, and I have a great many people to thank for walking with me along the way.

I would not be here were it not for my advisor, Dr. Boustany. Nada has been a constant companion in the evolution of my thesis, and she has steadfastly supported and encouraged me to persevere through my doubts, frustrations and exhaustions. Thank you Nada for the faith you have shown in me, and for all the reminders of the faith I keep in myself. I simply would not have been able to get here otherwise.

I am grateful to my other committee members, Drs. Yarmush, Metaxas, and White, for your feedback, ideas and encouragement. I am also indebted to all of the people who have blazed the trail before me, and have generously donated their time, resources and effort to help me in my work. Jing-Yi Zheng, thank you for teaching me everything I really needed to know to survive graduate school (and align the DMD!). Kevin Bray, thank you for your expert tumor tissue preparations and patient care of the vivarium mice. Shirley Masand, thank you for trying every possible (and some impossible) collagen preparations. Andrew Voyadjis, thank you for reminding me that I am still a social creature, and for the occasional game

of racquetball when I really needed to let off steam. Neel Shah, thank you for your tireless maintenance of our cells and our lab when I was drowning in my thesis. Bryan Rabin, thank you for automating our setup. Without you, I surely would have "clicked" myself to an early grave. Indeed, there are so many others to thank, and there are many more that I do not even know personally that deserve recognition. To them, I say simply and sincerely: Thank you for being a part of my journey. You helped, and it mattered.

I cannot end without acknowledgement of my family. My father, Sheldon, my mother, Linda, and my brother, Joe, have all been there through the best and the worst of it. You were the behind-the-scenes support beneath the soles of my feet that kept me on steady ground. I am grateful now more than ever that I have you in my life as I begin my next journey. You are my greatest strength, and limitless source of support, and it is to you whom I dedicate this dissertation.

TABLE OF CONTENTS

TITLE.....	Error! Bookmark not defined.
ABSTRACT OF THE DISSERTATION	ii
ACKNOWLEDGEMENT	iv
TABLE OF CONTENTS.....	vi
Table of Figures	viii
Chapter 1 : Introduction and review of previous work	1
1.1: Apoptosis	1
1.2: Apoptosis Detection	5
1.2.1: Electron microscopy and electron tomography.....	5
1.2.2: Biochemical assays and fluorescence microscopy.....	6
1.2.3: Optical methods	9
Chapter 2 : Optical Design and Instrument Development	13
2.1: Optical Gabor filtering evolved directly from the OSI design.....	13
2.2: Optical Gabor filtering with a digital micromirror device.....	14
2.2.1: The DMD dictates the optical design.....	15
2.2.2: Implementing Gabor filtering with the DMD	19
2.2.3: Setup and alignment of the optical system.....	22
2.3: Optical Gabor filtering with a Liquid Crystal device	24
2.3.1: Description of Optical Setup	26
2.3.2: Description of the LCD.....	28
2.3.3: Gabor Filter implementation on the LCD.....	34
2.4: Discussion	37
Chapter 3 : Characterizing the optical setup: Sensitivity to change in object size and aspect ratio	39
3.1: Introduction.....	39
3.2: Phase mask (ideal narrowband sample).....	41
3.3: Polystyrene spheres (high-contrast spatially confined samples).....	44
3.4: Comparison with digital post-processing.....	51
3.4.1: Digital Post-processing of phase mask images.....	52
3.4.2: Digital Post-processing of polystyrene microsphere images.....	54
3.4.3: Applicability of the sensitivity measurements with polystyrene microspheres	56
3.5: Using Optical Gabor filters to detect aspect ratio.....	59
3.5.1: A straightforward metric of aspect ratio: Orientedness.....	60
3.5.2: Applying optical Gabor filters to highly oriented structures in Marine Diatoms	61

3.6: Demonstration of rapid Gabor filterbank acquisition with the LCD-based system: Collagen fiber formation—	63
3.7: Discussion	72
Chapter 4 : Detection of mitochondrial fission During Apoptosis with orientation-dependent optical Fourier filters	78
4.1: Changes in Gabor filter response during apoptosis are spatially associated with mitochondria	79
4.1.1: Materials & Methods	79
4.1.2: Results	87
4.1.3: Discussion	96
4.2: High Time-Resolution study of Apoptosis	99
4.2.1: Cell Preparation and Optical Setup	99
4.2.2: Data acquisition and analysis	100
4.2.3: Results and Discussion	101
4.3. Discussion:	104
Chapter 5 : Using optical Gabor filters to detect Differential response to apoptosis in native iBMK and iBMK bax/bak knockouts	106
5.1: Applying optical Gabor filters to measure texture and orientedness in native iBMK and iBMK bax/bak knockouts	106
5.1.1: Methods	108
5.1.2 Results	109
5.1.3 Discussion	111
5.2 Applying Gabor filterbanks to detect differential execution of apoptosis in native iBMK and bax/bak iBMK knockouts	113
5.2.1 Methods	114
5.2.2 Results	117
5.2.3: Discussion	127
4.3 Discussion	129
Chapter 6 : Optical scatter imaging at the onset of apoptosis	131
6.1: Introduction	131
6.2: Methods	132
6.3: Results	134
6.4: Discussion	137
Chapter 7 : Summary & implications for further research	140
7.1: Summary	140
7.2: Implications for future research	143
7.3: Long-term outlook	145
References	149
CURRICULUM VITAE	156

TABLE OF FIGURES

Fig. 2-1. (printed from Boustany et al., (72) with permission): OSI setup. The objective back focal plane F is projected out of the microscope to conjugate Fourier plane F' . The scattered light (gray beam) is used to image the specimen on the CCD. Transmitted light (black ray traces) is blocked at F' yielding DF. The inset shows the setup at the high NA and low NA OSI imaging configurations. ...	14
Fig. 2-2. Setup. The transform of the object is focused at F_0 , F_1 , and F_2 . The object image is focused at I_0 , I_1 , I_2 and I_{CCD} . A beam block at F_1 blocks the zeroth order. Analog filtering at F_2 is accomplished by applying a series of Gabor-like filters to the DMD. Printed from Pasternack et al. (80) with permission.	16
Fig. 2-3. Imaging the DMD TF. (a). The DMD TF when all mirrors are actuated "on." (b-d). The DMD TF for an iris passing light between mirror radii $R = 28$ and $R = 383$ with the CCD placed in-the-plane, backward out-of-the-plane, and forward-of-the-plane, respectively. (e-g). The DMD TF for an iris passing light between mirror radii $R = 28$ and $R = 150$ with the CCD placed in-the-plane, backward out-of-the-plane, and forward-of-the-plane, respectively.	19
Fig. 2-4. Description of a Gabor filter.	20
Fig. 2-5. Illustration of DMD implementation of Gabor filter. (a): Ideal Gabor Filter in k -space. (b): DMD approximation formed by overlay of binary concentric discs. (c): Overlapping profile views of (a) and (b). Printed from Pasternack et al. (80) with permission.	21
Fig. 2-6. Illustration of filter bank design. Top filter bank measures particle size at chosen angle φ . Bottom filter bank measures particle orientedness or orientation at chosen spatial frequency $1/S$	22
Fig. 2-7. Using a graticule imaged in DF with known line spacing (left) to calibrate the DMD and derive the spatial frequency increment per mirror. The diffraction pattern (right) is imaged in the presence of an iris ruler in which concentric tickmarks in the Fourier plane block the transmittance at regular mirror intervals.	23
Fig. 2-8. Laser illumination launch. Narrow-band laser light from a ~ 25 mW crystal laser is focused ($f = 100$ mm) onto a ground glass diffuser (DG20-120, Thor Labs, NJ) spinning at > 500 rpm. Diffused light is collected and collimated by an aspheric lens (A390 TM-B, Thorlabs, NJ), and coupled into a single mode fiber (BFL48-600, NA=0.29 Thor Labs) by an aspheric fiber collimator (F220FC B, Thorlabs). Fiber output is collimated using an $f = 15.3$ mm aspheric lens (F260FC-A, Thorlabs) and input to the microscope condenser through the field lens. Drawn by Dr. Boustany.	26
Fig. 2-9. Optical setup. Light from the laser launch in central Köhler configuration strikes the object O mounted on the inverted microscope which is imaged at I_1 , I_2 and I_3 ; Fourier planes of the object image occur at F_1 , F_2 , and F_3 . Spatial filtering occurs on the SLM at F_3 . A polarization beamsplitting cube (B-S) is placed to pass horizontally polarized light to the SLM and to transmit vertically polarized light from the SLM to the CCD. A horizontally oriented polarizer (P) is placed in front of the B-S to enhance vertical extinction. A beam block at F_1 blocks enhances the elimination of transmitted light. A field stop is placed at I_2	27

Fig. 2-10. LUT linearization. (a): Device gray level input vs. LUT value for that gray level. (b): Signal vs. gray level input. For both (a) and (b), device defaults are given by the gray traces while the corrected values are given by the solid traces.30

Fig. 2-11. Contrast ratio. (a): DC component with device beam block in position. Non-zero orders of diffraction are evident at the top and bottom of the image. (b): Contrast enhanced rendition of (a) demonstrating small amount of DC transmission. The intensity of zeroth order (adjusted for exposure and neutral density) was 0.958×10^3 CCD counts. (c): DC component with device beam block removed. The intensity of zeroth order (adjusted for exposure and neutral density) was 1.427×10^6 CCD counts. The orders of diffraction evident in (a) and (b) are dim in comparison to the DC component. For reference, DF images of the graticule responsible for diffraction pattern are inset in red (upper right) on each panel.30

Fig. 2-12. TF. (a): TF with 768 mirror aperture placed on LCD. An illustration of the aperture image placed on the LCD while collecting TF is inset in red (lower right). (b): TF from (a) contrast-enhanced dim regions in TF. (c): TF with 600 mirror aperture placed on LCD. An illustration of the aperture image placed on the LCD while collecting TF is inset in red (lower right). (d): TF from (c) contrast-enhanced to dim regions in TF. TF remains circular and symmetric indicating the absence of optical aberration from the LCD.33

Fig. 2-13. Point spread function. (left): Image of $0.217 \mu\text{m}$ polystyrene microsphere. (right): Signal trace through center of PSF (red line). No significant aberrations are noted.34

Fig. 2-14: Scaling the Gabor filter gray level to the LCD LUT. (a) 8-bit Gaussian corresponding to a Gabor filter with spatial frequency $1.11 \text{ cycles}/\mu\text{m}$ at Fourier orientation $\varphi = 90^\circ$. (d) The same Gabor filter whose graylevel is remapped to the new gray level values of the LUT.35

Fig. 2-15. Signal-to-noise ratio of unfiltered dark-field signal from iBMK cells. Signal plot corresponds to signal across red line segment in image.36

Fig. 2-16. Signal-to-noise ratio of Gabor filtered ($S = 0.6 \mu\text{m}$, $\varphi = 135^\circ$) dark-field signal from iBMK cells. Signal plot corresponds to signal across red line segment in image. ROI corresponds to same ROI as given in **Fig. 2-15**.36

Fig. 3-1. Representative phase mask images. (a) Bright field taken at $0.080 \mu\text{m}/\text{pixel}$. (b): Bright field taken at $0.205 \mu\text{m}/\text{pixel}$. (c): Gabor-filtered image filtered at mask frequency, showing the edge of the condenser field stop and taken at $0.275 \mu\text{m}/\text{pixel}$. Optically filtered images were used for optical processing. (d): Representative plot and fit of signal in a single pixel of a series of filtered images...41

Fig. 3-2. Illustration of DMD implementation of Gabor filter bank and subsequent processing shown here for a phase mask data set. (a): Gabor-like filter bank applied to optical object transform in k-space. (b): Resultant stack of Gabor-like filtered images. (c): Representative fit of filter response as a function of Gabor filter frequency at one pixel of the image stack. Squares represent data points, the solid line represents the fit, and the dashed line represents the residual. (d): Morphometric-encoded image generated from fit for all pixels in the image. The color scale indicates the Gaussian mean resulting from the pixel response fit and thus gives at each pixel the optimum Gabor filter frequency, $1/S_{\text{max}}$, giving maximum response.43

Fig. 3-3. Optical Gabor filtering of phase masks. (a): Left to right: Color-coded images encoding measured phase mask frequency pixel-by-pixel from optical Gabor-like filtering at locations 1 mm, 3mm and 5mm from arbitrary starting point $x_0=0$ on chirped phase mask. Highlighted regions of

each image represent ROI used for analysis (pixel rows 80-446 and columns 65-446 of images). (b): Measured chirp as a function of displacement along the chirped (black diamonds) and unchirped (gray squares) phase masks imaged at $0.275 \mu\text{m}/\text{pixel}$ using Gabor-like optical filtering. Data are mean \pm standard deviation of the pixel values included in the processed regions of interest (ROI) (e.g. highlighted regions within the color encoded images in panel (a))......44

Fig. 3-4. Experimental Gabor filter bank response to finite objects (polystyrene microspheres) at low magnification ($0.275 \mu\text{m}/\text{pixel}$) with 20x objective. (a): Representative Dark Field (DF) ROI ($0.465 \mu\text{m}$ spheres) in polyacrylamide gel. (b): Differential Interference Contrast Image of same ROI. (c): Representative Gabor-filtered image of ROI. (d): Optically processed image encoding optimum Gabor period S_{max} giving maximal filter response. (e): Processed image encoding Gabor filter bank response gated to DF intensity image from Panel (a). For both Panels (d) and (e), color hue encodes filter period S_{max} at which response is maximized and intensity encodes relative fit amplitude.45

Fig. 3-5. Representative Gaussian fits of Gabor filter response at one pixel for three sphere sizes below $1 \mu\text{m}$. Pixel is chosen from regions on which a sphere is present. Ordinate is relative signal intensity. Signal increases with increasing sphere size.47

Fig. 3-6. Histogram showing the distribution of Gabor filter periods S_{max} at which local response for each sphere is maximized for sphere sizes ranging from $0.465 \mu\text{m}$ to $1.053 \mu\text{m}$. Each sphere region is derived from the dark-field-gated responses48

Fig. 3-7. Linear fit (with intercept fixed at zero) to plot of S_{max} as a function of sphere diameter. Error bars on abscissa are standard deviation of sphere diameter according to sphere manufacturer specifications while error bars on ordinate are standard deviation of the measured mean S_{max} . For sphere diameter $\leq 1.826 \mu\text{m}$ taken at 20x and for sphere diameter $\leq 1.053 \mu\text{m}$ taken at 60x, the coefficient of correlation > 0.9949

Fig. 3-8. Simulation of Gabor “filter-fit” methodology. (a): Mie-Theory sphere scatter intensity profile generated for $0.548 \mu\text{m}$ diameter sphere with index ratio $1.56/1.33 = 1.20$ matching that of the sphere samples. Unpolarized light is assumed. (b): Two-dimensional un-normalized Gabor filterbank applied to scatter intensity profile. (c): Plot of signal output from each simulated filtered scatter intensity profile. Signal is normalized to total energy of scatter profile. Shot noise is added with a random vector whose magnitude is the square root of the signal for that simulated filtered scatter intensity profile. (d): Same as (a) but simulating $1.826 \mu\text{m}$ diameter sphere scatter intensity profile. (e): Applied Gabor filterbank as in (b). (f): Plot of signal output from each simulated filtered scatter intensity profile as in (c) for $1.826 \mu\text{m}$ diameter spheres.50

Fig. 3-9. Digital post-processing processing of chirped phase mask. Measured chirp is plotted as a function of displacement along the chirped phase mask imaged in bright field at $0.205 \mu\text{m}/\text{pixel}$ (black triangles) and $0.080 \mu\text{m}/\text{pixel}$ (gray squares) and digitally post-processed using Gabor digital filtering. Data are mean \pm standard deviation of the mask periods measured at the pixels included in the processed ROI's within the bright field images. The analyzed ROI's of the unfiltered bright field images were pixel rows 75-448 and columns 75-448.53

Fig. 3-10. Measurement of sphere size based on S_{max} values derived from digitally post-processed images. (a): Histogram derived from digital Gabor filter bank applied to dark field image. (b): Histogram derived from digital Gabor filter bank aligned to the axis of contrast applied to DIC image. (c): Histogram derived from digital Gabor filter bank misaligned with the axis of contrast

applied to DIC image. (d) & (e): Sphere diameter measured using Gaussian second derivative template-matching algorithm as processed by Qian for dark field and DIC images, respectively.56

Fig. 3-11. Relative intensity of sphere scatter profile as a function of scatter angle for a sphere of 0.548 μm in diameter with $m = 1.04$ (green curve), $m = 1.12$ (black curve), $m = 1.20$ (red curve), and $m = 1.28$ (yellow curve). Incident light is unpolarized; scatter profiles are cylindrically symmetric....58

Fig. 3-12. Marine diatom samples for sensing oriented structures. (a): Dark field image of diatom. (b): Object orientation image. Color scale indicates degree of orientation (aspect ratio) while brightness encodes significance of the total Gabor filter response. (c): Orientation of objects with response intensity 10% of maximum. Line segment indicates the corresponding structure's long axis.63

Fig. 3-13. Representation of the single-pixel Gabor filter response in α, y, z defined by the Gabor filter parameters θ and φ66

Fig. 3-14. Representative data (orange) arranged into spherical configuration based on (θ, φ) of the Gabor filters and corresponding principal components (blue) calculated from PCA analysis.67

Fig. 3-15. Collagen gelation visualized using PCA analysis on Gabor filter signal. Left panels are unfiltered DF while right panels are encoded for aspect ratio (hue) and overall response amplitude (brightness) based on pixel-by-pixel PCA analysis. Responses are scaled according to Little structure is apparent at $T = 0$ (a). As time progresses, structures appear and brighten (b,c), and by 10 minutes the process is largely complete.70

Fig. 3-16. Time trace of aspect ratio during collagen gelation Only pixels of $>10\%$ maximum response are included.....71

Fig. 3-17. Local analysis collagen gelation ROI. (a): DF image of collagen sample at $T = 0$. (b): DF image of collagen sample at $T = 10$ min. Local neighborhood of ROIs studied is given by orange squares in the center top of (a) and (b). (c): Local neighborhood of (a) in DF (left panel), filtered image for Gabor filter with $S = 0.9 \mu\text{m}$, $\varphi = 60^\circ$ (center panel), and filtered image for Gabor filter with $S = 0.9 \mu\text{m}$, $\varphi = 150^\circ$ (right panel) at $T = 0$. Orientation of the respective filters are given by the yellow arrows (Center and Right panels, respectively). (d): Local neighborhood of (b) as in (c) at $T = 10$ min. Orientation of the respective filters are given by the yellow arrows (Center and Right panels, respectively). The pair of filters highlights different structures in the DF image. Red boxes in (c), (d) constitute 5×5 pixel ROIs for which polar plots of signal are rendered in (e-h). (e): Polar plot of signal from upper left ROI in (c) highlighting structures oriented at 60° at $T = 0$. (f): Polar plot of signal from upper left ROI in (c) highlighting structures oriented at 150° at $T = 0$. (g): Polar plot of signal from upper left ROI in (d) highlighting structures oriented at 60° at $T = 10$ min. (h): Polar plot of signal from upper left ROI in (d) highlighting structures oriented at 150° at $T = 10$ min.71

Fig. 4-1. Mounting the cells for imaging. The steel plate is machined with a 1 cm centered hole with channels halfway through the plate on either side of the hole. The top coverslip is mounted first with vacuum grease. The coverslip with live cells facing the inside of the chamber is then mounted on the bottom (Underside View) with vacuum grease. Medium is inserted into the space between coverslips by pipette. Finally, a layer of VaLaP is applied to the edge of the bottom coverslip to form a watertight and rigid seal.....81

Fig. 4-2. Optical setup and data processing. The light scattered by the sample is Fourier-filtered by the DMD (Inset 1). The stack of filtered images (Inset 2) collected on the CCD is processed pixel-by-

pixel and results in morphometrically encoded images (color-coded image) of the object that can be registered directly with the fluorescence and DIC images (Inset 3). Masks segregating bright fluorescent regions from dim ones for each cell ROI at each time point (Inset 4) allow study of orientation dynamics within regions dominated by mitochondria and those dominated by non-fluorescent subcellular structures (Inset 5).83

Fig. 4-3. Fluorescence image processing. The raw fluorescence image (A) is filtered with a lowpass filter. This generates a background image (B) which is then subtracted from the original image to generate a high-contrast mitochondrial fluorescence image (C). A digital Gabor filterbank with the same orientations, period and Gaussian envelope as the DMD Gabor filters used in the optical setup is applied to the background-corrected fluorescence image to yield a fluorescence image with the same spatial resolution as the optically filtered images (D).86

Fig. 4-4. Orientedness derived from Gabor-like filter responses for BAEC studied at low resolution (objective NA=0.75, 0.625 $\mu\text{m}/\text{pixel}$). A: Images of BAEC exposed to STS taken -60 min, 20 min, 120 min. and 180 min. from STS exposure ($T=0$). Top: DIC. Middle: Fluorescence images of labeled mitochondria. Little difference in mitochondrial morphology is discernible at these time points at low resolution. Despite this, the morphometric images encoding orientedness (color scale in bottom panels) report a decrease in orientedness as a function of time after STS addition. B, C: Time traces plotting the mean orientedness within individual cells treated with STS (gray traces in B) or DMSO (gray traces in C). In B-C, the solid bold black trace represents the mean \pm standard deviation of the individual gray traces. The data were normalized to $T=-120$ min.88

Fig. 4-5. High resolution study of BAEC exposed to STS (objective NA= 1.4, 0.195 $\mu\text{m}/\text{pixel}$). A: Images of BAEC exposed to STS at -60 min, 20 min, 120 min. and 180 min. from STS exposure ($T=0$). Top: DIC. Middle: Fluorescence images of labeled mitochondria. Arrows point to fragmenting mitochondria. Bottom: Morphometric images encoding orientedness (color scale) reporting decrease in orientedness as a function of time after STS addition at $T=0$89

Fig. 4-6. Time traces plotting the mean orientedness within individual cells tested at high resolution (objective NA= 1.4, 0.195 $\mu\text{m}/\text{pixel}$) and treated with STS (gray traces). Bold black trace with solid squares represents the mean \pm standard deviation of the gray traces of cells exposed to STS. The blue trace with open circles corresponds to the average orientedness per cell \pm standard deviation as a function of time for DMSO control. The STS data were normalized to $T=-180$ min.; the DMSO data to $T=-200$ min.89

Fig. 4-7. Effect of threshold level on separating dynamics of fluorescent and nonfluorescent regions within cell ROIs at high resolution (objective NA= 1.4, 0.195 $\mu\text{m}/\text{pixel}$). A representative cell from the center of the field of view shown in **Fig. 4-5** is illustrated here. A-F show the fluorescent (above threshold, left) and non-fluorescent (below threshold, right) region pairs generated by applying a threshold to the corresponding Gabor-resolved fluorescence image (**Fig. 4-3d**). The time traces for normalized mean orientedness evaluated within the designated fluorescent mask (above threshold, solid black line) and the non-fluorescent mask (below threshold, dashed line) are shown below the corresponding binary mask images. The threshold level, T_h , is given as a fraction of the average fluorescence signal within the cell ROI (e.g. $T_h = 2.0$ indicates that twice the average of the intensity of the Gabor-resolved fluorescence images within that ROI was used to generate the region pair). .91

Fig. 4-8. A-B: Time traces plotting orientedness for the bright, above-threshold fluorescent regions (A) and for the dim, below-threshold regions (B) within individual STS-treated cells (gray traces). The average fluorescence intensity in the processed fluorescence image defined the threshold value within

each cell and corresponds to $T_h=1$ (see also **Fig. 4-7**). Bold black trace with solid squares represents the mean \pm standard deviation of the gray traces of cells exposed to STS. Blue trace with open circles corresponds to the mean \pm standard deviation for DMSO control (average of all cells). C-D: Normalized number of non-contiguous fluorescent regions counted in the above threshold fluorescent mask generated at high resolution (Panel C, NA=1.4, 0.195 μ m/pixel) and at low resolution (Panel D, NA=0.75, 0.625 μ m/pixel) with $T_h=1$. The rise in the number of fluorescent regions beyond $T = 60$ min. is statistically significant ($p < 0.05$) comparing average STS response with DMSO control at high resolution (C) but is not statistically significant ($p = 0.72$) at low resolution (D). In C-D, bold black trace represents the mean \pm standard deviation of the gray traces of cells exposed to STS. Dashed trace corresponds to the mean \pm standard deviation for DMSO control (average of all cells).....92

Fig. 4-9. Effect of movement on accuracy of masks. DIC (A) and fluorescence (B) image of BAEC labeled with Mitotracker green under experimental conditions taken immediately after STS exposure ($T = 0$ min.) and 10 minutes later. C: Color coded segments demonstrating how the segments within the ROI of a representative cell change over time. Each ROI is compared with the initial ROI at $T=0$ in order to quantify movement over a 10 minute time span. D: Time trace plotting the fraction of pixels that change between fluorescent and non-fluorescent regions over time. After an initial jump from zero to 5% by 1 minute, the error increases at a fairly constant rate of .4% per minute. Solid bold black trace represents the mean \pm standard deviation of the gray traces of cells exposed to STS in this experiment..... 94

Fig. 4-10. Immunofluorescence of cleaved caspase 3 in BAEC under experimental conditions. Representative DIC (A) and immunofluorescence (B) images of cells treated with STS (top) or DMSO (bottom) for 3 hours. C: Number of caspase 3 positive cells (dark gray) as a fraction of the total number of cells tested (light gray) for STS- and DMSO-treated cells. The ordinate cells/mm² is calculated by manually counting cells and normalizing to the area of the field of view measured with the aid of a stage micrometer. While small, the fraction of cleaved caspase 3 positive cells is significantly greater ($p < 0.01$) in the cells treated with STS than cells treated with DMSO. D: Relative fluorescence intensity distributions for the STS- and DMSO-treated cells. Cells with intensity greater than 50% the background intensity (0.11) were taken as positive for caspase 3 activation.95

Fig. 4-11. Dark-field (top panels) and optically processed images of a representative field of view just before and 180 min. after STS treatment. For a given filter period S (in μ m), orientedness (color scale) is taken as the ratio of maximum over average filter response as a function of filter orientation φ . The color brightness gives the total response at the filter period, S , summed over all angles..... 102

Fig. 4-12. Dark-field (top panels) and quiver plots (middle panels) showing the orientation angle of subcellular structures with filter responses at $S = 0.9 \mu$ m. The polar plots show representative data collected with the optical system. Filtered signal responses are shown as a function of filter period S and filter orientation φ for two 4x4 pixel regions (arrows) located in the cytoplasm (C) and nucleus (N) just before ($T = 0$), and 180 min. after STS treatment. 103

Fig. 4-13. Average orientedness per cell plotted as a function of time for filter responses at $S = 0.9\mu$ m. The data were normalized to the value at $T = -120$ min. STS or DMSO was administered at $T = 0$. Individual traces are shown for the STS-treated cells in the field of view tested in **Fig. 4-11** and **Fig. 4-12** ($N = 6$). The black line with solid black circles is the mean orientedness \pm 95% confidence interval of cells treated with DMSO ($N = 7$). 103

Fig. 5-1. W2 (bax/bak expressing) and D3 (bax/bak null) cells images. (a), (e): Differential interference contrast, (b), (f): Dark field (DF). Little difference can be discerned between the two cell types using these modalities. (c), (g): Object orientation as in **Fig. 3-12**. More highly oriented objects (red areas) are present in the W2 compared with the D3 cell. (d), (h) & F: W2 and D3 cell whose filtered images were block-processed to simulate a 4x demagnification before orientation analysis.

..... 110

Fig. 5-2. Pixel histogram of all W2 and D3 aspect ratios. A: Histogram for subcellular orientedness without block processing. W2 cells have a higher orientedness distribution ($p < 0.04$) than D3 cells. B: With 4x4 pixel block processing. W2 cells' higher orientedness distribution remains significant ($p < 0.05$). 111

Fig. 5-3. Illustration of orientation measurement from W2 and D3 images. (a) Differential interference contrast. (b) Dark-field. (c) Object orientation as in **Fig. 3-12**. (d) Orientation of objects with response intensity 15% of maximum. Line segment indicates the corresponding structure's long axis. 111

Fig. 5-4. (a): DF image of graticule. (b): Mask resulting from image segmentation routine applied to (a). (c): Representative field of iBMK cells under typical experimental conditions. (d): Mask resulting from image segmentation routine applied to (c). 117

Fig. 5-5. Representative dark-field (top panels) and morphometric-encoded images (bottom panels) of PCA-based aspect ratio of W2 cells treated with 0.5 μ M staurosporine at $t = 0$ (a), $t = 2$ h (b), and $t = 4$ h (c) after staurosporine is introduced. Color hue indicates orientedness and color saturation is scaled to response intensity (the relative cumulative signal intensity collected from all Gabor filters). Figures are scaled to intensity of Gabor signal response as in **Fig. 5-1**, **Fig. 7-1**, and **Fig. 5-3**. 118

Fig. 5-6. Representative time response of aspect ratio histogram for W2 (a) and D3 (b) cells exposed to STS. A significant ($p < 0.01$) rise at ~ 1 -2 h, and subsequent drop (3-6h) in aspect ratio is detected for the W2 cells while little response is noted for the D3 cells. Number of W2 cells (N_{W2}) and D3 cells (N_{D3}) are ~ 30 each. 119

Fig. 5-7. Mean normalized aspect ratio time response of (a) apoptosis competent (W2) and (b) apoptosis resistant (D3) iBMK cells. W2 time response is normalized to maximum aspect ratio ($t = 120$ min.). All other time responses are normalized to first time point ($t = 0$). Due to difficulty in counting unlabeled cells in a confluent culture in DF, number of cells is approximate and is based on average cell density for preparation conditions. 119

Fig. 5-8. JC-1 time lapse imaging. DF images (left column of image panels, exposure time 50 ms), red JC-1 fluorescence (middle column, exposure time 200 ms) and green JC-1 fluorescence (right column, exposure time 200 ms) of W2 cells labeled with 1 μ g/mL JC-1 under experimental conditions, without STS treatment. Imaging commenced at $T = 0$ (a) immediately after mounting the cells to the microscope stage. At this time point, healthy polarized mitochondria are abundant as evidenced by the numerous bright, punctate regions in (a, center panel). After 30 minutes (b), 1 hour (c) and 2 hours (d) of imaging, the cells steadily deteriorate. The DF presentation worsens as the cytoplasm becomes less distinct and structured and the cell nuclei shrink markedly. This is accompanied by an almost total disappearance of bright punctate regions of red fluorescence (center column) indicating a commensurate loss of mitochondrial potential. 123

Fig. 5-9. DF images (left, exposure time 50 ms), red JC-1 fluorescence (center, exposure time 200 ms) and green JC-1 fluorescence (right, exposure time 200 ms) of W2 cells labeled with 1 μ g/mL JC-1

under experimental conditions, without STS treatment. The field of view shown is adjacent to the one imaged in **Fig. 5-8**. The edge of the field irradiated for time lapse imaging lies approximately halfway up from the bottom of the DF image. The bottom cells (irradiated in time lapse) closely resemble the appearance of those in **Fig. 5-8** after the time lapse while the cells in the top portion of the image (not irradiated in time lapse) resemble the W2 cells in **Fig. 5-8a** at the start of imaging ($T = 0$). The cells not imaged in time lapse (top) also have similarly high levels of red fluorescence in bright, punctate regions indicating healthy mitochondria (center panel)..... 124

Fig. 5-10. DIC montage of irradiated field of view and surrounding vicinity. Sample consists of W2 cells labeled with 50 nM mitotracker green in growth medium for 30 min at 38 °C, 8.5% CO₂ which was then subsequently given 200 ms of blue fluorescent excitation every 10 minutes over 12 h under experimental conditions. The time-lapse irradiated area (enclosed by red circle) is roughly 250 μ m in diameter. Cells within this area are highly deteriorated in comparison with cells removed from the circle. 124

Fig. 5-11. Fixed iBMK JC-1 fluorescence (a): DIC (left panel) and dual-channel fluorescence (right panel) in W2 cells at $T = 0$. Punctate red regions correspond to mitochondria with high membrane polarization (negative potential) and green diffuse areas correspond to areas of low potential. (b): DIC (left panel) and dual-channel fluorescence (right panel) in W2 cells at $T = 4$ h. Reduced red fluorescence indicates a generalized loss of mitochondria membrane potential consistent with apoptosis. (c): DIC (left panel) and dual-channel fluorescence (right panel) in D3 cells at $T = 0$. (d): DIC (left panel) and dual-channel fluorescence (right panel) in D3 cells at $T = 4$ h. In contrast to W2 (B), no reduction in membrane potential as reported by JC-1 is noted after 4 h STS treatment. 126

Fig. 6-1. Top row: fluorescence (left), OSI (middle), and differential interference contrast (right) images of a representative cell immediately after 1- μ M STS treatment at (a) $T=0$, (b) $T=40$ min, and (c) $T =140$ min after STS addition. Bottom row: magnified fluorescence and OSI insets showing mitochondrial fragmentation (arrows)..... 134

Fig. 6-2. OSIR change as a function of time for STS (black diamonds) and DMSO (white diamonds) treated cells. The value at each time point is the mean OSIR per cell normalized to the mean OSIR per cell at $T=-120$ min. Error bars indicate \pm the 95% confidence interval of the mean. STS (1 μ M) or DMSO was added at $T=0$ 135

Fig. 6-3. (a) Representative raw fluorescence image (top panel) and Gabor filtered fluorescence image (bottom panel) used for thresholding study (images are shown for $T=-60$). (b) Representative binary subcellular masks (shown for one cell) with fluorescence intensity above ($>Th$) or below ($\leq Th$) threshold. The threshold value (Th) was normalized to the average fluorescence intensity within a given cell segment. (c) and (d) Mean OSIR per masked cell $\pm 95\%$ confidence interval as a function of time in the subcellular regions with fluorescence above threshold (filled squares) or below threshold (open squares). Data are shown for (c) STS and (d) DMSO treated cells, and for different values of Th 136

Fig. 7-1. iBMK-W2 tumor tissue studied with orientedness detection Gabor filter bank to detect effect of staurosporine in time lapse. A: DIC ($T = 0$ min.) and processed images ($T = 0$ min. and $T = 180$ min.) produced as in **Fig. 3-12**. For tissue exposed to 0.8 μ M staurosporine (STS). B: For tissue exposed to DMSO only (no STS). C: Plot showing time dependency of particle orientedness for each of the three STS concentrations. Particle orientedness decreases when exposed to STS and does not when exposed to a control lacking STS. 147

CHAPTER 1 : INTRODUCTION AND REVIEW OF PREVIOUS WORK

1.1: APOPTOSIS

Apoptosis is a highly conserved process of programmed cell death exhibited in multicellular eukaryotes (1). Physiological, pathological and environmental stimuli can trigger the apoptotic process leading to characteristic changes in cell morphology and finally the destruction of the cell. Apoptosis is also characterized by specific biochemical events which guide this process. It is a physiological and homeostatic process which provides advantage to multicellular organisms, including normal cell replacement (acting as a counterbalance to mitosis), immune response, and development. Dysregulation (either upward or downward) is a primary factor in human disease, and therefore apoptosis has been a subject of vigorous and rapidly expanding research interest.

Unlike traumatic cell death (necrosis), the processes of apoptosis are homeostatically regulated and are generally of no harm to the organism (in fact, they can be of significant benefit, such as the case in human development, as the tissues between the digits are removed by apoptosis of these cells, leaving separate digits behind (2)). Genetically damaged cells are eliminated through the apoptotic pathway (3). Apoptosis is executed with exquisite precision; of the 1090 somatic cells generated in the development of the adult *Caenorhabditis elegans*, 131 undergo apoptosis, dying at specific points throughout the developmental process. This phenomenon is essentially completely invariant between worms, and the number and order of cells dying is exact.

Undoubtedly, the process is mediated and regulated by a rich array of cell signals and pathways that originate either with extrinsic inducers (hormones, growth factors, cytokines)

or intrinsic inducers (in response to stress). Either transport of these factors across the plasma membrane or the transduction of the signal they carry must be executed in order for them to have any effect (which may be positive i.e. promoting apoptosis, or negative, i.e. repression of apoptosis) (4; 5; 6; 7).

In the intrinsic pathway, the regulation of the intrinsic pathway of the apoptotic process to great extent converges upon the mitochondria and is an area of extensive ongoing research. Mitochondria participate in the apoptosis signaling pathway through the release of cytochrome c (an essential protein for electron transport during oxidative phosphorylation) from the intermembrane space in response to apoptotic signals (4; 5; 6; 8). Pro-apoptotic factors include Bax and Bak which are themselves induced by oxidative stress, cellular damage, or signaling from the CD95 “death receptor” and the subsequent activation of Caspase 3 (6; 9; 10; 11). Bax and Bak promote the release of cytochrome c and collateral substances by increasing mitochondrial outer membrane permeability. As cytochrome c is leaving the mitochondria, it activates Apaf-1, which then activates Caspase 9 by phosphorylating pro-Caspase 9 in the cytosol. Caspase 9 in turn activates Caspase 3, which activates Caspases 6 and 7, which are the effector caspases of apoptotic destruction of the cell. Also, activated Caspase 3 activates the pathway through which chromatin is condensed and DNA fragmented. For this reason, the activation of Caspase 3 is considered to be the “point of no return,” beyond which the cell is committed to the fate of an apoptotic death. In parallel to the Caspase cascade, the apoptosis inducing factor (AIF) pathway may be activated, directly effecting apoptotic death. The AIF pathway is active during development and is Caspase-independent (12).

There are several regulatory checkpoints within the signaling pathway. Bcl-2 and Bcl-xL prevent mitochondrial pore formation by Bax and Bak, blocking mitochondrial outer membrane permeabilization and subsequent apoptosis (13; 14). The Inhibitor of Apoptosis protein (IAP) can inhibit the activation and function of Caspase 3 unless Smac/Diablo is also released from the mitochondrial lumen in concert with Cytochrome C (15).

Smac/DIABLO export from the mitochondria is induced by DNA damage, cytotoxic factors and by ligand-binding of the CD95 “death receptor” (15). In the extrinsic pathway, The Tumor Necrosis Factor (TNF) family receptor can directly induce activation of the Caspase cascade without the involvement of the mitochondria (i.e. without the release of Cytochrome C), but can also activate Bid another protein of the Bcl-2 family, which in turn induces the mitochondrial mediated apoptosis pathway (16). Several genetic modifications can be made to cells to study these pathways and their effect on cell morphology. For example, transgenic Bax/Bak double- knock-out cells are highly resistant to apoptosis even when exposed to high doses of cytotoxic substances such as staurosporine (17).

The morphology of apoptosis is notable in that it is very carefully regulated to prevent the uncontrolled release of cellular cytosolic and nuclear contents into the extracellular milieu. Rather, the apoptotic morphological cascade ultimately results in the orderly dismantling of the cells into self-contained apoptotic bodies that are then subsequently consumed by other cells. This gives apoptosis its distinctive lack of inflammatory reaction (18; 19). At the cellular level, apoptosis causes cellular shrinkage, increasing the organellar concentration within the cell. Later, chromatin condenses, and the nucleus shrinks and fragments. The cell blebs extensively, and the cell breaks down into apoptotic bodies contained by the cells original plasma membrane (20). During the course of apoptosis, SEM studies have revealed several distinct mitochondrial morphologies, ranging

from swelling and outer membrane rupture (21), mitochondrial shrinkage (22), blebbing (23), fission (6; 24; 25), proliferation (26), and cristae remodeling (27).

Mitochondrial changes also occur during the early stages of apoptosis in the context of bax/bak localization to the outer membrane. Mitochondria undergo inner and outer membrane fission under the control of dynamin related proteins, which can interact with Bcl-2 family proteins during apoptosis. During apoptosis, truncated Bid (tBid) causes mitochondrial matrix vesicularization by disruption of OPA-1 oligomers, which control mitochondrial inner membrane fusion (25; 27; 28). tBid also affects bioenergetics, induces mitochondrial lipid peroxidation, and can activate Bax/Bak by interacting with cardiolipin (29; 30). In addition, mitochondria fragment during apoptosis under the control of Drp-1 and Fis1 (31; 32; 33). Strong evidence suggests that Drp-1 is critical for mitochondrial outer-membrane permeabilization and release of cytochrome c in the context of the intrinsic pathway (34). In particular, during apoptosis Bax translocates to mitochondria and coalesces with Drp-1 and Mitofusin 2 (Mfn-2) at mitochondria fission sites (35), however the relationship between Bax and Drp-1 is not yet fully clear. Bax seems to be required to stabilize Drp-1 localization on the mitochondria (36) and inhibition of Drp-1 inhibits Bax-mediated cytochrome c release and apoptosis (31; 37). Drp-1 may also be involved in Bax oligomerization once Bax inserted into the mitochondrial outer membrane (38).

Additionally, emerging evidence suggests that mitochondrial fragmentation may occur after mitochondrial outer membrane permeabilization by bax/bak. Arnoult et al. (39) show that Drp-1 activation may proceed retroactively from DDp/Timm8a (an mitochondrial intermembrane space protein) release after permeabilization. Additionally, fluorescence recovery after photobleaching studies reveal that the stable association of Drp-1

to the mitochondrial outer membrane occurs after Bax recruitment to the mitochondrial membrane but before loss of mitochondrial potential (36). Arnoult et al. also propose that Opa-1 (also released from the intermembrane space after permeabilization) may be similarly recruited to fragment the mitochondrial network (40). However, Scorrano et al. provides evidence that OPA-1 is involved in inner membrane fusion but does not necessarily act on the outer membrane (41). If mitochondrial outer membrane permeabilization does indeed occur upstream of mitochondrial fragmentation, and mitochondrial fragmentation requires intermembrane space factors, then mitochondrial fragmentation may be one of the earliest post-commitment morphological events in the apoptotic process, and is therefore of great interest in this thesis.

1.2: APOPTOSIS DETECTION

The methods used to study apoptosis are varied and range from direct optical imaging, electron microscopy (EM), biochemical assay, flow cytometry, fluorescence microscopy (FM), and optical scatter measurements (OSM), and have been implemented in living cells, fixed samples, and isolated organellar suspensions. Direct imaging offers the most cursory level of examination, while the others have higher sensitivities. In this section, the advantages and disadvantages of each will be discussed as a primary motivating factor in applying the optical Gabor filtering method.

1.2.1: ELECTRON MICROSCOPY AND ELECTRON TOMOGRAPHY

EM allows very high resolution imaging (nanometer scale) but requires sample fixation and destruction of the living cell. Nonetheless, more recent advances in electron tomography (42) allows three-dimensional shape reconstruction of pleomorphic structures

such as mitochondria, and has been used to characterize gross structure, 3-dimensional shape, and its implications for mitochondrial function (43; 44; 45).

Apoptosis detection with EM utilizes the very high spatial resolution of EM in order to directly image the morphological changes (blebbing, chromatin condensation) associated with apoptosis. Generally, detection of apoptosis with EM is most effective for late-stage apoptosis after these hallmark morphological changes have already taken place. The morphological changes associated with early apoptosis are much more subtle, and EM has been used in only limited fashion in this context (46). However, with sufficient care, EM can be used to distinguish end-stage apoptosis from necrosis by looking for intact organelles within the apoptotic bodies and comparing those with the disrupted organelles found in necrosis (47).

Although a very powerful method, high cost, low throughput and the inherent need for fixation (with the loss of dynamic study and the possible introduction of fixation artifacts) limit the usefulness and availability of this method. Additionally, EM provides only limited insight into the underlying biological mechanisms that drive the morphology. As a result, EM is accompanied by chemical detection methods designed to detect reporter molecules heralding apoptosis.

1.2.2: BIOCHEMICAL ASSAYS AND FLUORESCENCE MICROSCOPY

Biochemical apoptosis assays rely on activation of a reporter molecule, which are typically activated after a key biological event that makes the target ligand for the reporter available. For example, annexin V can be used to bind phosphatidylserine as it is exposed to the outer plasma membrane after the loss of membrane potential asymmetry in apoptosis with the help of flow cytometry (48). Staining can also be done on cells that have been

plated and fixed by labeling for nuclear DNA fragmentation with H&E staining. Fragmented DNA in compromised nuclei results in a diffuse stain whereas intact DNA yields a stain confined to the nucleus (49). The TUNEL fluorescence assay can also be used to detect fragmented DNA more specifically, but cannot discriminate between apoptotic, autophagitic or necrotic pathways (50). Combination stains can be used to study the progressive events of apoptosis *in situ* (51). Although their ability to infer biologically specific information is their greatest advantage, the throughputs of such assays are typically low, they are not always amenable to study of living cells, and thus can be time-consuming and expensive to use in large studies.

Electrophoretic methods can be used to detect the presence of cleaved DNA resulting from chromatin condensation. DNA fragmentation occurs during late-stage apoptosis, but can be detected very accurately using a comet assay (47; 52). The comet assay uses gel electrophoresis of whole cells encapsulated in agarose and lysed by alkaline or detergent treatment *in situ*. Damaged DNA leaks out of the cell upon electrophoresis (resulting in a trail of DNA from the cell resembling a comet) while intact DNA does not. The amount of leakage and the degree of fragmentation can be quantified based on the characteristics of the DNA "comet tail." Protein-based apoptosis analyses typically measure the presence of cytochrome C in the cytosolic milieu, the concentration of regulatory proteins, and activated caspases. Western blotting techniques are extremely sensitive, allowing for the detection of cytochrome C release in as little as 30 minutes post-induction in some cases (53). The earliest possible detection of the reporter is in general desirable because of the improved time resolution that can be achieved. This information can then be used to generate an improved understanding of the time dynamics involved in the process.

Because of the sensitivity of electrophoretic methods, they will continue to play a major role in apoptosis research. However, like EM, their use requires the destruction of the

cell in order to retrieve the information sought. Therefore, other methods are employed to detect apoptosis in intact cells.

Fluorescence detection is perhaps the most flexible and popular method for apoptosis detection. It is extremely versatile, fairly sensitive, and in many (but not all) cases, can be used to measure apoptotic events in living cells over long periods of time. Generally, two versions of fluorescence detection are currently employed: flow cytometry and fluorescence microscopy (FM).

Flow cytometry (54) offers the ability to rapidly measure the fluorescence from living cells and thus represents a high throughput yet chemically sensitive and specific measurement. By tailoring the fluorescent label to bind to specific ligands, flow cytometry can be used to ascertain the concentration of almost any apoptosis reporter desired. For example, annexin V-FITC labeling can be used to differentiate apoptosis from necrosis in living cells (47).

Flow cytometry also allows the user to rapidly count and even sort cells depending on the presence or absence of a reporter above a set threshold. However, the analysis represents a snapshot of the cellular system and time lapse study usually requires repetition of the analysis at independent time points from different samples. Therefore, when morphological detection, in-situ observation, and time lapse studies are required, the techniques mentioned here are usually accompanied by some form of FM.

FM offers a very versatile and powerful alternative using fluorescent labeling at optical resolutions. This technique may be applied to either fixed or living cells, allows for a higher throughput than EM, and can be done in-situ unlike many biochemical assays. For example, mitochondria are typically labeled with a mitochondrial-targeting fluorescent protein such as mitochondrial matrix-targeted-GFP (mito-GFP) or -DsRed2 (mito-DsRed2)

(55) that allow for high signal-to-noise acquisition. Then, morphology may be measured with 3-D reconstruction from serial confocal images and digitally post-processed (25; 56; 57). This method is very versatile, having been used in applications ranging from the study of morphogenesis (56) and disease states (57) of the synapse and neuronal processes (51) to measuring shape change and mitochondrial involvement in apoptosis (25). Fluorescence recovery after photobleaching (FRAP) (58) shows great promise in analyzing movement and transport within mitochondria by diffusion tracking, and has already been used to assess the rate of mitochondrial fusion and the degree of mitochondrial networking in cells lacking the pro-apoptotic proteins Bax and Bak (9). Highly sensitive quantitative study of subcellular morphology using FM requires high resolution imaging with magnifications that limit acquisition throughput analysis beyond at best a handful of cells at a time (59). High throughput study is possible, but applications are limited to low resolution screenings with coarse structural compartment distinctions such as nucleus, cytoplasm, and extracellular space (60). Because this technique ultimately requires direct observation of the field of view, the target organelles must in any case be sufficiently resolved and magnified to detect the morphology being probed. Therefore, although throughput is much higher than in EM, it remains a significant limitation of FM.

To combat the collective limitations of labeling, fixation, and sensitivity that are endemic to the standard apoptosis detection techniques given above, recent interest has grown in using optical methods to detect apoptosis.

1.2.3: OPTICAL METHODS

OSM of mitochondria and other subcellular components has also been extensively used. Measurements using scattering and spectroscopic detection are extremely powerful

and sensitive in measuring spherical particle size accurately even for particles sized below the diffraction limit (61; 62). Angularly resolved light scattering with a layered Mie theory sphere model has improved the traditional Mie theory models dramatically in detection of mitochondrial swelling from intact cells and cell lysates (63). Angular scattering spectroscopy has proven very useful in studying other mitochondrial dynamics in living cells (64; 65) and has been applied to living cells to measure other organelles (66).

Reflectance OSM methods such as Optical Coherence Tomography (OCT) (67) have been used as well, and OCT has a better depth penetration over other methods measuring reflected scattered light such as confocal microscopy (68). Therefore, optical study of thick tissues (69; 70; 71) is possible with OCT. The difference between the optical Fourier filtering technology used in developing a morphological assay and other OSM lies in the fact that this method does not rely on modeling of the scatter spectrum to extract physical morphological parameters and is capable of encoding these parameters onto an image that is directly registered with the primary field of view.

Optical Gabor filtering most closely resembles and is indeed a direct extension of a previous optical Fourier filtering technique known as Optical Scatter Imaging (OSI) developed by Boustany et al. (72) and utilized extensively by Zheng et al. to study mitochondrial morphology (73). OSI directly encodes angular-scatter information into a specimen image, and because it is an optical rather than a digital filtering technique, this method provides sensitivity to objects at the limit of microscope resolution despite digital undersampling of these particles in the image. OSI applies spatial filtering in a rudimentary way with an iris placed in a conjugate optical Fourier plane that essentially allows the investigator to vary the numerical aperture of the scatter plane. This allows the user to take a

ratio of two images taken with different apertures, thereby deriving the ratio of wide- to narrow-scatter intensity.

Many of the underpinnings of OSI still apply to the optical Fourier filtering technology used here. Both employ dark field imaging as the signal to be optically filtered, as the removal of transmitted light allows for study of scattered light only as the basis of study. However, a serious limitation to the OSI technique arises from calibration of the optical scatter intensity ratio (OSIR). Calibration of OSIR values requires a theoretical description of the optical scatter in question, in turn requiring an assumption of the shape of the objects being measured, and that a predictive scatter model exists for that shape (or its approximation). For example, Mie Theory can be used to calibrate OSIR values for spherical particles (72). Boustany et al. found that the optical scatter intensity ratio (OSIR) is monotonically decreasing for spheres with diameters between 0.2 μm and 2 μm , making this measurement a useful parameter in measuring change in object size for particles within this size range.

Boustany et al. used OSI Mie theory solution (and approximated all visualized particles as spherical) to study BCL-xL-dependent structural changes in mitochondria during apoptosis (74). Zheng et al. also took this approach to use OSI and fluorescence microscopy to show how genetic alteration of the Bcl-xL C-terminal transmembrane domain can alter apoptosis resistance (73). While these studies are promising, Zheng (75) established that OSIR cannot discriminate between changes in shape and changes in size. In the biological setting, this represents a fundamental limitation to how OSIR results may be interpreted, and motivates the need to design a new method with the advantages of OSI but with sensitivity to both size and shape as well.

Chapter 2 will describe the evolution of the optical Gabor filtering method from OSI and describe two versions of this system with different spatial light modulators. The characteristics use of each spatial light modulator (and the systems built around them), as well as the Gabor filter implementations will be described. Chapter 3 will present data characterizing the performance of the system in measuring changes in object size (using polystyrene microspheres), orientedness (using marine diatoms) and aspect ratio (using collagen gelation). The description and application of each morphometric parameter (size, orientedness and aspect ratio) will be given. This chapter will also confirm the time-lapse capability of automated Gabor filter acquisition using the collagen gelation experiment as a proof of principle. Chapter 4 presents a study of orientedness in endothelial cells treated with staurosporine and how this can be validated against fluorescence imaging of labeled mitochondria. The spatial distribution of changes in orientedness will be discussed. Chapter 5 describes a study of aspect ratio and mitochondrial membrane potential of immortalized baby mouse kidney (iBMK) cells (both bax/bak expressing and bax/bak knockout) treated with staurosporine. The differences and similarities between the aspect ratio dynamics measured in iBMK and orientedness in BAEC will be discussed. Chapter 6 presents an optical scatter imaging study of BAEC, extending previous work and using fluorescent imaging to establish the spatial distribution of OSI dynamics. Finally, Chapter 7 summarizes the results of this thesis, and discusses areas of immediate future research and experimentation. The thesis concludes with an exploration on how this method can be used to study Gabor filter optical responses to apoptotic agents in biopsied iBMK tumor tissue is given, offering a broader outlook of the applicability of the optical Gabor filtering technique in a broader clinical setting.

CHAPTER 2 : OPTICAL DESIGN AND INSTRUMENT DEVELOPMENT

The optical processing approach required the design of an optical processing system which accomplishes both microscopic imaging and optical Fourier filtering, and which must meet several design requirements. It must be sensitive to changes in both size and shape, and it must allow for an independent measurement of each. It should be able to operate without the introduction of stains or dyes and must accommodate study of living samples. As a prototype, the system must also be able to readily accommodate changes in optical design. This chapter describes the evolution and construction of the optical Gabor filter microscope, beginning with the foundation laid by Boustany and Zheng in designing the OSI instrument, the addition of a spatial light modulator (SLM) in place of an iris to achieve Fourier filtering, the implementation Gabor filtering on the SLM, and calibration and testing of the resulting redesigned microscope. This chapter describes how two distinctly different SLMs were used to achieve Fourier filtering, and the advantages and disadvantages of each instrument.

2.1: OPTICAL GABOR FILTERING EVOLVED DIRECTLY FROM THE OSI DESIGN

The chosen design approach was therefore similar to those taken by Boustany in designing the OSI instrument (72), which takes advantage of conjugate image planes and conjugate Fourier planes to allow the optical magnification from the microscope and optical filtering applied by the user to occur independently (**Fig. 2-1**). From a design perspective, this allows the use of a commercial microscope whose output is then filtered outside of the microscope system, and this achieves a good-quality imaging system when carefully aligned.

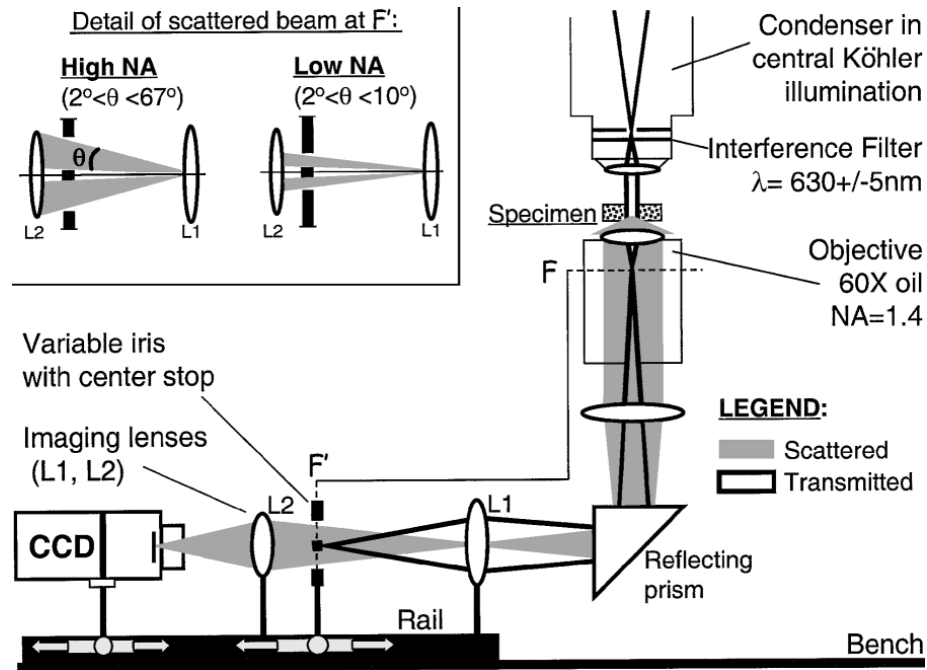


Fig. 2-1. (printed from Boustany et al., (72) with permission): OSI setup. The objective back focal plane F is projected out of the microscope to conjugate Fourier plane F'. The scattered light (gray beam) is used to image the specimen on the CCD. Transmitted light (black ray traces) is blocked at F' yielding DF. The inset shows the setup at the high NA and low NA OSI imaging configurations.

The most serious limitation of this approach results from the fact that the optics of the microscope and the Fourier processing sections are not linked. Therefore, when a change to the microscope settings resulting in a change of optical geometry (e.g. switching the objective), the entire optical system for the Fourier processing component must be reconfigured as well. This precludes switching the objective on-the-fly during experiments.

2.2: OPTICAL GABOR FILTERING WITH A DIGITAL MICROMIRROR DEVICE

The first design iteration of the optical Gabor microscope used a Texas Instruments Digital Micromirror Device (TI 0.7 XGA DMD 1100) (DMD) as the spatial light modulator. The DMD is a 1024x768 array of individually addressable $13.7 \times 13.7 \mu\text{m}^2$ mirrors, which can be actuated to deflect the light towards or away from the CCD detector, thereby allowing for binary on/off amplitude modulation of the field at each mirror. The DMD mirror array is

rotated 45° with respect to the direction of actuation, giving a mean spacing of $13.7/\sqrt{2} = 9.61 \mu\text{m}$ and $N = 2 \times 768 = 1536$ lines. In the image space, the DMD is a robust spatial light modulator with very fast image cycling (>150 frames/sec), high throughput, and good contrast ratio. Others have used the DMD and exploited these strengths with great effect for applications in high-speed addressable confocal microscopy (76), photopolymerization (77), and digital holography (78). The next section describes how the DMD is utilized in building the optical system, and how its characteristics dictated a substantial portion of subsequent design constraints.

2.2.1: THE DMD DICTATES THE OPTICAL DESIGN

Placing the DMD in the conjugate Fourier plane instead of the image plane as used in the applications mentioned above is a somewhat uncommon design arrangement. Doing so allows for filtering of the Fourier plane with any shape linear filter localized to any spatial frequency desired. This offers a number of advantages, including the ability to measure object orientation independently of size by using a set of filters that change orientation in the Fourier plane. A filter bank that measures both object size and shape may be implemented by arraying a filter bank such that the passband of the filter varies in spatial frequency and orientation. This enables the user to measure object shape, size and orientation without *a priori* assumptions or a restrictive scattering model.

The DMD is a tremendous design improvement over the OSI iris. However its introduction required significant design modifications to the original OSI system, which were initially undertaken by Zheng et al. (79). The first change was the extension of the optical train to include a second conjugate Fourier plane in which the DMD is placed (**Fig. 2-2**). This allows the system to generate a collimated beam with a second image plane

upstream of the device. This allows significantly more freedom in decoupling the size of the Fourier plane from the size of the final image. This configuration also allows for the placement of an analog beam stop in the first Fourier plane, or an OSI iris if desired (**Fig. 2-2**)(OSI irises can be automatically applied on the SLM if desired as well).

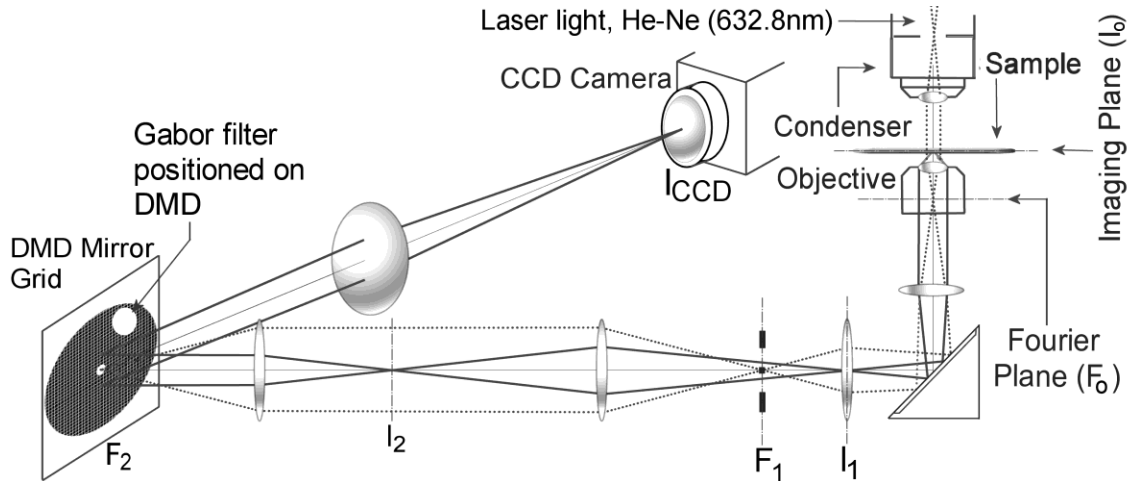


Fig. 2-2. Setup. The transform of the object is focused at F₀, F₁, and F₂. The object image is focused at I₀, I₁, I₂ and ICCD. A beam block at F₁ blocks the zeroth order. Analog filtering at F₂ is accomplished by applying a series of Gabor-like filters to the DMD. Printed from Pasternack et al. (80) with permission.

The DMD has characteristics of both a reflector and a diffractor, and this dictated several other aspects of the system design. First, the optical train follows along the 12° DMD mirrors' reflection angle, which requires aligning the optics downstream of the DMD along a rail oriented 24° from incidence. The DMD acts as a diffraction grating and obeys the law of diffraction, $\sin\theta_m = m\lambda/a$, where $\sin\theta_m$ describes the position of the diffraction orders, m is the order number (0, 1, 2, ...) λ is the wavelength of incident light, and a is the DMD mirror spacing. As a result several images of the object's transform are generated at each of the diffraction orders. The wavelength dependence imposes bandwidth limits on the illumination. The bandwidth tolerance $\Delta\lambda$ is given from the grating equation, $\lambda_0/\Delta\lambda = mN$, where λ_0 is the incident wavelength, $\Delta\lambda$ is its bandwidth, m is an integer which refers to the brightest diffraction order. The bandwidth of illumination must be smaller than $\Delta\lambda$ to avoid

wavelength-dependent smearing in the image when the imaging utilizes the transforms generated at diffraction orders other than $m=0$. All spatial light modulators have spacing between their elements and so must have similar restrictions. However, because of the tilt of the DMD mirrors, the DMD acts as a blazed grating, in which the highest intensity diffraction order is not the zeroth but the sixth (79). Thus, for $m = 6$, $\lambda_o = 633 \text{ nm}$, and $N = 2*768 = 1536$, $\Delta\lambda = 0.07 \text{ nm}$, a condition requiring an ultra-narrowband illumination.

The DMD therefore dictates the illumination and its efficiency as well. We used a HeNe 5mW laser to satisfy the bandwidth requirement; however, the laser is highly coherent, and so this in turn must be passed through a spinning diffuser to scramble the phase of the light to achieve a uniform background illumination without coherent speckle. Losses of light to the other diffraction orders of the DMD are significant and contribute to the DMD's 45% overall throughput efficiency (79). Other contributing factors to light loss include mirror reflectivity, window transmittance, fill factor, and mismatch between the DMD's blaze wavelength (650 nm) and the light source (633 nm). Because of light losses in the laser launch and diffuser, and the optical losses through the DMD, >99% of the current flux is lost from the launch to the sample, with an additional factor of 3-4 losses through the remaining optics and DMD. This imposes severe restrictions on exposure and acquisition time, especially when using Gabor filters.

Further restrictions are imposed on the maximum size of the Fourier plane (and thus the highest DMD spatial frequency resolution) by the optical qualities of the DMD. Zheng et al. (79) found that the DMD transfer function behaved in a markedly non-ideal way. That work is reproduced and elaborated here. Ideally, the DMD diffraction pattern should consist of a grid of spots whose spacing is a function of the DMD mirror spacing. Additionally, the shape of each spot should simply be the Fourier transform of the aperture placed on the

DMD if the DMD behaved as a perfect reflector. Hence, for example, the DMD transfer function with a circular aperture should be a circular Bessel function of the first kind. It should very nearly resemble a bright spot that defocuses in a circularly symmetric manner as the CCD is moved axially away from the Fourier plane in either direction. However, the shape of each spot, which in this document is called the transfer function (TF) of the device, did not yield this result. Instead, when DMD TF is imaged in the Fourier plane, the DMD TF appears aberrated. Further, these aberrations were only mitigated by decreasing the extent of the aperture placed on the DMD.

As **Fig. 2-3** illustrates, the DMD TF resembled a cross (with one leg of the cross brighter than the other) even when a circular aperture was applied. Moving the CCD axially about the image of the Fourier plane clearly revealed that the TF was not circularly symmetric. This effect can be reduced by decreasing the size of the Fourier plane on the DMD. Based on other reports by other manufacturers (e.g. Holoeye photonics, 3146 Tiger Run Court, Suite 120, Carlsbad, CA and Hamamatsu, 360 Foothill Road, Bridgewater, NJ) discussing the effect of the curved silicon surface of some spatial light modulators we suspect that the mirror array of the device is not perfectly planar, and that the device effectively lenses the applied collimated beam astigmatically. Reducing the astigmatism effect by reducing the extent of the Fourier plane on the device was the best method for improving the quality of the TF in the imaging system, but came at the cost of sacrificing nearly 80% of the available DMD mirrors and 60% of the possible sampling resolution per mirror. These effects persist regardless of the choice of optical alignment or illumination configuration.

Finally, after all these considerations arising from the DMD, including illumination, extent of the Fourier plane, and TF, the next section will discuss how the Gabor filter is implemented on the DMD.

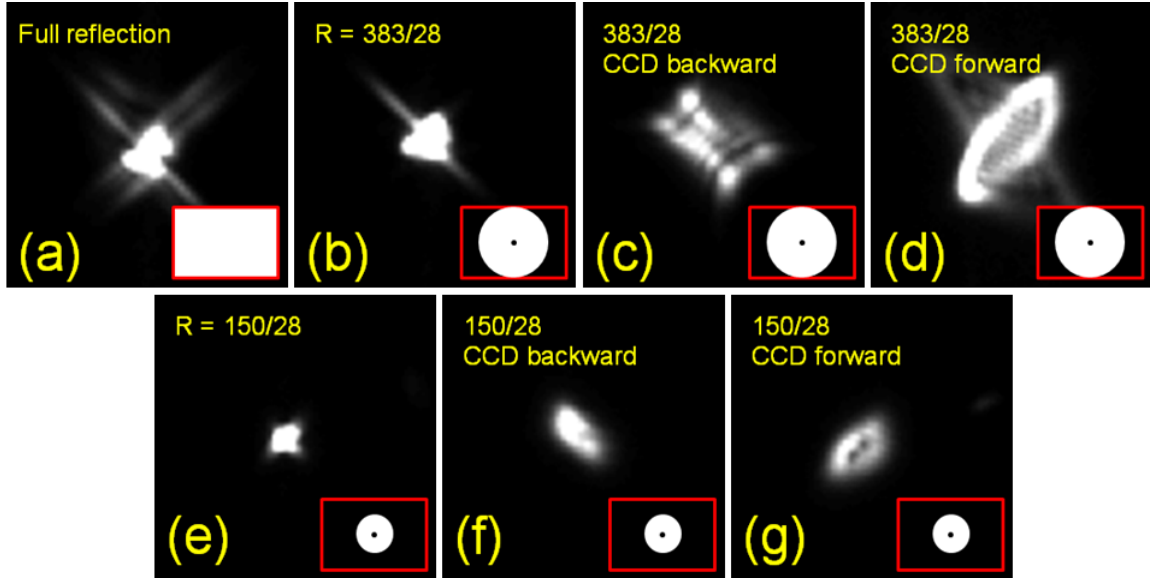


Fig. 2-3. Imaging the DMD TF. (a). The DMD TF when all mirrors are actuated "on." (b-d). The DMD TF for an iris passing light between mirror radii $R = 28$ and $R = 383$ with the CCD placed in-the-plane, backward out-of-the-plane, and forward-of-the-plane, respectively. (e-g). The DMD TF for an iris passing light between mirror radii $R = 28$ and $R = 150$ with the CCD placed in-the-plane, backward out-of-the-plane, and forward-of-the-plane, respectively.

2.2.2: IMPLEMENTING GABOR FILTERING WITH THE DMD

Descriptively, a Gabor filter may be considered a "tunable ruler", where sensitivity to object size and orientation may be chosen independently. They have been used extensively in texture discrimination (81) and texture-based segmentation (82) in digital processing because of their tunability to specific textural patterns within an image. Mathematically, a Gabor filter in the space domain corresponds to a complex sinusoidal wavelet with a Gaussian envelope and is composed of a 2D Gaussian multiplied by a complex 2D sinusoid: $H(x, y) = G(x, y) * S(x', y')$, where $G(x, y)$ is a 2D Gaussian rotated by an angle φ with standard deviations σ_x and σ_y and $S(x', y')$ is a complex 2D sinusoid function $S(x', y') = \exp(-j2\pi(Ux' + Vy'))$ (**Fig. 2-4**). U and V represent the Cartesian spatial frequencies of the sinusoid. The orientation of the sinusoidal stripes in the space domain is defined as $\varphi = \arctan(V/U)$, and the peak-to-peak distance between the stripes is defined by the period S of

the 2D sinusoid: $S = (U^2 + V^2)^{-1/2}$. The choice of φ and S therefore decide the characteristics of this "ruler." In the Fourier domain, a 2D Gabor filter's impulse response is a Gaussian-shaped band-pass filter: $H(u, v) = A \cdot \exp(-2\pi^2 S^2 [(u - U)^2 + (v - V)^2])$, where A is the amplitude of the filter impulse response. The Gabor filter confines the filter impulse response in both the space and Fourier domains, and does so in a manner such that the extent of the filter in both domains is mathematically minimized (83). This has the desirable consequence of optimizing both spatial and frequency resolution, allowing the response of the filter to be spatially localized while still preserving frequency sensitivity. In this work, we used a symmetric Gaussian envelope with $\sigma_s = S/2$.

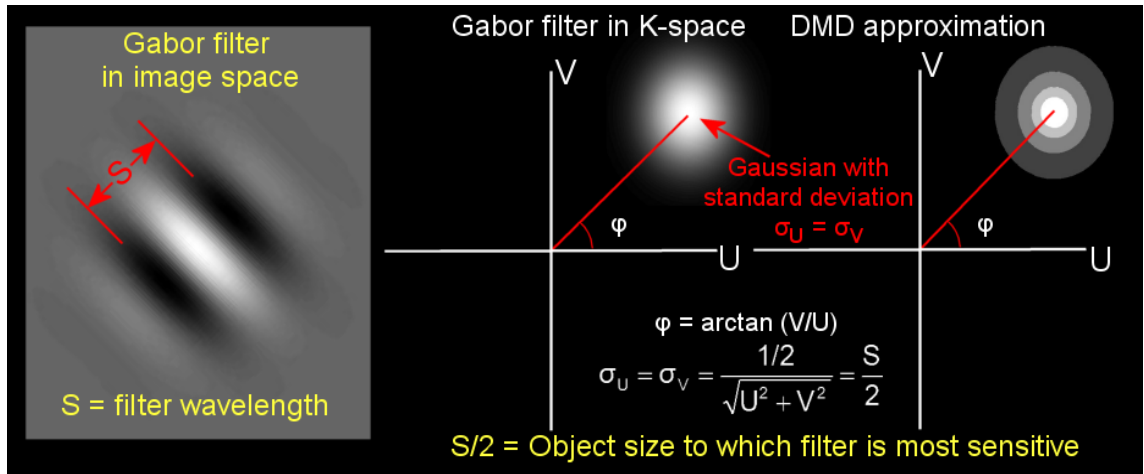


Fig. 2-4. Description of a Gabor filter.

An approximation of the Gabor filter (**Fig. 2-4**, **Fig. 2-5**) can be projected onto the DMD by applying four concentric binary discs and cycling them on the DMD. Each filtered image is a quasi-coherent sum of the filtered images generated by each layer. We continuously cycle each of the images (each image is displayed over ~ 5 ms) over a long exposure (250-2000+ ms depending on the application) to capture the filtered image all at once. A Gabor filter, its approximation, and an intensity profile are given in **Fig. 2-5**.

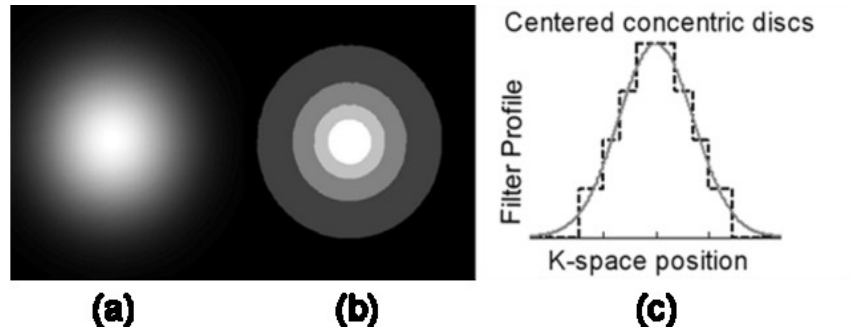


Fig. 2-5. Illustration of DMD implementation of Gabor filter. (a): Ideal Gabor Filter in k-space. (b): DMD approximation formed by overlay of binary concentric discs. (c): Overlapping profile views of (a) and (b). Printed from Pasternack et al. (80) with permission.

In general, many filtered images are needed and must be generated with the application of many filters (filter bank). This systematic probing of the object scatter plane forms the basis of the dataset from which morphological information may be extracted. For example, a filter bank may be chosen that measures the intensity of scatter as a function of azimuthal angle φ , thereby gauging the scatter intensity as a function of object orientation. Objects that are highly oriented (i.e. oblong) in the field of view may be studied with such an approach (**Fig. 2-6**). A Gabor-like filter bank of different periods can yield information about changes in particle size at the chosen orientation (**Fig. 2-6**). Both filter bank paradigms have been tested (80; 84) and will be discussed in detail in Chapter 3. It is important to note that these filterbanks represent only a small fraction of the possible information that can be collected. The application of these filterbanks is a demonstration of feasibility on a sample whose morphology is expected to show a response to these filters. In general, when probing a system whose morphology is not well characterized, the user would collect filtered images encompassing the entire Fourier plane, and then extract from these data the ones which yield a useful response. This need led to the redesign and automation of the optical setup and will be discussed in Chapters 2, Section 2.3.

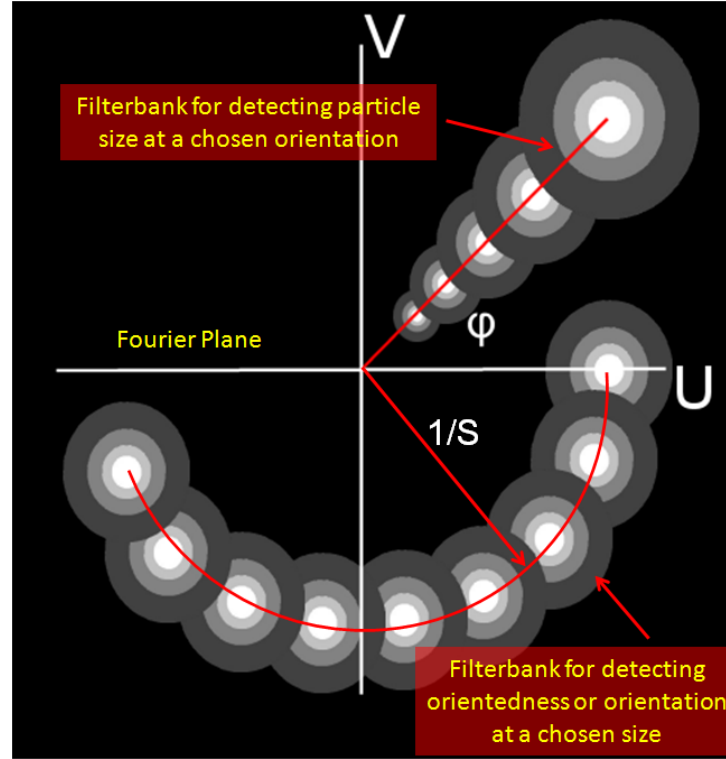


Fig. 2-6. Illustration of filter bank design. Top filter bank measures particle size at chosen angle φ . Bottom filter bank measures particle orientedness or orientation at chosen spatial frequency $1/S$.

2.2.3: SETUP AND ALIGNMENT OF THE OPTICAL SYSTEM

In general, the Gabor filter's spatial frequency $1/S$ is implemented in units of DMD mirrors. In order to define a relationship between DMD mirrors and spatial frequency in cycles per micrometer, the size of the Fourier plane projected onto the DMD must be measured. Using the same procedure as Zheng (79), calibration of the device is achieved with the help of an object (in this case a graticule) whose Fourier transform consists of a diffraction pattern whose spatial frequency spacing is known. In this case, calibration is achieved using a graticule with line spacing $b=10\mu\text{m}$ yielding diffraction orders m with spatial frequency increment $f = 1/b = 0.1\text{cyc}/\mu\text{m}/\text{order}$ at angles θ_f with respect to the optical axis. With spatial frequency on the Fourier plane defined (in $\text{cycles}/\mu\text{m}$) as $\sin\theta/\lambda_o = m/b$, mirror positions of the diffraction orders on the DMD are converted to spatial frequency in $\text{cycles}/\mu\text{m}$ (**Fig. 2-7**).

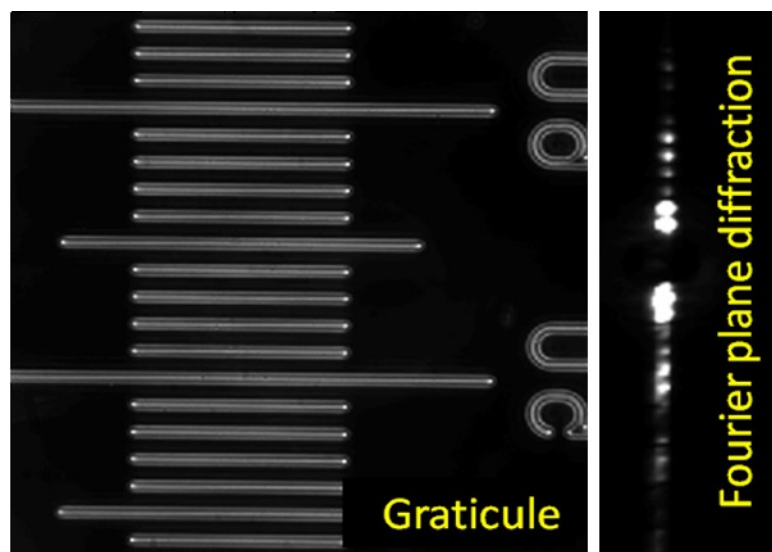


Fig. 2-7. Using a graticule imaged in DF with known line spacing (left) to calibrate the DMD and derive the spatial frequency increment per mirror. The diffraction pattern (right) is imaged in the presence of an iris ruler in which concentric tickmarks in the Fourier plane block the transmittance at regular mirror intervals.

The maximum aperture corresponds to NA/λ_o , where the NA of the objective is 0.75 or 1.4 for a 20x air or 63x oil objective, respectively. This maximum aperture can be projected onto the entire radius of the DMD (or a smaller portion) by appropriate choice of optics in **Fig. 2-2**. Typically the calibration gave ~ 0.0069 cycles per μm per mirror for the 63X when a region 320 mirrors in diameter was used on the LCD and ~ 0.0075 cycles per μm per mirror for the 20X objective when a region 150 mirrors in diameter was used on the DMD. Unfiltered images in dark field may be acquired, in which case the unscattered light is excluded by both an analog dot at F1 and a zeroth-order block filter on the DMD. Unfiltered images in differential interference contrast (DIC) are also obtainable by diffusing and polarizing the light source, increasing the numerical aperture of illumination through the condenser and by adding a Wollaston prism behind the objective and in front of the condenser. Final image magnification is achieved by selecting the focal distance of an imaging lens placed in front of the CCD without changing the NA of the system at the level of the DMD.

2.3: OPTICAL GABOR FILTERING WITH A LIQUID CRYSTAL DEVICE

The spatial light modulator is the focal point of the optical design. Although the DMD-based instrument was successful, the limitations of using the DMD (Chapter 2, Section 2.2.1) present severe constraints onto further design improvements and performance of the instrument. An overhaul of the setup was therefore undertaken, which replaced the DMD with a liquid crystal on silicon (LCoS) device, which in turn required a reconfiguration of the optical setup.

The LC R-2500 (HoloEye, Germany) liquid crystal display (LCD) was selected to replace the DMD as the spatial light modulator. Whereas the DMD operated in reflection mode, transmitting or blocking light based on the tilt of the mirrors, the liquid crystal device operates using phase modulation to achieve the same result. The LCD display itself consists of 1024x768 pixel elements capable of both amplitude and phase modulation of the incident E-field. Although this dissertation project explores only the amplitude modulation capability, it should be emphasized that phase modulation (which was completely beyond the capability of the DMD) is an alternative avenue of great interest for the optical setup that will be explored in the future. While the amplitude modulation of the DMD is binary (on/off), the LCD is capable of 8 bit graylevel (0-255) amplitude modulation. This obviates the need for cycling images of concentric discs on the DMD to approximate a Gaussian filter envelope. Instead, the Gaussian Gabor filter may now be simply placed on the device directly by utilizing the gray level amplitude modulation. This constitutes the first significant advantage that the LCD offers over the DMD.

The LCD and the LCD both act as diffractors, and so both obey the grating equation, $\lambda_o/\Delta\lambda = mN$. However, the LCD also has superior optical qualities for our purposes arising from the absence of blazing effects. Because there is no phase shift across the device arising from mirror tilt, the zeroth diffraction order is the brightest. The lack of blazing also eliminates losses due to mismatch between the blaze wavelengths and illumination wavelengths. These qualities also greatly relax the bandwidth limitations for the device illumination, allowing for illumination sources other than ultra narrow-band single spectral line sources.

Recall that the bandwidth tolerance of the DMD is $\Delta\lambda = 0.07$ nm. (see Chapter 2, Section 2.2.1). As was the case for the DMD, the bandwidth of illumination must be smaller than $\Delta\lambda$ to avoid wavelength-dependent smearing in the image in the LCD setup as well. However, the LCD does not act as a blazed grating and so the object transform is produced at the LCD's 0th order of diffraction and not the 6th. One can therefore use the zeroth order with $m = 0$, and because the orientation of the array is 0°, $N = 768$ for the LCD. These two conditions relax the wavelength constraint For $m = 0$, $\Delta\lambda \rightarrow$ infinity. Thus limiting the wavelength is no longer necessary for aberration-free imaging and one can utilize laser or LED illumination bandwidths with much more forgiving and less expensive solid state lasers. Furthermore, with sufficiently narrowband filters, it should also be possible to use the LCD with fluorescence microscopy. Utilizing a relatively narrow-band illumination also remains desirable to extract accurate angular scattering information from the objects being probed by this imaging system.

In addition to relaxing the wavelength constraint, the LCD also improves the quality of the system transfer function, thereby allowing a choice of optics that eliminates image overlap in the collected images while filling the device almost completely. Contrast ratio for

the LCD-based system is reduced, owing to the slight passive reflectance of the LCD pixels even when unbiased, but the use of the analog dot minimizes this drawback. Details of the performance of the LCD system are given in Chapter 3, Section 2.3.2.

The new setup capitalizes on these differences in gray level modulation and diffractive quality, and implements a redesigned optical launch and filtering scheme. The following section describes the new setup, optical Gabor filter implementation, and characterization of the LCD.

2.3.1: DESCRIPTION OF OPTICAL SETUP

Illumination is provided by a custom illumination setup consisting of a ~ 25 mW solid state laser ($\lambda_0 = 638 \pm 0.5$ nm). Laser output is focused through a ground glass spinning diffuser (DG20-120, Thor Labs, NJ) in order to reduce speckle resulting from the laser's coherence. The diffuser output is collimated and coupled into a multimode fiber whose output is launched into the microscope's condenser aligned in central Köhler illumination ($NA < 0.05$) (**Fig. 2-8**).

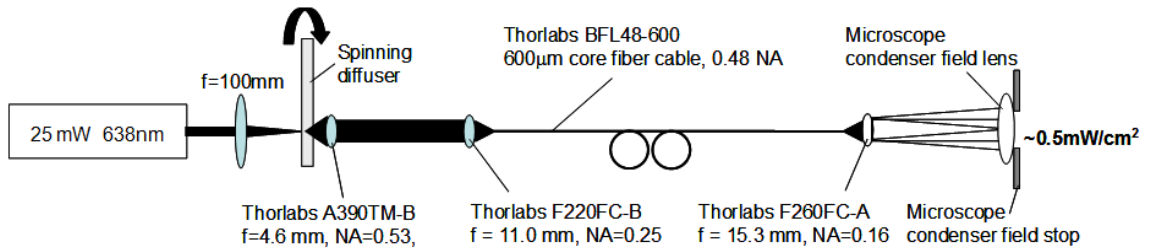


Fig. 2-8. Laser illumination launch. Narrow-band laser light from a ~ 25 mW crystal laser is focused ($f = 100$ mm) onto a ground glass diffuser (DG20-120, Thor Labs, NJ) spinning at > 500 rpm. Diffused light is collected and collimated by an aspheric lens (A390 TM-B, Thorlabs, NJ), and coupled into a single mode fiber (BFL48-600, $NA=0.29$ Thor Labs) by an aspheric fiber collimator (F220FC B, Thorlabs). Fiber output is collimated using an $f = 15.3$ mm aspheric lens (F260FC-A, Thorlabs) and input to the microscope condenser through the field lens. Drawn by Dr. Boustany.

The main optical setup consists of an inverted commercial microscope (Axiovert 200M, Zeiss, Göttingen Germany) fitted with a 60x $NA=1.4$ oil immersion objective and the liquid crystal device placed in a conjugate Fourier plane to the back focal plane of the

objective (**Fig. 2-9**). Alignment of the setup requires choosing the position of L1 and then pegging distance of L4 exactly f_4 away from the CCD. The position of L2 is adjusted until the Fourier plane is focused on the CCD. This approach ensures that the light incident to L4 is collimated and hence that the position of L2 is correct. L3 is then placed so that the object's image is generated on the CCD and is parfocal with the focused sample in the eyepiece. Finally, the position of the LCD while the LCD is actuated to show a dark field aperture. The position and orientation of the device is adjusted until a dark field is achieved, assuring that the device is coincident with and centered in the Fourier plane F2. The analog beam stop at F2 is used when imaging to further reduce background and leakage of unscattered light.

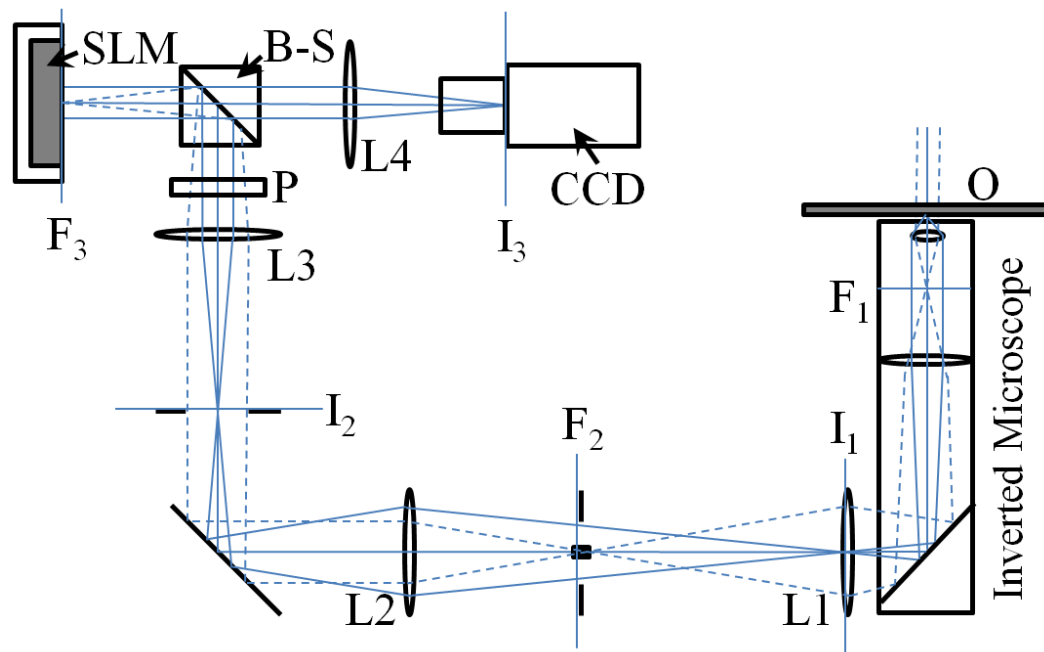


Fig. 2-9. Optical setup. Light from the laser launch in central Köhler configuration strikes the object O mounted on the inverted microscope which is imaged at I₁, I₂ and I₃; Fourier planes of the object image occur at F₁, F₂, and F₃. Spatial filtering occurs on the SLM at F₃. A polarization beamsplitting cube (B-S) is placed to pass horizontally polarized light to the SLM and to transmit vertically polarized light from the SLM to the CCD. A horizontally oriented polarizer (P) is placed in front of the B-S to enhance vertical extinction. A beam block at F₁ blocks enhances the elimination of transmitted light. A field stop is placed at I₂.

Once alignment is complete, calibration of spatial frequency on the LCD is achieved by imaging the Fourier plane on the LCD directly on the CCD by replacing L4 with a lens of shorter focal length. As for the DMD-based system, to measure spatial frequency, we use a graticule with line spacing $b=10\mu\text{m}$ yielding diffraction orders m with spatial frequency increment $f = 1/b = 0.1\text{cyc}/\mu\text{m}/\text{order}$ at angles θ_f with respect to the optical axis. While imaging the Fourier plane, we use a concentric bull's-eye target centered on the LCD as a spatial frequency ruler to measure the position of the diffraction orders in LCD pixel elements. With spatial frequency on the Fourier plane defined as $\sin\theta/\lambda_o = m/b$, mirror positions of the diffraction orders on the LCD are converted to spatial frequency in cycles/ μm . The calibration C for the current configuration was found to be $C = 0.00693$ cycles/ $\mu\text{m}/\text{LCD pixel element}$, placing the maximum aperture $= \text{NA}/\lambda_o$ at a radius of 320 pixel elements. After calibration, L4 is replaced to its initial position. Final image magnification is achieved by selecting the focal distance of L4 without changing the NA of the system at the level of the DMD. The magnification on the CCD (measured in $\mu\text{m}/\text{pixel}$) is measured directly by imaging the graticule and is found to be $0.31\ \mu\text{m}/\text{pixel}$ for $f_{L4} = 200\text{mm}$.

2.3.2: DESCRIPTION OF THE LCD

The LCD is a 1024×768 array of individually addressable $14 \times 14\ \mu\text{m}^2$ pixel elements. Diffraction from the LCD pixels occurs at $\sin\theta_m = m\lambda_o/a$ (θ_m is angle of diffraction for diffraction order m , λ_o is incident wavelength, a is LCD pixel element size). The first diffraction order occurs at $\theta_m = 2.6^\circ$. For our CCD, the CCD field is $512 \times 512\ 16\mu\text{m}$ square pixels, giving an acquisition field of $D = 8.2\text{mm}$ on a side. The distance Δr between additional images convolved with the LCD diffraction is given by $\tan\theta_m = \Delta r/f$, where f is the

focal distance of L4. In order to avoid image overlap from the convolution of LCD diffraction and the CCD, $\Delta r > D$ must be true. For the current setup, $f = f_4 = 200\text{mm}$, giving $\Delta r = 9.0\text{ mm}$ which satisfies $\Delta r > D$. Therefore, we do not observe image overlap from LCD diffraction in the LCD-based setup rigged in this optical configuration. However, other choices for lens focal lengths may be in general be useful (e.g. to enlarge or demagnify the image at the CCD) which can still produce overlap. In such a situation, an image deconvolution algorithm such as that developed by Zheng (75) may be used.

Image acquisition consists of collecting on a 16-bit CCD (Roper Scientific Cascade 512B) spatially filtered dark-field images resulting from filter banks displayed on the LCD. Optical filters are displayed on the LCD in the form of 8-bit grayscale TIFF images. These images are calibrated to the device's look-up table (LUT), which translates the 8-bit grayscale. In turn, each LUT element value assigns the device throughput, and therefore the signal detected on the CCD, to the input gray level (**Fig. 2-10b**). The factory-set LUT is modified so that the LCD signal throughput varies linearly as a function of gray scale value. LUT linearization is accomplished with the use of the CCD by imaging signal from a collimated beam incident to the LCD and modulated by the graylevel applied to the entire device. The lookup table values are then re-assigned (**Fig. 2-10a** solid line) so as to linearize signal response as a function of applied gray level (**Fig. 2-10b** solid line. Both white offset and black offset are constrained to maximize contrast ratio between on (grayscale value= 255) and off pixels (grayscale value= 0). The LUT blackpoint was reached when the LUT value is less than 183, and whitepoint was reached when the LUT value is greater than 483. The remaining range of values (184-483) was distributed across all gray levels (0-255) as shown in **Fig. 2-10a** (solid trace) yielding an almost linear relationship with signal ($R^2 = 0.99$,

Fig. 2-10b solid trace). The original factory-set LUT values and signal relationship (**Fig. 2-10**, dashed traces) are shown for comparison.

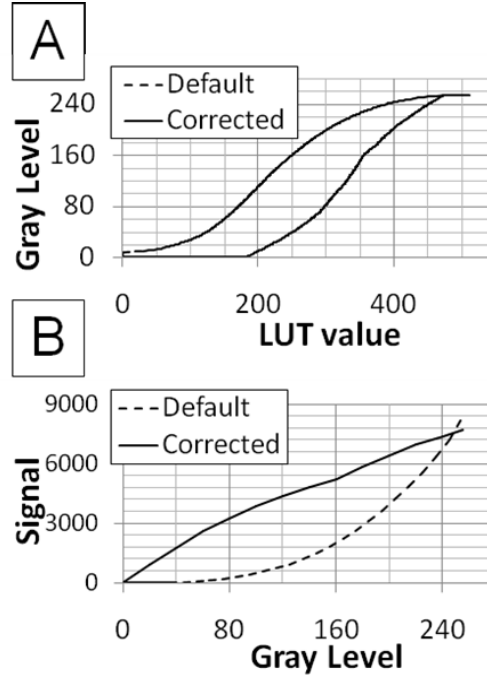


Fig. 2-10. LUT linearization. (a): Device gray level input vs. LUT value for that gray level. (b): Signal vs. gray level input. For both (a) and (b), device defaults are given by the gray traces while the corrected values are given by the solid traces.

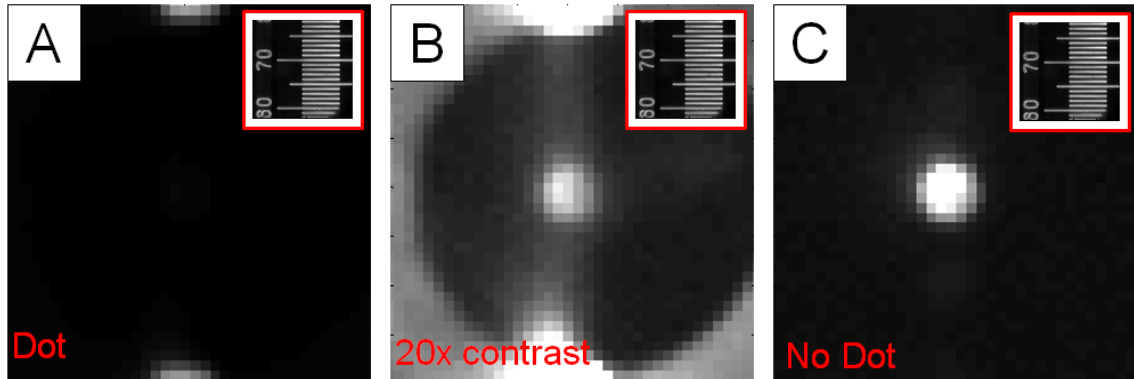


Fig. 2-11. Contrast ratio. (a): DC component with device beam block in position. Non-zero orders of diffraction are evident at the top and bottom of the image. (b): Contrast enhanced rendition of (a) demonstrating small amount of DC transmission. The intensity of zeroth order (adjusted for exposure and neutral density) was 0.958×10^3 CCD counts. (c): DC component with device beam block removed. The intensity of zeroth order (adjusted for exposure and neutral density) was 1.427×10^6 CCD counts. The orders of diffraction evident in (a) and (b) are dim in comparison to the DC component. For reference, DF images of the graticule responsible for diffraction pattern are inset in red (upper right) on each panel.

After the LUT is linearized, contrast ratio is measured by imaging the diffraction pattern of the graticule sample. The diffraction pattern is imaged with and without blocking the zeroth order. When the zeroth order is not blocked, all pixels on the LCD are set to gray level 255. To block the zeroth order pixels within a circular LCD region 56 LCD pixels in diameter are set to gray level 0. With all other pixels remaining set on gray level 255. The zeroth order spot includes all pixels that pass a threshold of 10% of maximum signal in the unblocked image. The contrast ratio of the device is measured as the ratio of the on/off intensities of the zeroth order spot after normalizing for differences in exposure times and neutral density (**Fig. 2-11**). The Analog beam stop at F1 (**Fig. 2-9**) is removed when measuring contrast ratio of the LCD.

Contrast ratio in the Fourier plane was measured at 1490:1 while the device specifications call for a contrast ratio of 3000:1 or more. This discrepancy is due to the limited extinction efficiency of the polarization beam splitting cube (rated at 1000:1). A detailed image of the diffraction pattern captured on the CCD is given in **Fig. 2-11**. **Fig. 2-11b** shows the diffraction pattern with contrast enhanced to detail the circular beam block on the device and the DC component. Higher diffraction orders ($m \geq 1$) lie beyond the edge of the circular patch (**Fig. 2-11a - Fig. 2-11b**). Because the zeroth order is brighter than the other orders of diffraction by a factor of >33 , these are not visible when the zeroth order is unblocked (**Fig. 2-11c**).

Transfer function (TF) of the SLM is measured by removing L3 (**Fig. 2-9**) and imaging the Fourier transform of the collimated beam applied to the device. No sample is applied to the instrument when imaging the TF, and the analog beam stop (**Fig. 2-9**) is also

removed. TF is measured for binary circular apertures of radius $R = 300$ or $R = 384$ pixels centered on the SLM (

Fig. 2-12) for which pixels within R are applied a gray level of 255 while all others are applied a gray level of 0. For both apertures, the device transfer function is circular (

Fig. 2-12). The presence of a circular transfer function indicates the absence of optical aberrations due to the device. In contrast to the DMD, the LCD can generate a circular transfer function using the entire available area with a circular aperture, allowing the Fourier plane to occupy more of the LCD than was possible with the DMD, greatly increasing imaging flexibility. Using this same optical configuration, device throughput was measured to be 79% with the aid of an optical power meter applied to the incident beam before and after the device.

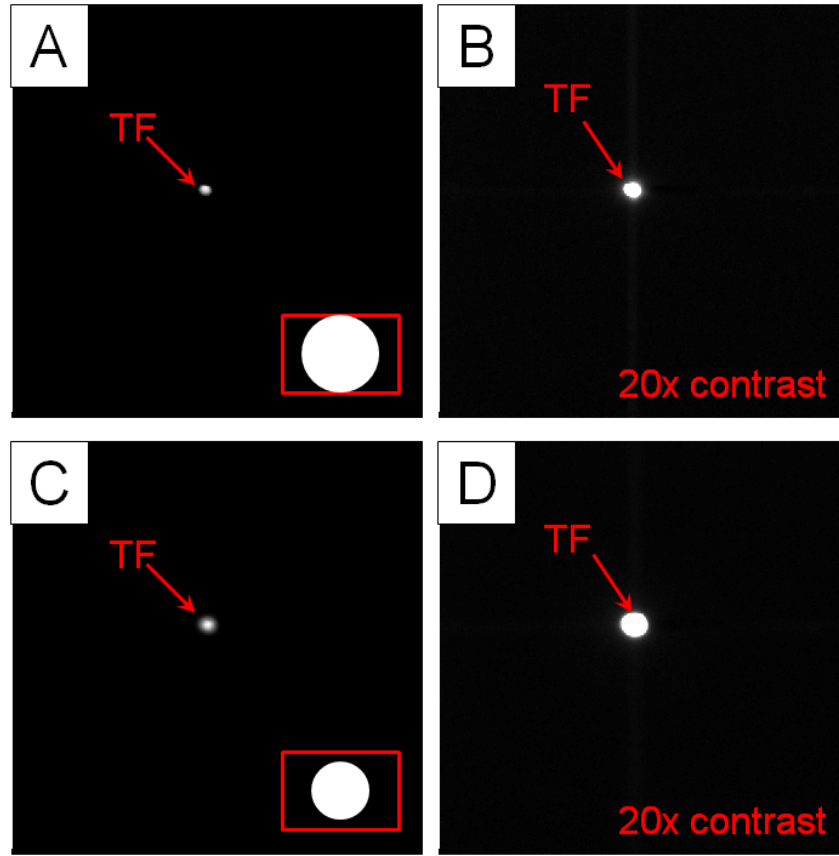


Fig. 2-12. TF. (a): TF with 768 mirror aperture placed on LCD. An illustration of the aperture image placed on the LCD while collecting TF is inset in red (lower right). (b): TF from (a) contrast-enhanced dim regions in TF. (c): TF with 600 mirror aperture placed on LCD. An illustration of the aperture image placed on the LCD while collecting TF is inset in red (lower right). (d): TF from (c) contrast-enhanced to dim regions in TF. TF remains circular and symmetric indicating the absence of optical aberration from the LCD.

A point spread function of the LCD system is also collected (**Fig. 2-13**) by replacing L3 and imaging in standard mode a sample of 0.217 μm polystyrene microspheres. The preparation of this sample is detailed in Chapter 3, Section 3.3. The position and focal length of L4 are adjusted in order to magnify the image of the sphere on the CCD. The sphere best approximates a point source relative to the optical resolution of the system ($\sim 0.2\mu\text{m}$). Consistent with the shape of the LCD TF (Fig. 2-12), the PSF is a blurred point source and therefore the system is free of significant aberrations when properly aligned.

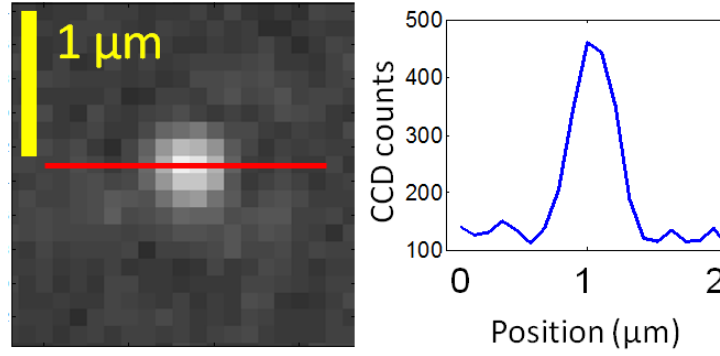


Fig. 2-13. Point spread function. (left): Image of 0.217 μm polystyrene microsphere. (right): Signal trace through center of PSF (red line). No significant aberrations are noted.

2.3.3: GABOR FILTER IMPLEMENTATION ON THE LCD

Gabor filters are created and applied as an image of the Gaussian on the LCD at the desired spatial frequency and orientation. The spatial frequency of the filters are transformed to LCD pixels with the aid of the calibration constant found as described above. We create our Gabor filters on a black 1024x768 array in MATLAB by constructing a Gaussian centered at pixel position $[x = 512 + \text{round}(f/C\cos(\varphi)), y = 384 + \text{round}(f/C\sin(\varphi))]$ on the array. We constrain the Gaussian amplitude A for all filters to white at position $[x,y]$ (i.e. $A([x,y]) = 255$). The program then constructs Gaussian corresponding to the Gabor filter for the choices given for f , φ and σ_k . To account for the slight deviation from linearity remaining in the device LUT, the Gabor filter gray levels are rescaled to the device LUT gray levels so that the intensity modulation of signal through the Gabor is linear with the modified gray level. **Fig. 2-14** illustrates the difference in gray scale for a representative Gabor filter.

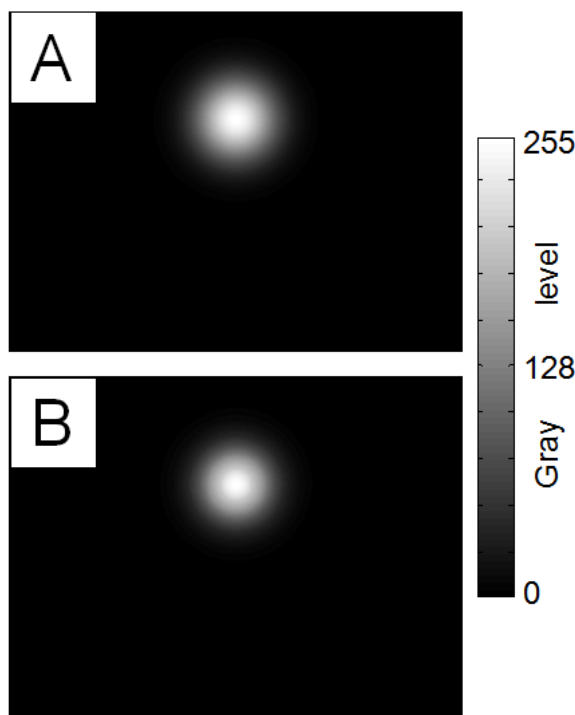


Fig. 2-14: Scaling the Gabor filter gray level to the LCD LUT. (a) 8-bit Gaussian corresponding to a Gabor filter with spatial frequency 1.11 cycles/ μm at Fourier orientation $\varphi = 90^\circ$. (d) The same Gabor filter whose graylevel is remapped to the new gray level values of the LUT.

Our setup provides illumination of sufficient intensity and consistency to achieve high SNR biological measurement. For example, unfiltered dark field images of immortalized baby mouse kidney cells (iBMK) under normal growth conditions (see Chapter 5) give an SNR of 38.9 (laser output at 23.5 mW, 50 ms exposure) (**Fig. 2-15**). Representative Gabor-filtered images (**Fig. 2-16**) yield a SNR of 17.1. Under these conditions, light intensity at the sample is measured to be $< 0.6 \text{ mW per mm}^2$.

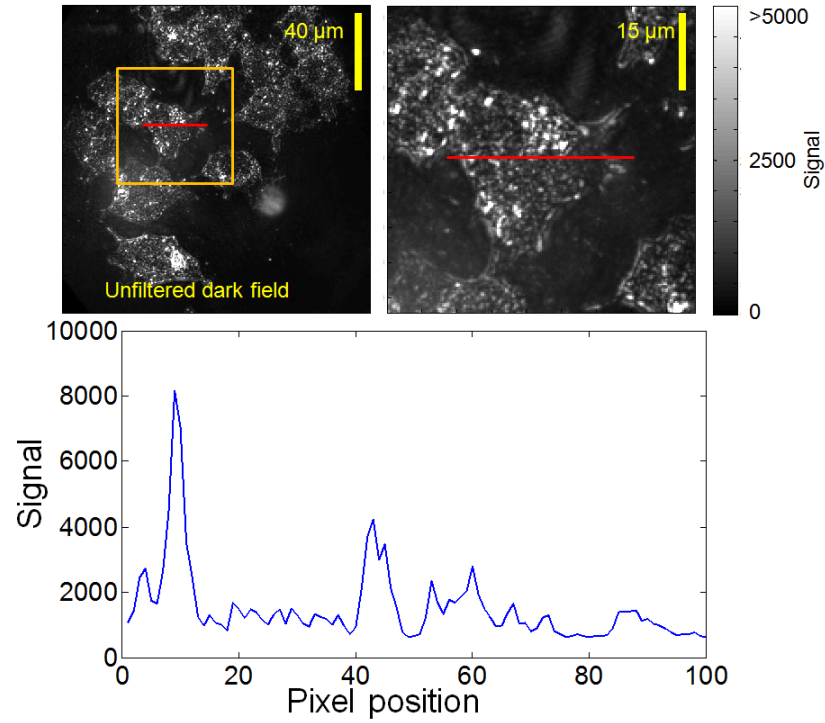


Fig. 2-15. Signal-to-noise ratio of unfiltered dark-field signal from iBMK cells. Signal plot corresponds to signal across red line segment in image.

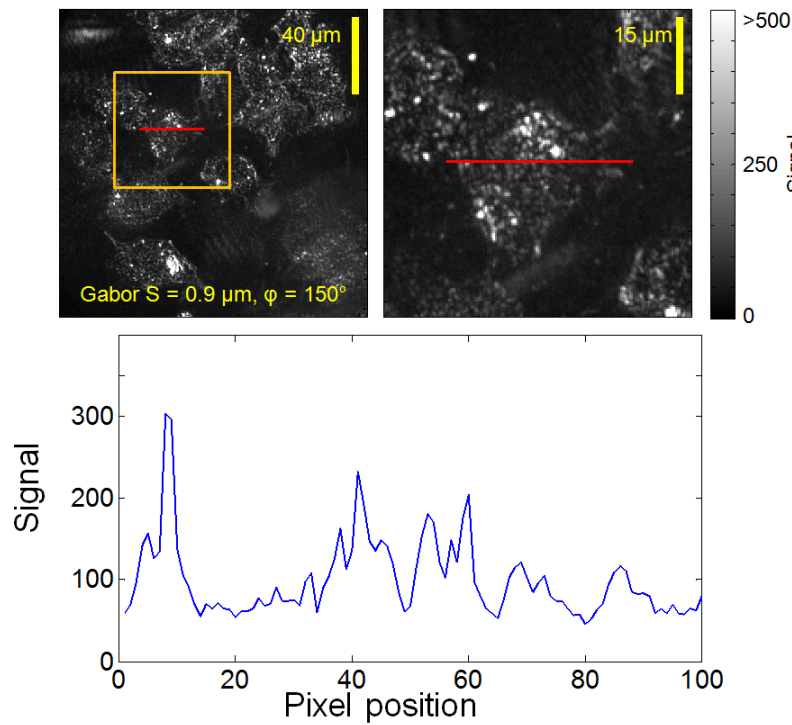


Fig. 2-16. Signal-to-noise ratio of Gabor filtered ($S = 0.6 \mu\text{m}$, $\varphi = 135^\circ$) dark-field signal from iBMK cells. Signal plot corresponds to signal across red line segment in image. ROI corresponds to same ROI as given in Fig. 2-15.

2.4: DISCUSSION

For both the LCD-based and DMD-based systems, the fundamental design approach remains the same as for OSI. Both techniques achieve optical Fourier filtering by modifying the E-field at a Fourier plane projected outside of a commercial microscope. Both operate on dark-field input to generate filtered images which may then be further processed. However, in their completed forms, both optical Gabor filtering setups are considerably different in design and implementation from the OSI apparatus. OSI requires a theoretical description in order to calibrate the size measurement to physical units. OSI cannot distinguish between size changes and shape changes.

The LCD-based system is a significant improvement over the DMD-based system. It offers the potential for phase modulation in future studies. It has transfer function properties which allow for filling the device in the Fourier plane, and its edges need not be avoided as was the case with the DMD. The LCD is capable of gray-scale modulation, making Gabor filter implementation much simpler than cycling concentric discs on the DMD. It also allows for using other light sources than ultra-coherent lasers.

The following chapter characterizes the performance of the Gabor filtering approach and develop formalisms for processing raw Gabor-filtered data into physically meaningful morphometric parameters. Chapter 3 shows how the Gabor filtering approach using the DMD-based system can measure changes in object size, aspect ratio and orientedness without the need for a predictive model. It also compares the analog Fourier processing method to postprocessing of digitally acquired dark-field or differential interference contrast images. Chapter 3 also demonstrates how the automated LCD-based system can be used

rapidly acquire images from large Gabor filterbanks and using these to study dynamic processes.

CHAPTER 3 : CHARACTERIZING THE OPTICAL SETUP: SENSITIVITY TO CHANGE IN OBJECT SIZE AND ASPECT RATIO

- This chapter includes work published in (84): Pasternack RM, Qian Z, Zheng J-Y, Metaxas D, Boustany, NN. “Highly sensitive size discrimination of sub-micron objects using optical Fourier processing based on two-dimensional Gabor filters.” Optics Express, 17(14), 12001-12012, (2009), and work published in (80), Pasternack RM, Qian Z, Zheng J-Y, Metaxas DN, White E, Boustany NN. “Measurement of subcellular texture by optical Gabor-like filtering with a digital micromirror device.” Opt. Lett. 33, 2209-2211 (2008)

3.1: INTRODUCTION

By applying a Gabor filter to the DMD using the setup, the user can capture a filtered image which is fundamentally a response map to the period (S) and orientation (φ) of that filter measured pixel-by-pixel. By collecting many such filtered images, the user can construct a vector of responses for each pixel studied in the image. In order to characterize the performance of the Gabor filtering approach, it is useful to process this vector of responses into a useable variable. For example, at some point (either within the bandwidth of the system or beyond), the period and orientation of the Gabor filter will be optimally matched with the spatial extent and orientation of the object it is probing, and the response at that pixel will be maximized. Although a response may be found for all filters applied, the best match naturally produces an optimal response. Using the premise, testing of the device requires studying of samples whose sizes and orientations are known.

The first step in this investigation is to establish the theoretical limit of sensitivity to changes in object size under the most ideal conditions possible. To achieve this measurement, a purely periodic phase object (a phase mask) is used whose bandwidth in the

Fourier plane is minimal. This gives an object where SNR is maximized, leaving the frequency resolution of the system as the limiting variable.

The next step was to establish the sensitivity to changes in object size for spatially confined objects. In this case, the optical response in the Fourier plane is broadband, and so the expected sensitivity to changes in object size is reduced. Polystyrene microspheres in acrylamide gels prove ideal samples to study the relationship between the Gabor filter period and object size. They provide high SNR images, are easy to control, and the spherical symmetry of the particles minimizes the dependency of response on filter orientation, allowing me to proceed by considering only S as the independent variable for this study.

The analysis in both these studies relies on the fact that at some point, the response to the Gabor filter will be optimized at an optimal filter period S_{\max} . This parameter is ultimately used as the descriptor for the size measurement. As a first-order approach to extracting this value, the signal at each pixel plotted as a function of S and a Gaussian distribution is fit to the data in the frequency domain using non-linear least-square residual minimization. The choice of a Gaussian arises from the expectation that a Gaussian profile should match the shape of the expected signal from the Gabor filterbank inasmuch as there is a spatial frequency position at which a maximum response occurs. In order to test its performance, the analysis of the data applies this “filter-fit” approach to periodic and finite object samples as described below. Finally, in the next section the performance of the Gabor filtering method is compared with the performance of digital post-processing of unfiltered images.

3.2: PHASE MASK (IDEAL NARROWBAND SAMPLE)

In order to interrogate the performance of the system and to assess its maximum sensitivity to changes in object morphology under idealized conditions, a series of test samples consisting of glass phase masks and polystyrene spheres embedded in polyacrylamide gel were employed. The Gabor filter bank paradigm chosen for these experiments was a size filter bank in order to demonstrate sensitivity to change in object size. The phase masks, generously provided by P. Westbrook of OFS Labs, Somerset, NJ, were studied as suitable narrowband test objects at both high and low magnification. Their Fourier transform consists of a series of harmonically related delta functions in the scatter plane, only the first of which was passed by the NA of the system at 20x. Investigation at 60x with was not attempted, as the oil required would have index-matched the refractive index of the phase mask grooves, rendering the mask nearly invisible. Calibration of the Fourier plane on the DMD gave ~ 150 mirrors at the NA for 20x (0.00781 cycles/ μm /mirror).

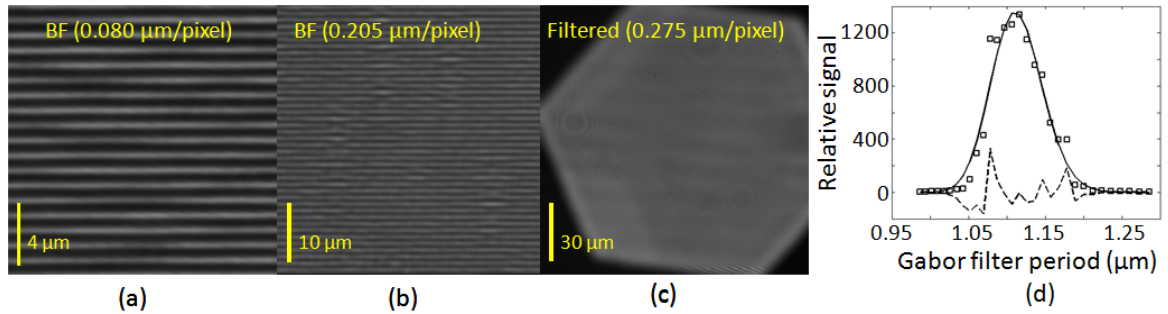


Fig. 3-1. Representative phase mask images. (a) Bright field taken at 0.080 $\mu\text{m}/\text{pixel}$. (b): Bright field taken at 0.205 $\mu\text{m}/\text{pixel}$. (c): Gabor-filtered image filtered at mask frequency, showing the edge of the condenser field stop and taken at 0.275 $\mu\text{m}/\text{pixel}$. Optically filtered images were used for optical processing. (d): Representative plot and fit of signal in a single pixel of a series of filtered images.

The first phase mask studied was an unchirped phase mask with frequency a period of 1.075 μm , while the second was a chirped phase mask with chirp rate of 7.5 nm/mm around a nominal period of 1.05 μm . Both are studied using the above optical scheme with Gabor filtering taking place at the DMD at several points of 1 mm (chirped) or 2 mm (unchirped) intervals with arbitrary independent starting points x_0 imaged at the same

magnification of $0.275 \mu\text{m}/\text{pixel}$ on the CCD. Exposure time at the CCD varied from 2000ms to as little as 50 ms to avoid overexposure when the phase mask delta function in the scatter plane lied directly within the filter bandpass. **Fig. 3-1** illustrates the phase mask while imaged in central dark field and with a Gabor filter applied near the intensity response maximum.

A filter bank of 57 four-layer Gabor-like filters ranging in center frequency from $0.734 \text{ cycles}/\mu\text{m}$ to $1.172 \text{ cycles}/\mu\text{m}$ in one mirror increments ($0.00781 \text{ cycles}/\mu\text{m}$ increment in the frequency range around the nominal frequency near $0.9\text{-}1.0 \text{ cycles}/\mu\text{m}$ of the phase mask) and arrayed in the Fourier plane 90° from the orientation of the phase mask lines were constructed. Because the sample is obviously not spatially confined, the spatial extent of the Gabor-like filters was set to $\sigma_s = S$, widening the confinement area in the image but increasing resolution in the Fourier plane as a result.

Because the Gabor-like filters applied to the DMD lack the complex conjugate to the impulse response, the filtered images are essentially featureless, lacking the stripe pattern visible in the unfiltered images (**Fig. 3-1**). Spatial confinement of the filter is apparent from the preservation of the hexagonal condenser field stop boundary in **Fig. 3-1c**. Despite the narrow bandwidth ($\sim 0.01 \text{ cycles}/\mu\text{m}$) of the phase mask diffraction order, several images taken over a larger range of filter frequencies ($\sim 0.1 \text{ cycles}/\mu\text{m}$ when $\sigma_s = S$) contain signal significantly above background levels due to the width of the Gabor filters. However, signal strength is maximized when the Gabor filter is centered over the diffraction order and decreases as the filter position is moved away (**Fig. 3-1d**).

When interrogating a sample to measure object size through the sample, the Gabor filter responses as a function of S (see example **Fig. 3-1d**), we have established and follow the image acquisition and analysis sequence given in **Fig. 3-2** as given in (84) and elaborated here. First, a filter bank of four-layer Gabor-like filters with increasing center frequency

arrayed radially in the Fourier plane are constructed as illustrated in **Fig. 2-6** (upper right quadrant), and applied sequentially on the DMD while imaging the object. The resulting stack of filtered images (**Fig. 3-2b**) encode the pixel-by-pixel amplitude response as a function of applied Gabor filter frequency and are post-processed digitally to extract morphometric information from the dataset. After normalizing to exposure time, these data (squares in **Fig. 3-2c**) are then fit using non-linear least-squares Gaussian fitting (solid line in **Fig. 3-1d, Fig. 3-2c**), yielding the optimum Gabor frequency giving maximum response at each pixel. The optimum Gabor frequency is converted to optimum Gabor period, S_{\max} , as shown in **Fig. 3-1d**. The data are encoded into color-coded images indicating optimum Gabor frequency (or period) vs. pixel (**Fig. 3-2d**). At each pixel, the value of S_{\max} was then taken as a direct measurement of local phase mask period.

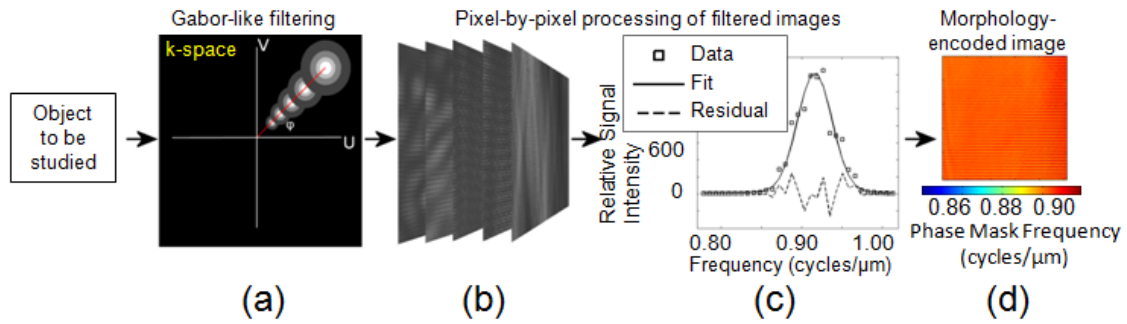


Fig. 3-2. Illustration of DMD implementation of Gabor filter bank and subsequent processing shown here for a phase mask data set. (a): Gabor-like filter bank applied to optical object transform in k-space. (b): Resultant stack of Gabor-like filtered images. (c): Representative fit of filter response as a function of Gabor filter frequency at one pixel of the image stack. Squares represent data points, the solid line represents the fit, and the dashed line represents the residual. (d): Morphometric-encoded image generated from fit for all pixels in the image. The color scale indicates the Gaussian mean resulting from the pixel response fit and thus gives at each pixel the optimum Gabor filter frequency, $1/S_{\max}$, giving maximum response.

Processing of the phase-mask filtered images in this manner for the chirped and unchirped phase masks demonstrates both sensitivity to nanometer-scale changes in chirped phase mask period, and, with correct system calibration, accuracy in measuring unchirped phase mask period. As shown in **Fig. 3-3**, processed pixels near the center of the field of view (the edges are excluded to avoid the condenser aperture) color-coded morphometric images indicating mask order frequency vs. pixel demonstrates that the chirp is detectable

even over 1mm of the phase mask. The Gaussian fit to the Gabor response at each pixel produced a correlation of greater than 80% in >99% of pixels, indicating that the Gaussian data fitting method to extract the position of maximum response is reliable. Analysis of the encoded images of the chirped phase mask produced a mask period vs. stage position relationship (**Fig. 3-3b**) in which the chirp mask period is linearly decreasing with relative position at a rate of 7.6nm/mm (correlation = 0.98), 0.1 nm/mm higher than the provided manufacturer specifications but well within the error of the optical setup. Analysis of the encoded images for the unchirped phase mask produced a nearly constant period ranging from 1.074 ± 0.002 to $1.077 \pm 0.003 \mu\text{m}$, and within 3 nm of the $1.075 \mu\text{m}$ period specified by the manufacturer (**Fig. 3-3b**, gray squares). These results show that at under ideal circumstances, the method can detect nanoscale changes in the parameters of the phase masks, and that at least for periodic objects, the “filter-fit” methodology is both precise and accurate.

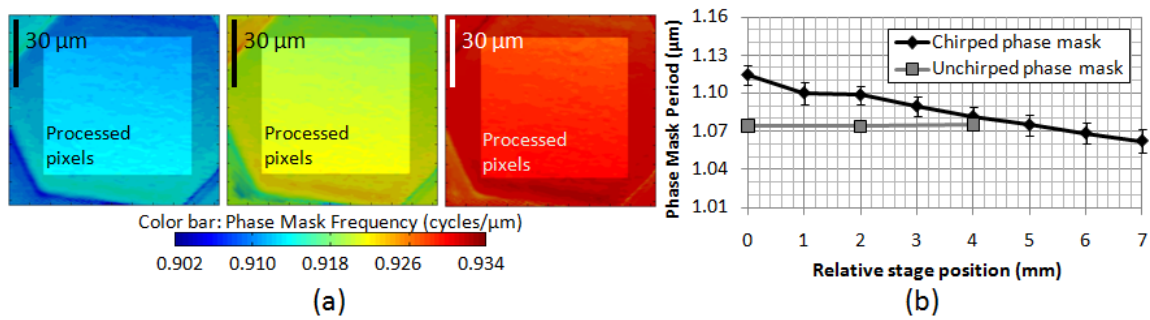


Fig. 3-3. Optical Gabor filtering of phase masks. (a): Left to right: Color-coded images encoding measured phase mask frequency pixel-by-pixel from optical Gabor-like filtering at locations 1 mm, 3mm and 5mm from arbitrary starting point $x_0=0$ on chirped phase mask. Highlighted regions of each image represent ROI used for analysis (pixel rows 80-446 and columns 65-446 of images). (b): Measured chirp as a function of displacement along the chirped (black diamonds) and unchirped (gray squares) phase masks imaged at $0.275 \mu\text{m}/\text{pixel}$ using Gabor-like optical filtering. Data are mean \pm standard deviation of the pixel values included in the processed regions of interest (ROI) (e.g. highlighted regions within the color encoded images in panel (a)).

3.3: POLYSTYRENE SPHERES (HIGH-CONTRAST SPATIALLY CONFINED SAMPLES)

Although using the Gabor filter paradigm is very successful in measuring the phase masks, these samples are not indicative of performance when measuring biological samples,

which are composed of finite objects. In order to discover how well the system performs in detecting changes in the size of finite objects, sphere gels of various sizes were made as in (84). We chose to operate at both 20x and 60x for this experiment, as in this case, both settings may be useful (the former for accessing a wide field of view, and the latter for accessing higher spatial frequencies passed by the system NA).

In 20x, the system is aligned as it was for the phase masks with a $0.275 \mu\text{m}/\text{pixel}$ magnification at the CCD. The same general scheme as outlined in **Fig. 3-2** is once again used to study gels with spheres ranging from $0.271 \mu\text{m}$ to $1.826 \mu\text{m}$ in diameter (sphere sizes were uniform in the sample; spheres were not mixed). **Fig. 3-4** illustrates a representative analysis of the sphere samples. A Gabor filter bank with filters centered on mirrors 50 (corresponding to $0.391 \text{ cycles}/\mu\text{m}$) to 150 (corresponding to $1.172 \text{ cycles}/\mu\text{m}$) was applied to the DMD and each sample was examined using the filter bank. The frequency increment was one mirror (corresponding to $0.00785 \text{ cycles}/\mu\text{m}$), $\varphi = 90^\circ$, and $\sigma_s = S/2$.

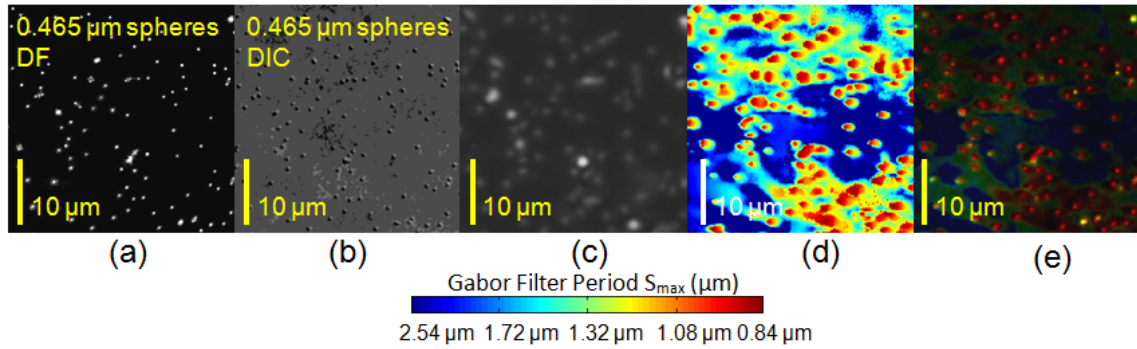


Fig. 3-4. Experimental Gabor filter bank response to finite objects (polystyrene microspheres) at low magnification ($0.275 \mu\text{m}/\text{pixel}$) with 20x objective. (a): Representative Dark Field (DF) ROI ($0.465 \mu\text{m}$ spheres) in polyacrylamide gel. (b): Differential Interference Contrast Image of same ROI. (c): Representative Gabor-filtered image of ROI. (d): Optically processed image encoding optimum Gabor period S_{max} giving maximal filter response. (e): Processed image encoding Gabor filter bank response gated to DF intensity image from Panel (a). For both Panels (d) and (e), color hue encodes filter period S_{max} at which response is maximized and intensity encodes relative fit amplitude.

Each resulting set of optically filtered images (**Fig. 3-2b**, **Fig. 3-4c**) was analyzed pixel-by-pixel using the Gaussian fitting scheme previously described, and an encoded image of optimum Gabor period, S_{max} , (**Fig. 3-2d**, **Fig. 3-4d**) was produced for each sample. This image was then scaled to the dark field intensity image (**Fig. 3-4e**). Sample Gaussian fits to

the optical response at one pixel taken with the 20x objective are shown in **Fig. 3-5**. Each dark field-gated encoded image was thresholded by intensity to include points that are at least 12% maximum intensity, thereby excluding the background but retaining other features. On the remaining pixels that were included which correspond to the locations where features are present, the Gaussian fitting correlation was greater than 80% in >95% of these pixels.

In 60x, the system is aligned to produce a Fourier plane ~ 180 mirrors in radius at the NA on the DMD (0.01229 cycles/ μm /mirror) as described in section 4.1.1 to give a 0.195 μm /pixel magnification (yielding a 100 $\mu\text{m} \times 100 \mu\text{m}$ field) at the CCD. The size range of samples in this case is extended to study spheres up to 2.979 μm in diameter (spheres are once again not mixed). The same general scheme as outlined in **Fig. 3-2** and demonstrated **Fig. 3-4** is used once more. This time, however, we applied filterbanks ranging from mirrors 12-85 on the DMD (corresponding to 0.147 cycles/ μm to 1.045 cycles/ μm) for the 0.771 μm spheres expecting the higher frequencies to be well beyond the position of the expected response maximum. By the same reasoning, expecting the response maximum to be located well beyond the low frequency range of the DMD for the medium-sized spheres (0.465 μm - 0.548 μm), we used filterbanks spanning mirrors 25-120 on the DMD (corresponding to 0.307 cycles/ μm - 1.475 cycles/ μm) to test the medium-sized spheres.

Similarly, we applied a Gabor filter bank with filters centered on mirrors 51 (corresponding to 0.627 cycles/ μm) to 170 (corresponding to 2.089 cycles/ μm - 1.475 cycles/ μm) to study the smallest spheres (0.217 μm and 0.356 μm). The frequency increment was again one mirror (corresponding to 0.1229 cycles/ μm), $\varphi = 90^\circ$, and $\sigma_s = S/2$ as before. Each resulting set of optically filtered images (**Fig. 3-2b**, **Fig. 3-4c**) was again analyzed pixel-by-pixel using the Gaussian fitting scheme previously described, and an encoded image of optimum Gabor period, S_{max} , (**Fig. 3-2d**, **Fig. 3-4d**) was produced for each sample. This image was then scaled to the dark field intensity image (**Fig. 3-4e**).

Sample Gaussian fits to the optical response at one pixel taken with the 60x objective are also shown in **Fig. 3-5**. With the exception of the smallest sphere size (0.217 μm), each dark field-gated encoded image was thresholded by intensity to include points that are at least 20% maximum intensity, thereby excluding the background but retaining other features. The 0.217 μm spheres had to be thresholded to 60% in order to exclude most of the background due to the very low signal from the spheres. On the included pixels which correspond to the locations where features are present, the Gaussian fitting correlation was greater than 80% in >90% of these pixels for sphere sizes 1.053 μm and below. Larger sphere sizes have poorer fits at 60x.

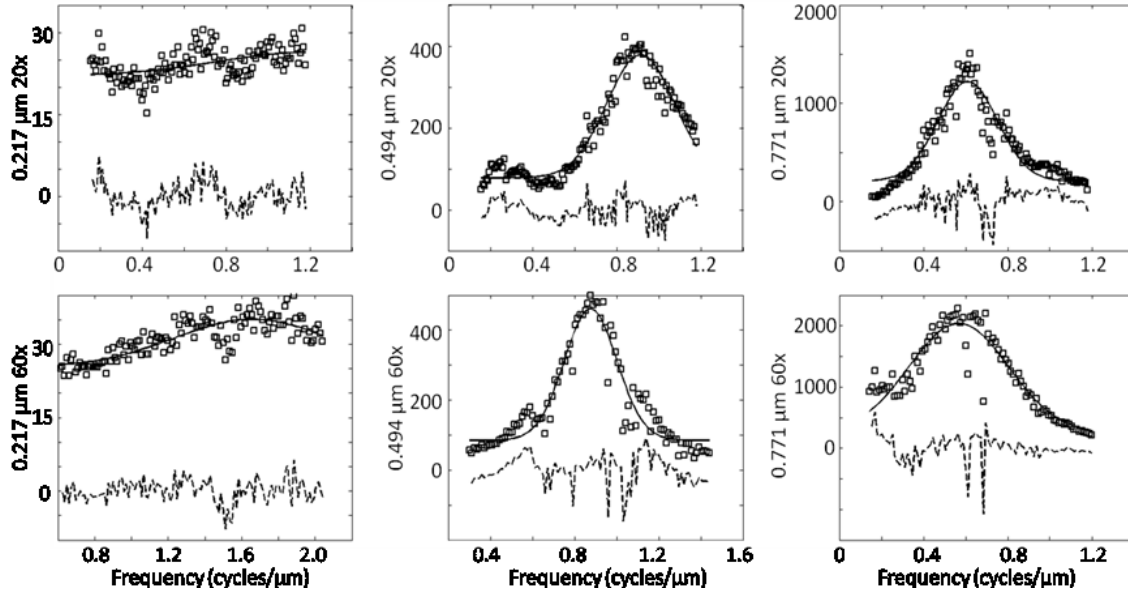


Fig. 3-5. Representative Gaussian fits of Gabor filter response at one pixel for three sphere sizes below 1 μm . Pixel is chosen from regions on which a sphere is present. Ordinate is relative signal intensity. Signal increases with increasing sphere size.

The maximum filter response retrieved from the Gaussian fitting method at each pixel is averaged to yield an average maximum response over the entire pixel region passed for each sphere. Thus, an overall maximum filter response frequency is retrieved for each sphere regardless of the number of pixels occupied. **Fig. 3-6** plots several representative histograms plotting the distribution of S_{max} found for the spheres on a per-object basis. The maximum filter response period is recorded as S_{max} . **Fig. 3-7** shows a linear fits to S_{max} .

plotted against the corresponding sphere diameter using the 20x and 60x conditions for the range of sphere sizes utilized.

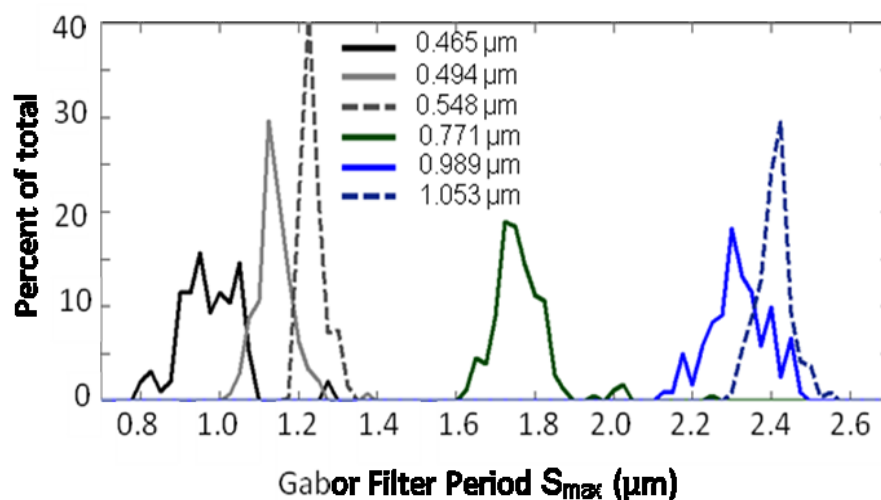


Fig. 3-6. Histogram showing the distribution of Gabor filter periods S_{max} at which local response for each sphere is maximized for sphere sizes ranging from 0.465 μm to 1.053 μm . Each sphere region is derived from the dark-field-gated responses

The performance of the “filter-fit” methodology is inherent in both the extent to which the relationship between sphere diameter and S_{max} is linear and the precision of the measurement. **Table 1** shows the statistical significance of the measured change in S_{max} for each sphere size. Spheres with very similar diameters around 0.5 μm were intentionally chosen to determine the upper limit of sensitivity in the optimal regime of the method’s dynamic range. Even the 0.465 μm and the 0.494 μm spheres, with a difference in diameter of only 29nm, yields p values which near statistical significance at 95% confidence. For the other sphere sizes, all other measurements are statistically significant with the exception of those that fall from the linear fit at 60x in **Fig. 3-7**.

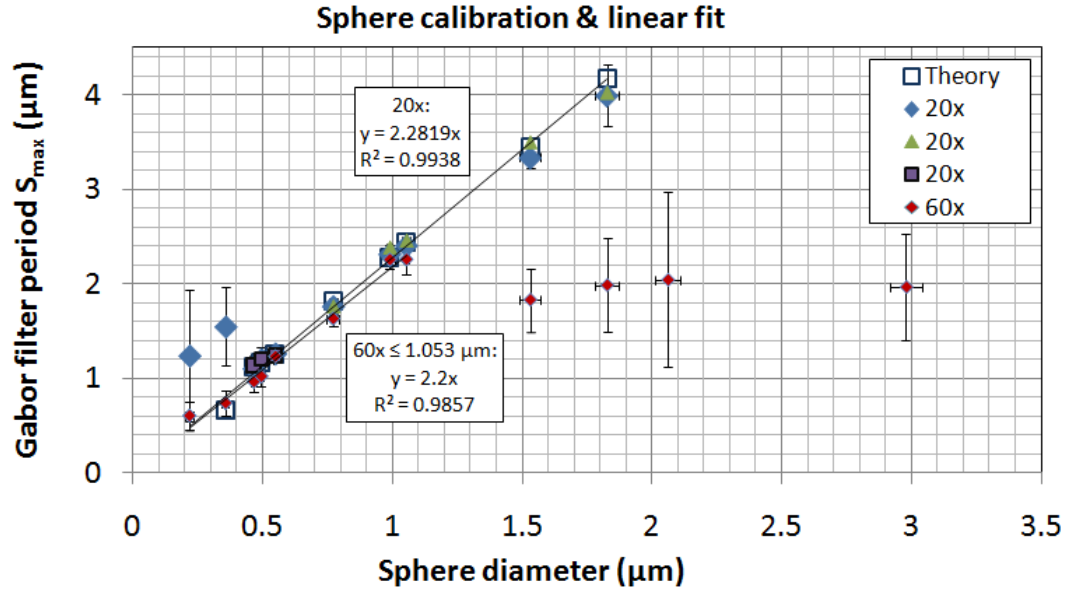


Fig. 3-7. Linear fit (with intercept fixed at zero) to plot of S_{\max} as a function of sphere diameter. Error bars on abscissa are standard deviation of sphere diameter according to sphere manufacturer specifications while error bars on ordinate are standard deviation of the measured mean S_{\max} . For sphere diameter $\leq 1.826 \mu\text{m}$ taken at 20x and for sphere diameter $\leq 1.053 \mu\text{m}$ taken at 60x, the coefficient of correlation > 0.99 .

Table 1. Optical filtering response showing nanoscale sensitivity to spheres with diameter $\sim 500 \text{ nm}$. P value in comparison with 494 nm spheres.

Actual diameter (nm)	Student t-test p value, 20x	Student t-test p value, 60x
$465 \pm 10 *$	$p < 0.08$	$p < 0.07$
$494 \pm 11 *$		
$548 \pm 16 *$	$p < 0.04$	$p < 0.02$

*values are mean \pm standard deviation

For finite objects, the overarching “filter-fit” approach behaves differently from periodic objects (the trivial case). So long as the first diffraction order from the phase mask is passed by the NA, the “filter-fit” method should retrieve the mask period with nanometric sensitivity. However, the dynamic range for measuring the polystyrene spheres has more subtle constraints. Instead of measuring the sphere size directly, the measurement is linearly correlated with sphere size through a certain range. This seems to occur because the Gabor filter bank is primarily probing the forward-scatter main lobe instead of the side-scatter lobes for small spheres. In **Fig. 3-8**, this behavior is illustrated through a simplified simulation of the sphere scatter. To generate idealized versions of the sphere scatter using the same

parameters as those for the sphere-gel system, MieTab scatter simulation software (Prof. August Miller, New Mexico State University) was used to simulate a two-dimensional scatter response series (representative plots **Fig. 3-8a** and **Fig. 3-8d**) which was then subjected to a digital Gabor filter bank (**Fig. 3-8b** and **Fig. 3-8e**). The response (i.e. the integral of the product of the filter and the scatter profile) is then plotted for each filter (**Fig. 3-8c** and **Fig. 3-8f**). This model also simulates the shot noise-limited case in which all noise except that which is intrinsic to the photon statistics is eliminated.

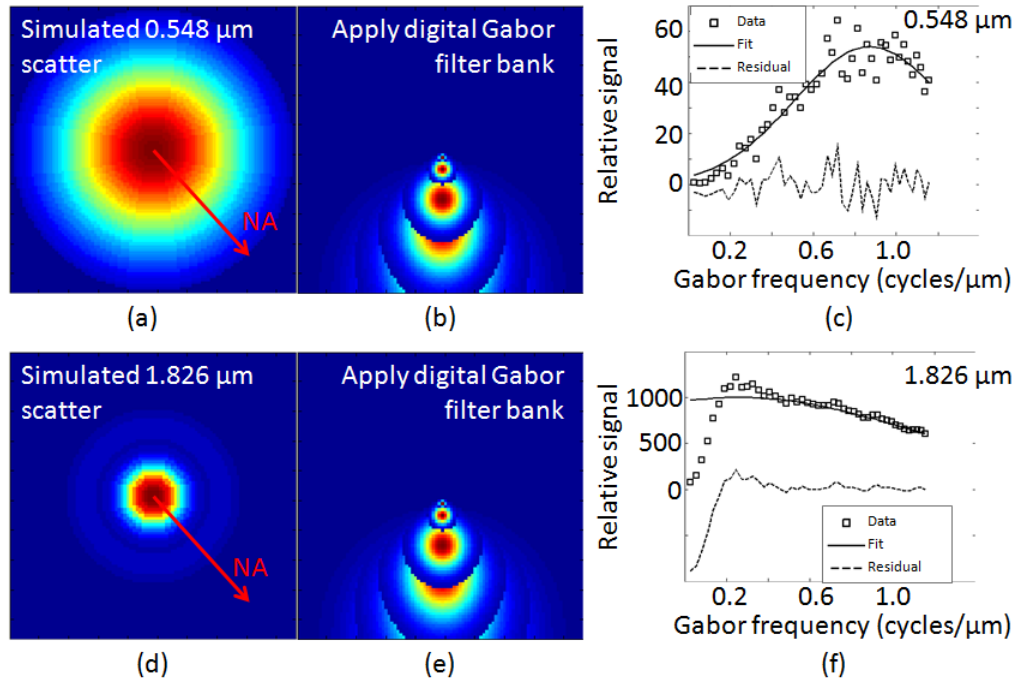


Fig. 3-8. Simulation of Gabor “filter-fit” methodology. (a): Mie-Theory sphere scatter intensity profile generated for 0.548 μm diameter sphere with index ratio $1.56/1.33 = 1.20$ matching that of the sphere samples. Unpolarized light is assumed. (b): Two-dimensional un-normalized Gabor filterbank applied to scatter intensity profile. (c): Plot of signal output from each simulated filtered scatter intensity profile. Signal is normalized to total energy of scatter profile. Shot noise is added with a random vector whose magnitude is the square root of the signal for that simulated filtered scatter intensity profile. (d): Same as (a) but simulating 1.826 μm diameter sphere scatter intensity profile. (e): Applied Gabor filterbank as in (b). (f): Plot of signal output from each simulated filtered scatter intensity profile as in (c) for 1.826 μm diameter spheres.

For sphere sizes smaller than $\sim 1 \mu\text{m}$, the Gaussian filter-fit method works very well; the low residual values imply that the choice of the Gaussian for the data fit is well-justified. However, larger spheres have multiple side lobes passed by the NA, and the scatter profile is no longer monotonic. In this regime, the fit residual grows larger and the fitting algorithm

can easily fail to extract the correct maximum. Additionally, passing more side scatter by either increasing sphere diameter or increasing the NA (or both) exacerbates this behavior. It is also likely that for the largest spheres, the analog beam block at F1 (**Fig. 2-9**) blocks a sizeable fraction of the main lobe of scatter, effectively constraining the dynamic range by cutting off the lowest spatial frequencies.

For finite particles, the range over which the relationship between S_{\max} and sphere size is linear is governed by two constraints. On the lower end, the limit is established by the noise within the signal compared with the degree to which the signal has a detectable peak response. In other words, small particles must both be bright enough to ensure adequate SNR, and enough of the scatter plane must be included so that the scatter profile does not flatten out over this range. This limit is very similar to the limitation on dynamic range for OSI for small particles, and is apparent in the representative fits for the $0.217\ \mu\text{m}$ spheres (**Fig. 3-5**). On the higher end, SNR is no longer a practical concern, as larger particles are many times brighter. However, in this regime the scatter profile is no longer monotonic but oscillatory, creating a Gabor filter response profile that cannot be reliably fit by the Gaussian over the entire range of the profile. The filter-fit method presented here is therefore intrinsically dependent on whether or not the signal decreases monotonically or near-monotonically within the NA. When it is not, another fitting function should be used that is amenable to an oscillatory signal. For the largest sphere sizes, it may be beneficial to use a smaller analog dot or even remove it entirely to eliminate low frequency cutoff.

3.4: COMPARISON WITH DIGITAL POST-PROCESSING

The system design hinges upon analog implementation of the Gabor filtering. This section more clearly describes the benefits of collecting the data after filtering instead of collecting unfiltered images and then processing them digitally. Additionally, this section describes results of a digital post-processing analysis on both the phase mask and the polystyrene sphere samples.

Digital image processing is a proven and powerful tool to interrogate biological samples. In the realm of morphometric studies on mitochondria, digital processing techniques have been developed that morphometrically quantify mitochondrial mass, potential, motility and morphology from confocal microscopy images in both two (85) and three dimensions (86). Mitochondrial swelling was detectable with high-resolution confocal microscopy imaging using a technique that is in essence a digitally implemented version of OSI (87).

All of these methods employ high resolution imaging with fluorescence labeling. The basic theme for each of these methods is therefore high SNR. Indeed, digital processing is extremely powerful so long as this criterion is met. However, there are conditions in which it is not possible or practical to obtain this condition. Long-term incubation with a fluorescent label such as for time-lapse experiments can lead to undesirable effects. Throughput is inherently limited to the high resolution required to image these fields of view adequately for digital processing. In the regime where fluorescent labeling is not desirable or higher-throughput screening is advantageous, the method proposed here recommends itself.

This section presents data demonstrating the limitations of digital post-processing in the undersampled condition, and puts forth an explanation as to why this limitation exists. Both phase mask and sphere images acquired under similar conditions as above are processed digitally in an attempt to achieve the same morphometric sensitivity of the optical processing and “filter-fit” method.

3.4.1: DIGITAL POST-PROCESSING OF PHASE MASK IMAGES

For digital post-processing of the phase mask, unfiltered phase mask images were acquired through the setup by passing all mirrors of the DMD. All images are taken in

bright field in this case to yield non-aliased images at the CCD at $0.080\ \mu\text{m}/\text{pixel}$ and $0.205\ \mu\text{m}/\text{pixel}$ magnification (**Fig. 3-1a** and **Fig. 2-1b**). The images were post-processed digitally using Gabor filters with $\sigma_s = S$ applied in image space. The period of the phase mask was measured at each pixel by optimizing the period of the Gabor filter to give maximum image pixel response. The optimization algorithm utilized an unconstrained nonlinear minimization (Nelder-Mead Simplex Method) and was conducted by Zhen Qian (Former Rutgers BME student in Dr Metaxas' laboratory, presently at Piedmont Heart Institute, Piedmont Hospital, Atlanta, Georgia 30309, USA) in collaboration with this project.

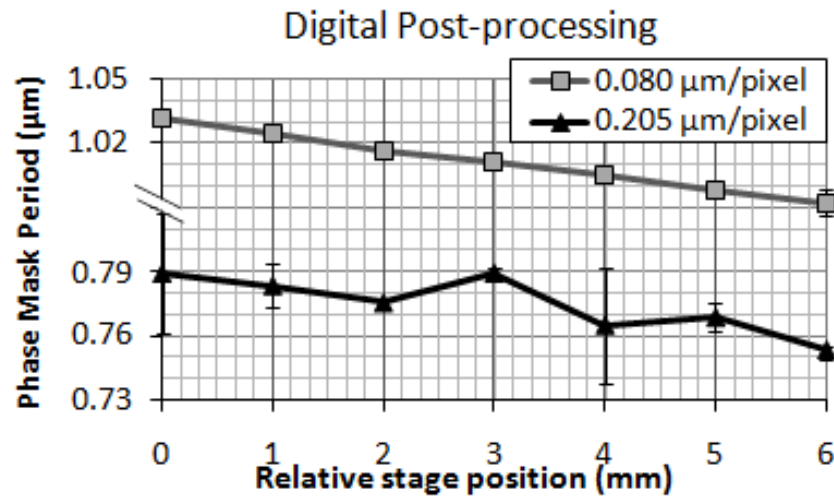


Fig. 3-9. Digital post-processing processing of chirped phase mask. Measured chirp is plotted as a function of displacement along the chirped phase mask imaged in bright field at $0.205\ \mu\text{m}/\text{pixel}$ (black triangles) and $0.080\ \mu\text{m}/\text{pixel}$ (gray squares) and digitally post-processed using Gabor digital filtering. Data are mean \pm standard deviation of the mask periods measured at the pixels included in the processed ROI's within the bright field images. The analyzed ROI's of the unfiltered bright field images were pixel rows 75-448 and columns 75-448.

Fig. 3-9 illustrates the results of digital Gabor filtering obtained by digital post-processing of the phase mask bright field images. When imaged at $0.080\ \mu\text{m}/\text{pixel}$, digital Gabor filtering measures the period to be linearly decreasing with position with a nominal chirp rate of $7.5\ \text{nm}/\text{mm}$ based on a linear fit, exactly the expected value specified by the manufacturer (**FIG. 3-9**, gray line). However, when imaged at $0.205\ \mu\text{m}/\text{pixel}$ (**FIG. 3-9**, black line), a linear fit of the digital Gabor filtering measures a nominal chirp rate of 6.5

nm/mm, significantly lower than the expected value by 1.0 nm/mm. At this resolution, the measured periods range from 0.75 to 0.79 μm , much lower than the high magnification measurement in the same vicinity of the phase mask. Additionally, the phase mask period is no longer monotonically decreasing with incremental movements of the stage. At points 3 and 5, the value of the measured mask period increases from its previous value at the prior position, yielding a positive chirp rate for these two positions. Finally, the error of the measurement is much greater in value at several points than the errors for either high-magnification digital processing (**FIG. 3-9** gray line) or optical processing (**Fig. 3-3**). Both precision and accuracy of digital post-processing is therefore lost when high magnification is no longer used in the image acquisition despite the lack of aliasing in the image.

For the smallest size objects, the optical method is noise-limited. Sources of noise include optical background, shot noise from the detector, sample movement, and geometric effects arising from the DMD (79).

3.4.2: DIGITAL POST-PROCESSING OF POLYSTYRENE MICROSPHERE IMAGES

In the same way in which a regime exists in which the optical Gabor filter method confers an advantage over digital post-processing for the phase mask, this section describes the digital post-processing analysis performed on unfiltered polystyrene microsphere images and demonstrates a similar performance advantage.

Dark-field (DF) and DIC images of the sphere samples collected at 0.275 μm /pixel were Fourier-transformed digitally and filtered using a digital Gabor filter bank with center frequencies ranging from 67 to 206 pixels in radius on the Fourier plane (corresponding to a range of 0.475-1.463 cycles/ μm with frequency increment 0.00710 cycles/ μm) and with $\sigma_s =$

S/2. To account for effects of contrast gradient due to the DIC shear axis, the orientation of the digital filter bank was applied both parallel and perpendicularly to the direction of maximal contrast. The generated filtered image transforms were then reverse-transformed and subject to a digital pixel-by-pixel fit to Gaussian as in an analogous manner as was done for optical processing. After registration, the same pixels from the analog feature analysis are used in the digital analysis, yielding a per-feature histogram of filter responses for each sphere size. The measured filter responses for the DF data overlap and do not have differences in their distribution that are statistically significant (**Fig. 3-10a**). The same is true for the DIC data (**Fig. 3-10b** and **Fig. 3-10c**); however, the standard deviations of the distributions of the contrast aligned DIC analysis (**Fig. 3-10b**) are much smaller than those for the DF digital analysis (**Table 2**). The digital template-matching algorithm used by Qian to digitally study the spheres fared no better than digital Gabor filtering of the spheres, with no statistically significant difference in measured sphere size noticeable for DF (**Fig. 3-10d**) or DIC (**Fig. 3-10e**), with the exception of the $0.494\text{ }\mu\text{m}$ spheres which were actually measured larger than the other two sphere sizes in DIC (**Fig. 3-10e**).

In analog processing, spatial filtering acts on the object E-field directly, while in digital processing, the filtering acts on the digitized intensity image. Analog optical processing therefore confers a sensitivity advantage over digital processing. By decoupling the optical processing with Gabor filters from digital image resolution as collected by the CCD, analog processing relaxes the digital sampling requirements imposed by digital processing, therefore allowing sensitive measurement in undersampled fields of view. Analog Gabor filtering remains sensitive to changes in object despite undersampling of those objects.

Table 2. Digital filtering response to spheres

Actual diameter (nm)	DF		DIC (aligned with contrast)		DIC (misaligned with contrast)	
	Gabor filter period S_{\max} (nm)	Student t-test p value	Gabor filter period S_{\max} (nm)	Student t-test p value	Gabor filter period S_{\max} (nm)	Student t-test p value
$465 \pm 10^*$	$1174 \pm 42^*$	$p = 0.94$	$1003 \pm 94^*$	$p = 0.95$	$1828 \pm 218^*$	$p = 0.53$
494 ± 11	1174 ± 24		994 ± 24		1814 ± 108	
548 ± 16	1162 ± 22	$p = 0.41$	1000 ± 24	$p = 0.97$	1648 ± 42	$p < 0.05$

*values are mean +/- standard deviation

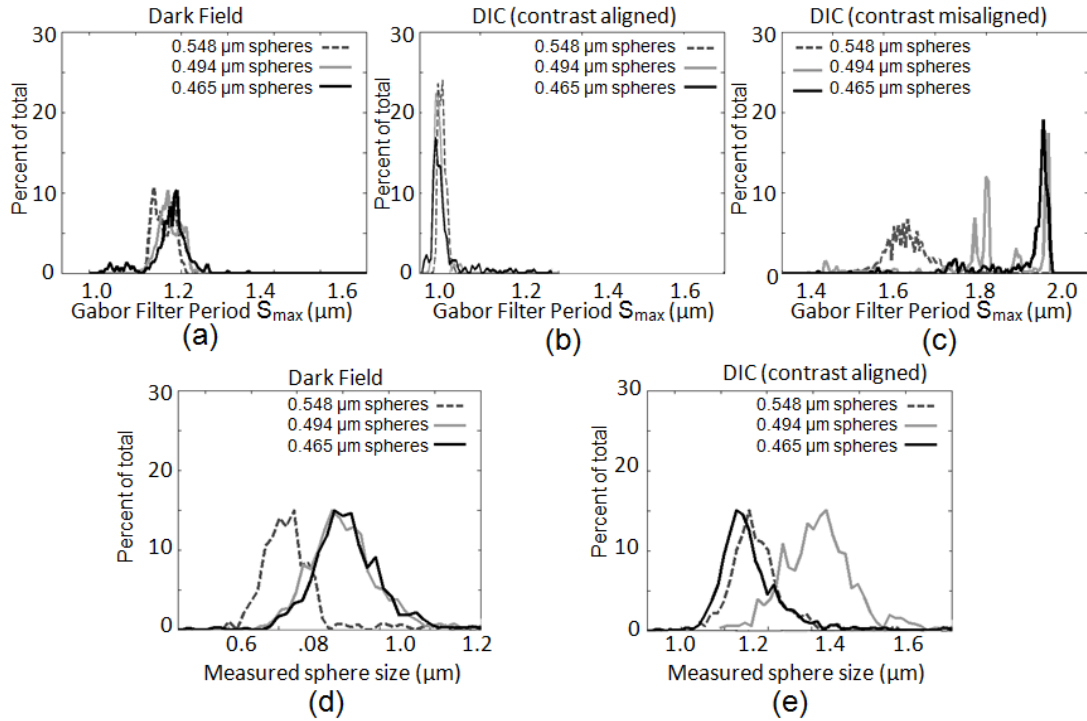


Fig. 3-10. Measurement of sphere size based on S_{\max} values derived from digitally post-processed images. (a): Histogram derived from digital Gabor filter bank applied to dark field image. (b): Histogram derived from digital Gabor filter bank aligned to the axis of contrast applied to DIC image. (c): Histogram derived from digital Gabor filter bank misaligned with the axis of contrast applied to DIC image. (d) & (e): Sphere diameter measured using Gaussian second derivative template-matching algorithm as processed by Qian for dark field and DIC images, respectively.

3.4.3: APPLICABILITY OF THE SENSITIVITY MEASUREMENTS WITH POLYSTYRENE MICROSPHERES

Using polystyrene microspheres as test samples to measure the performance of the optical Fourier filtering technology allowed us to determine the sensitivity to changes in object size. We verified that there is no need to infer object size from an optical scatter

model by retrieving a linear parameter for object size for spheres smaller than $2\text{ }\mu\text{m}$ in diameter. We also demonstrated the importance of conducting the Fourier filtering optically prior to digitization by comparing the performance of analog and digital filtering at equal magnifications. Careful consideration of these data must include the observation that the ratio of the index of refraction between the spheres and their environment, which is proportional to their contrast in the image, is much higher than that of biological phenomena. Biological organelles have refractive index ratios $m \sim 1.04$ ($n \sim 1.4$ for mitochondria) (88), while for the polystyrene spheres in ployacrylamide gel $m \sim 1.2$. The decrease from $m=1.2$ to $m=1.04$ corresponds to an order of magnitude loss of signal due to the reduction in scatter intensity cross section at the lower values of m (**Table 3**).

Table 3: MieTab simulated scatter intensity (Qsca)	
	Qsca (no units)
$m = 1.04$	0.037
$m = 1.12$	0.348
$m = 1.20$	0.974
$m = 1.28$	1.82

Table 4: Effect of m on phase function response to filter bank to $0.548\text{ }\mu\text{m}$ sphere simulation		
Index ratio m	S_{max} (simulation) (μm)	S_{max} (fit) (μm)
1.04	1.556	1.348
1.12	1.556	1.348
1.20	1.575	1.345
1.28	1.612	1.348

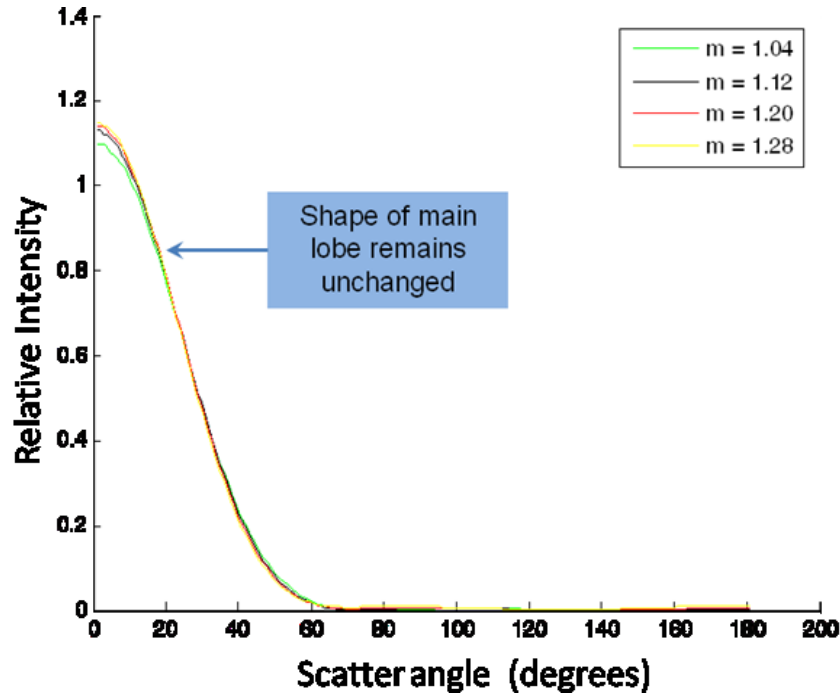


Fig. 3-11. Relative intensity of sphere scatter profile as a function of scatter angle for a sphere of $0.548\ \mu\text{m}$ in diameter with $m = 1.04$ (green curve), $m = 1.12$ (black curve), $m = 1.20$ (red curve), and $m = 1.28$ (yellow curve). Incident light is unpolarized; scatter profiles are cylindrically symmetric.

However, sphere scatter simulations show that changing the refractive index ratio between the measured particle and the medium by changing the refractive index of the particle is not expected to change the shape of the forward scatter lobe appreciably and therefore will not change the relationship between the Gabor filter period S_{max} and sphere diameter (**Fig. 3-11, Table 4**). It should be noted that the effect of changing the index ratio by altering the medium index of refraction has not been tested and may yield changes in shape and/or spatial frequency distribution of the forward scatter lobe. In any case, the net effect of the sphere/gel system on this analysis was to increase SNR in the measurement. This is justified considering that the goal was to ascertain the sensitivity of the optical Gabor filtering method under optimal (high SNR) conditions. As the signal for a biological system with $m = 1.04$ would drop by a factor of ~ 10 , the signal-to-noise (SNR) ratio in a shot-noise limited detection system would drop by a factor of $10^{1/2}$ (e.g. SNR in data of **Fig. 3-5**), from

which signal may still be recovered, albeit with lower sensitivity. Recovering this sensitivity rests squarely on achieving a high SNR acquisition of the data. For such a factor of 10 loss, this sensitivity may be recovered immediately, by using more powerful illumination, or by examining more than one pixel at a time to average the noise out (binning). Given that the fluence at the sample when using this setup is $\sim 0.2 \text{ mW/mm}^2$, accounting for power losses at the diffuser and during coupling into the microscope, the current laser power could simply be increased by a factor of 10 to recover this loss. This would not damage biological samples. Conversely, binning to pixel areas corresponding to $0.5 \mu\text{m} \times 0.5 \mu\text{m}$ (2x2 pixels at the current magnification) could be analyzed while remaining within the resolution of the Gabor filters used. Thus, for cases where the refractive index ratio is low (such as for cellular organelles in cytosol), accurate data collection is a signal to noise issue that can be solved either with a more powerful source of illumination, post-processing averaging, or both, and is not expected to be otherwise affected by index of refraction.

3.5: USING OPTICAL GABOR FILTERS TO DETECT ASPECT RATIO

The motivation for measuring the shapes of structures in an image arises from fundamental importance of shape in the morphology of subcellular processes. Apoptosis involves specific morphological changes that include fairly predictable and ordered shape changes, such as mitochondrial fragmentation (89). The ability of measuring shape reliably and efficiently is therefore of great importance.

Chapter 3, Sections 3.3 and 3.4 develop a method using optical Gabor filters with the DMD-based setup to arrive at a measurement of object size by varying the period of the filter and measuring changes in response. These responses are then fit to a Gaussian to

extract the optimal response, S_{\max} , which maintains a linear relationship with object diameter over biologically relevant size ranges. This section presents a straightforward methodology to extract object shape based on Gabor filter response, specifically the degree to which a particle is oriented in a particular direction. This methodology, unlike the approach to measure object size, does not rely on curve fitting. Rather, by using an orientation-sensitive filter banks such as the one illustrated in **Fig. 2-6** (bottom filterbank) where the Gabor filter angle φ varies while keeping S is held constant, it is possible to measure the response as a function of φ and directly encode an aspect ratio parameter from these values. What follows is a description of how this technique is developed and tested on diagnostic samples using the DMD-based setup.

3.5.1: A STRAIGHTFORWARD METRIC OF ASPECT RATIO: ORIENTEDNESS

Encoding a morphometric parameter for orientedness derived from a Gabor filter bank is much more straightforward than encoding for size. A simple geometric approach for assessing object shape is to measure aspect ratio, which can readily be adapted to a Gabor filter measurement by interpreting the response to a Gabor filter at a given angle as the object's aspect at the perpendicular orientation (the position of the filter in the Fourier plane and the orientation of the object are always rotated by 90°). However, this metric does not use a simple measure of aspect ratio directly. Because such a measurement, i.e. the ratio of maximum dimension to minimum dimension is defined only for objects where these dimensions occur at right angles (e.g. an ellipse). However, the Gabor responses need not be so constrained. Additionally, if the minimum response is small, the ratio can become unreasonably large or even singular.

Therefore, deciding against using aspect ratio (in this case as the ratio of maximum Gabor filter signal to minimum Gabor filter signal), the method instead defined a parameter that takes into account all of the Gabor filter responses. This parameter, named orientedness, is defined as the ratio of maximum Gabor signal to average Gabor signal for all filters (i.e. $O = S_{\max}/S_{\text{avg}}$). O is calculated pixel-by pixel across the field of view to generate a morphometric encoded image in which orientedness is visualized. The minimum value for S_{avg} occurs when all responses other than S_{\max} are zero (in this case $S_{\text{avg}} = S_{\max}/N$). The maximum value for S_{avg} occurs when all responses are the same (i.e. $S_i = S_{\max}$) in this case $S_{\text{avg}} = N \cdot S_{\max}/N = S_{\max}$. N is the number of filtered responses measured as a function of ϕ . The value of S_{avg} is therefore constrained such that $S_{\max}/N \leq S_{\text{avg}} \leq S_{\max}$, and the value of O is also constrained such that $1 < O < N$. Although this implies that the range for aspect ratio is constrained to the number of filters used, actual values of orientedness approaching N are not observed to occur because this would imply that all response for the filterbank is collected from a single filter. Because of the broadband scatter of real objects, this situation is highly unlikely. Therefore, the orientedness parameter, when defined in this way, provided a convenient descriptor of object shape that may be readily calculated from a series of appropriately filtered images and is stable between a predictable range.

3.5.2: APPLYING OPTICAL GABOR FILTERS TO HIGHLY ORIENTED STRUCTURES IN MARINE DIATOMS

The first task, after developing the orientedness parameter definition, was to apply the measurement to a predictable sample with highly oriented features. These studies began by choosing a filterbank period S for which filters varying in φ are applied. Choosing $S = 0.9 \mu\text{m}$ should highlight particles $\sim S/2$ ($0.45 \mu\text{m}$) in diameter, which should highlight various structures of this size within the diatoms. Finally, the filterbank angle of rotation was incremented by 20° such that $0^\circ \leq \varphi \leq 160^\circ$.

The sample used to test the orientedness approach consisted of an assortment of marine diatom skeletons in glass (Carolina Biological Supply Company). The skeletons have clearly visible, highly-oriented structures in a variety of shapes and sizes depending on the diatom species. The set of nine Gabor-filtered images of the diatom were processed pixel-by-pixel for object orientation and roundness. Processing consisted of (step 1) summing measured responses of all 9 Gabor-filtered images at each pixel to determine the overall magnitude of the signal response and (step 2) finding the orientedness as described, and the Gabor filter orientation, φ , at which the response is maximized. In effect, the first parameter encodes the magnitude of the overall response and the second parameter encodes the extent to which objects at each pixel have a preferred orientation. **Fig. 3-12** shows a representative marine diatom with highly oriented structures throughout (**Fig. 3-12a**). The orientedness response (**Fig. 3-12b**) quantifies the orientedness of the marine diatom's structures. The morphometric image is plotted so that the intensity of the response is encoded as pixel brightness, while the orientedness response is encoded as hue (blue for areas of low orientedness and red for areas of high orientedness). In order to confirm the accuracy of the measurement, the angle φ at which the Gabor filter response is maximized is converted to spatial orientation, θ , where $\theta = \varphi + 90^\circ$, and plotted as a quiver plot for high-intensity (response greater than 10% of maximum) pixels. This check allows for confirming that the angle of the maximum response correctly corresponds to the orientation of the objects. In this diatom, the edges of the structure are clearly captured around the periphery as well as the textured interior (oriented at $+45^\circ$ in the object). Satisfied that this approach can measure the variation in orientedness within an object, the technique can now be applied to

living cells.

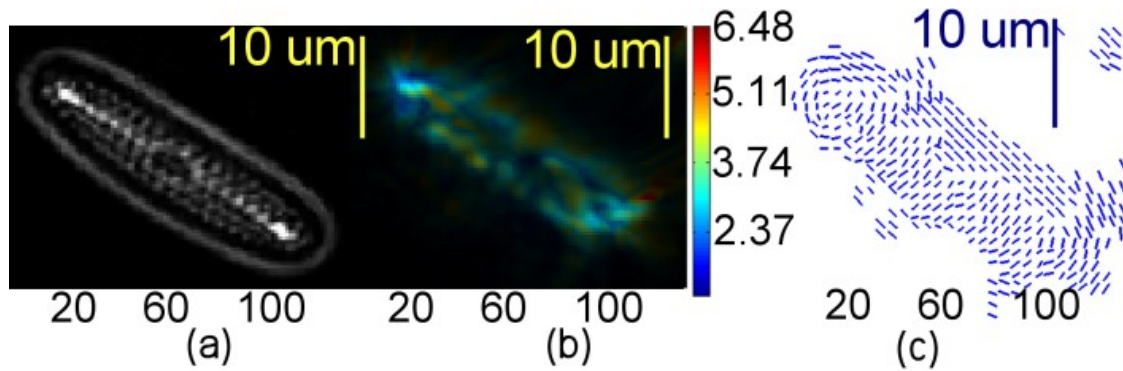


Fig. 3-12. Marine diatom samples for sensing oriented structures. (a): Dark field image of diatom. (b): Object orientation image. Color scale indicates degree of orientation (aspect ratio) while brightness encodes significance of the total Gabor filter response. (c): Orientation of objects with response intensity 10% of maximum. Line segment indicates the corresponding structure's long axis.

3.6: DEMONSTRATION OF RAPID, AUTOMATED GABOR FILTERBANK ACQUISITION WITH THE LCD-BASED SYSTEM: COLLAGEN FIBER FORMATION

The LCD-based system was automated by Bryan Rabin (90) and could be applied to rapidly acquire filtered images in sequence for dynamic processes. As a demonstration of its capabilities, collagen fiber network formation was chosen as a test sample to evaluate the performance of the LCD-based system and to develop data processing motifs to analyze the large amount of data generated from large filterbanks and automated acquisition. The collagen solutions were kindly prepared by Shirley Masand of Dr. D. Shreiber's lab in the dept. of Biomedical Engineering at Rutgers.

Gabor filtering was used for quantitative measurement of the collagen sample texture. Filter banks with filter orientations $\varphi = 0^\circ$ to $\varphi = 345^\circ$ in 15° increments were used for collagen imaging. Five such filter banks with filters with period $S = 0.6 \mu\text{m}$, $S = 0.9 \mu\text{m}$, $S = 1.2 \mu\text{m}$, $S = 1.8 \mu\text{m}$, and $S = 3.6 \mu\text{m}$ were used with Gaussian envelope standard deviation $\sigma = S/2 \mu\text{m}$ for all filters. These periods correspond to radii of 240, 160, 120, 80, and 40 pixel elements on the SLM, respectively.

The automated interface then collects a series of filtered images, each corresponding to each filter applied. This stack of images can then be visualized and processed in order to extract morphological information of interest.

3.6.1: COLLAGEN PREPARATION AND IMAGE ACQUISITION:

677 μL acid-soluble type I lyophilized collagen from calf skin (Elastin Products Company, Owensville, Missouri, USA) is doped with 5% FITC-conjugated type I lyophilized collagen from calf skin, acid-soluble (Elastin Products Company). This mixture is prepared at 3mg/mL in 0.02N acetic acid in 0.22 μm -filtered distilled water. 323 μL of buffer solution consisting of 20 μL Hepes buffer (Invitrogen, Carlsbad, California, USA 92008), 140 μL 0.1 N NaOH in distilled water, 100 μL 10x modified eagle medium (MEM, Sigma-Aldrich, St. Louis, MO 63178), 52 μL Medium 199 (M199), 10 μL L-glutamine (Sigma-Aldrich) (20 mM in 0.22 μm filtered deionized water), and 1 penicillin/streptomycin (P/S) (Sigma-Aldrich). The buffer solution and collagen solution are mixed forming the complete collagen solution and is chilled and stored over ice until use.

Immediately before use, 5 μL of the complete collagen solution are pipetted onto a 75 mm x 25 mm 1mm thick specimen slide and immediately covered with a No. 1 coverslip, allowing the collagen solution to spread throughout the area of the coverslip by capillary action. Samples are then mounted for study at room temperature. To study collagen fiber formation, the Gabor filter banks are applied in time intervals of 20 seconds, with each filtered image collected at 50ms exposure on the Cascade CCD. Therefore, each 20 seconds interval consists of 18 seconds during which image acquisition takes place, and 2 seconds of delay. At each time point, unfiltered dark field images are collected immediately before and after each stack of Gabor filtered images on the Cascade CCD. Unfiltered dark-field and Gabor-filtered background images were collected in the same way by replacing the

collagen sample with 5 μL of 0.22 μm filtered deionized water. The background images are subtracted from the corresponding collagen images before data analysis.

3.6.2: DATA ANALYSIS

After background subtraction, the analysis of the signal at each pixel of the filtered images uses principal component analysis (PCA) to incorporate the response from every filter in order to arrive at a manageable and meaningful morphometric parameter. The parameter "orientedness" (Chapter 3, Section 3.5) is inadequate because it is defined for only one filter period S . In this study, the filterbank used comprises filters with five values for S ($S = 3.6 \mu\text{m}$, $S = 1.8 \mu\text{m}$, $S = 1.2 \mu\text{m}$, $S = 0.9 \mu\text{m}$ and $S = 0.6 \mu\text{m}$), necessitating the development of a more general morphometric parameter. Importantly, the use of PCA preserves the ability of encoding response aspect ratio.

The PCA approach operates by reorganizing the Gabor-filtered data collected at each pixel into a matrix whose structure is determined from the Gabor filter parameters. The Gabor filter response R is fundamentally a function of axial θ and azimuthal φ angle of scatter. The axial angle θ is defined as the declination from the vertical of the angle of optical scatter and related to the Gabor filter period S by the diffraction relationship given in Chapter 2: $S^{-1} = f_s = n \times \sin(\theta) / \lambda_o$, where f_s is now the spatial frequency position of the Gabor filter. The Gabor filter response R may then be cast as a vector in spherical coordinates originating from the origin with magnitude R in the direction given by (θ, φ) (**Fig. 3-13**). Defining θ as declination from the adjacent axis as opposed to inclination from the normal plane allows straightforward representation in standard spherical coordinates and conversion from spherical to Cartesian coordinates x, y, z as follows:

$$R_x \mathbf{x} = R \cos(\varphi) \sin(\theta) \mathbf{x} \quad (\text{Eq. 4-1})$$

$$R_y \mathbf{y} = R \sin(\varphi) \sin(\theta) \mathbf{y} \quad (\text{Eq. 4-2})$$

$$R_z \mathbf{z} = R \cos(\theta) \mathbf{z} \quad (\text{Eq. 4-3}),$$

where R_x , R_y , and R_z are the components of R in the directions of unit vectors \mathbf{x} , \mathbf{y} , and \mathbf{z} , respectively. R is thus decomposed into 3 orthogonal spatial components for every filter response at each pixel. For a dataset consisting of N filters, this yields a response matrix $\mathbf{X}_{N \times 3}$ of size $N \times 3$ at each pixel. PCA is performed on $\mathbf{X}_{N \times 3}$ by invoking the Eigenvalue problem (Eq. 4-5) after finding the 3×3 covariance matrix \mathbf{C} (Eq. 4-4) of the whitened data:

$$\mathbf{C} = 1/(N-1) \sum_{i=1}^{N-1} (\mathbf{X}_{N \times 30_i} - \bar{\mathbf{X}}_{N \times 3}) (\mathbf{X}_{N \times 30_i} - \bar{\mathbf{X}}_{N \times 3})' \quad (\text{Eq. 4-4}),$$

$$\mathbf{D} = \mathbf{V}^{-1} \mathbf{C} \mathbf{V} \quad (\text{Eq. 4-5}).$$

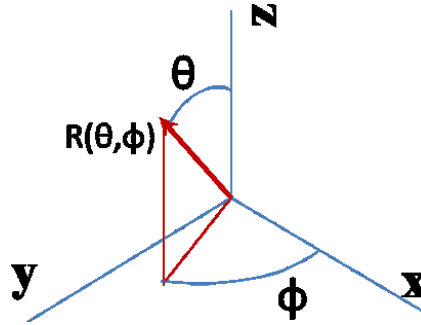


Fig. 3-13. Representation of the single-pixel Gabor filter response in $\langle \mathbf{x}, \mathbf{y}, \mathbf{z} \rangle$ defined by the Gabor filter parameters θ and φ .

\mathbf{D} in Eq. 4-5 is the diagonal matrix of Eigenvalues and \mathbf{V} is the 3×3 matrix whose columns are the eigenvectors in \mathbf{x} , \mathbf{y} , and \mathbf{z} . Fig. 4-8 shows a representative principal components from data analyzed using the technique described above.

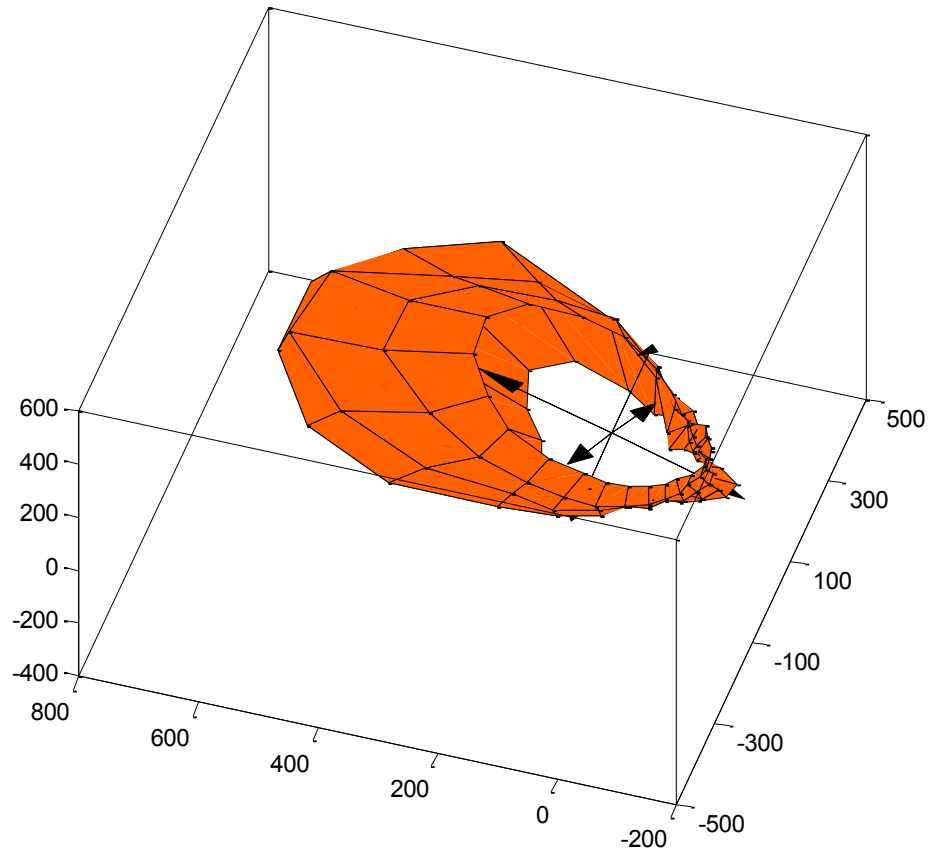


Fig. 3-14. Representative data (orange) arranged into spherical configuration based on (θ, φ) of the Gabor filters and corresponding principal components (blue) calculated from PCA analysis.

Of particular interest are the Eigenvalues in D because these describe the magnitude of each principal component. Differences in magnitude equate to a differential filter response in θ and φ and thus can be developed into a metric describing the degree to which a response is oriented. Orientedness in this analysis retrieved from the maximum aspect ratio of the response (i.e. the maximum ratio R of eigenvalues E given as $R = \max(E)/\min(E)$). By using PCA, this analysis approach arrives at a morphometric parameter tantamount to orientendess regardless of the choices of S . This analysis occurs independently for each pixel used in the field of view.

3.6.3: COLLAGEN TIME LAPSE RESULTS AND ANALYSIS

The purpose of studying collagen gelation is first a test of acquisition performance and speed, but is also a test-bed for data analysis and rendering. Several methods of data analysis and rendering are used here and throughout the remainder of this thesis.

Fig. 3-15 shows a representative collagen sample at several time points during gelation. Initially, the collagen sample appears largely void, with few bright particulates in the DF image. There is also little structure associated with the corresponding aspect ratio encoded image (**Fig. 3-15a**). However as time progresses, filamentous structures rapidly form and grow, and by 10 minutes the fiber growth reaches completion (**Fig. 3-15d**). The morphometric encoded images accompanying the DF images are generated by using the PCA analysis routine pixel-by-pixel across the image and then scaling the intensity in the image to the overall PCA response (taken as the sum of the resulting eigenvalues). Thus, in these images, hue represents aspect ratio and intensity represents overall response. Such a rendering is extremely useful as it quantitatively ascribes the morphometric parameters of response and aspect ratio directly in an image that registers with the underlying structures. For example, the morphometric image suggests that the filamentous regions (indicated by the yellow arrows, **Fig. 3-15d**) are more oriented than the clumped regions (indicated by the cyan arrows, **Fig. 3-15d**). Thus, such images are useful in guiding the analysis toward areas of specific interest based on spatial distribution of the measured parameter.

It is possible to conduct global analysis of the PCA aspect ratio data to study the evolution of the sample in time. In **Fig. 3-16**, the pixels corresponding to >10% of maximum response in the morphometric encoded images of **Fig. 3-15** are studied to yield a time trace of aspect ratio during collagen growth. Excluding pixels by using a threshold minimizes the inclusion of background, and exclusion of background is in general a

necessary step in analysis of the morphometric data given in this thesis. **Fig. 3-16** shows that aspect ratio begins at a high value but increases further as gelation progresses. This analysis reveals that this increase occurs mostly between 100 and 300 seconds. The presence of high aspect ratio initially may indicate the presence of oriented structures that are difficult to see in DF images (**Fig. 3-15a**) but nonetheless contribute a significant response.

It is also possible to examine local regions of interest and directly study the signal arising from individual structures as in **Fig. 3-17**. A very useful method for studying the Gabor signal is to organize each response for a pixel (or small ROI of pixels as in **Fig. 3-17**) into a polar plot. The polar plots are generated by placing the Gabor-filtered signal from the ROI into positions (S, φ) corresponding to the (S, φ) filter parameters. This allows for direct inspection of the distribution of signal in a Fourier plane-like rendering. In **Fig. 3-17**, such an approach was used on two local regions in the collagen sample with structures oriented approximately perpendicular from each other. Little signal is apparent at $T = 0$ in this region

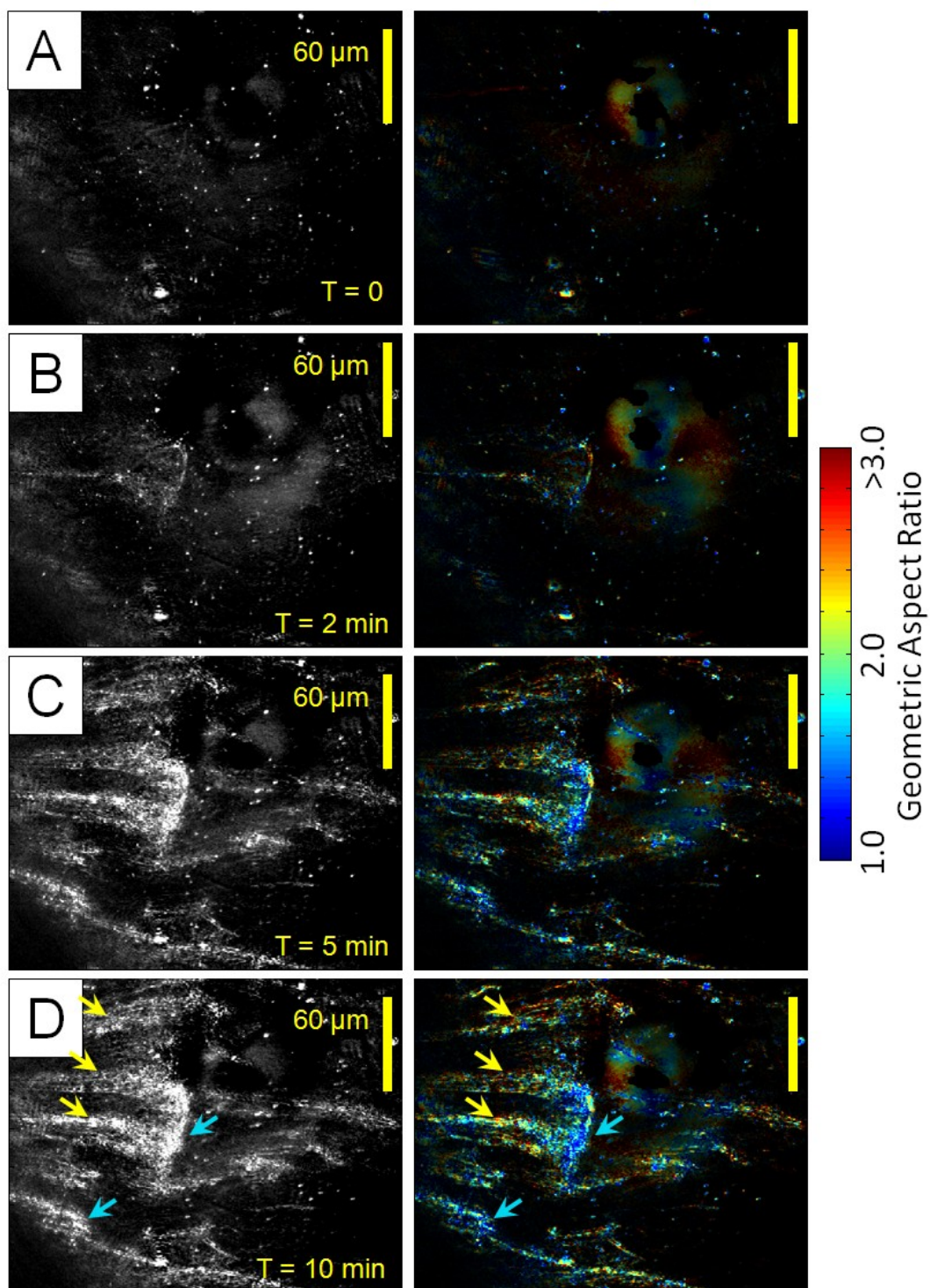


Fig. 3-15. Collagen gelation visualized using PCA analysis on Gabor filter signal. Left panels are unfiltered DF while right panels are encoded for aspect ratio (hue) and overall response amplitude (brightness) based on pixel-by-pixel PCA analysis. Responses are scaled according to Little structure is apparent at $T = 0$ (a). As time progresses, structures appear and brighten (b,c), and by 10 minutes the process is largely complete.

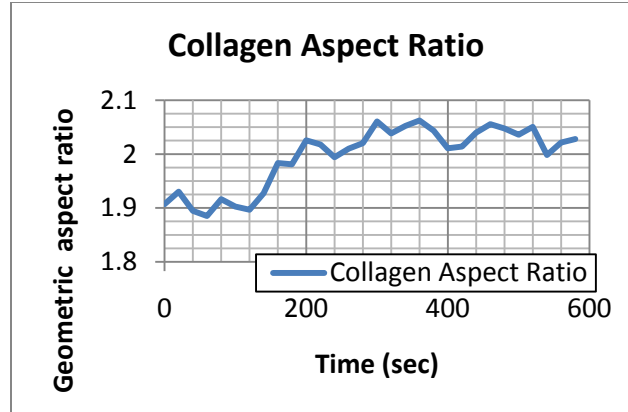


Fig. 3-16. Time trace of aspect ratio during collagen gelation. Only pixels of >10% maximum response are included.

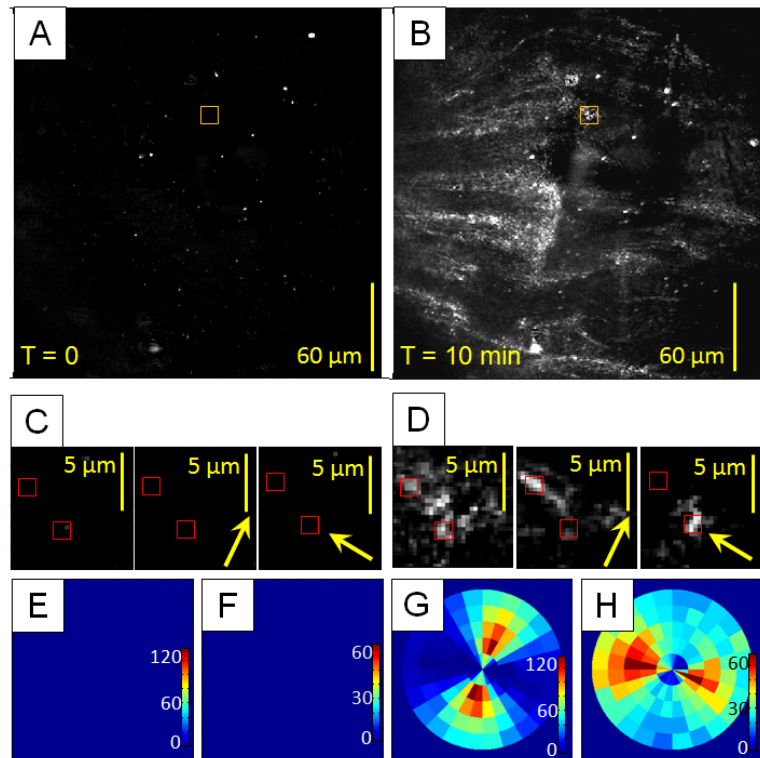


Fig. 3-17. Local analysis collagen gelation ROI. (a): DF image of collagen sample at $T = 0$. (b): DF image of collagen sample at $T = 10$ min. Local neighborhood of ROIs studied is given by orange squares in the center top of (a) and (b). (c): Local neighborhood of (a) in DF (left panel), filtered image for Gabor filter with $S = 0.9 \mu\text{m}$, $\varphi = 60^\circ$ (center panel), and filtered image for Gabor filter with $S = 0.9 \mu\text{m}$, $\varphi = 150^\circ$ (right panel) at $T = 0$. Orientation of the respective filters are given by the yellow arrows (Center and Right panels, respectively). (d): Local neighborhood of (b) as in (c) at $T = 10$ min. Orientation of the respective filters are given by the yellow arrows (Center and Right panels, respectively). The pair of filters highlights different structures in the DF image. Red boxes in (c), (d) constitute 5x5 pixel ROIs for which polar plots of signal are rendered in (e-h). (e): Polar plot of signal from upper left ROI in (c) highlighting structures oriented at 60° at $T = 0$. (f): Polar plot of signal from upper left ROI in (c) highlighting structures oriented at 150° at $T = 0$. (g): Polar plot of signal from upper left ROI in (d) highlighting structures oriented at 60° at $T = 10$ min. (h): Polar plot of signal from upper left ROI in (d) highlighting structures oriented at 150° at $T = 10$ min.

(**Fig. 3-17e, f**), but by $T = 10$ minutes the polar plots show markedly different distributions of signal for each region (**Fig. 3-17g, h**). Polar plots allow for close inspection of local regions of interest and can give a representative glimpse into the data as a whole. In this case, the structures studied (red ROIs, **Fig. 3-17c, d**) are oriented approximately perpendicular to each other, although from the DF image itself this is not immediately obvious.

3.7: DISCUSSION

To recap, this chapter reports on the DMD optical Gabor filter methods capabilities in detecting differences in object sizes and aspect ratio under ideal conditions. Optical Gabor-like filters were used to measure the change in the period of phase masks and to measure the change in diameter of polystyrene microspheres. Optical Gabor-like filters were used to measure the change in the period of phase masks, and in the diameter of polystyrene spheres. The results demonstrate that optical processing is sensitive to a 7.5 nm change in the period of periodic phase masks (**Fig. 3-3b**) and is also successful at discerning finite particle sizes down to a sensitivity of 30nm as determined from polystyrene spheres ~ 500 nm in diameter (**Fig. 3-6, Fig. 3-7, Table 1**). This sensitivity is achieved despite digital aliasing in the filtered images acquired on the CCD. In contrast, and as expected, digital post-processing of aliased object images shows that there is insufficient sensitivity to detect the change in sphere size using either DIC or DF contrast. Moreover, digital post-processing results are dependent on the method of imaging contrast used.

The results from digital post-processing of non-aliased periodic phase mask images indicate that high magnification is required for digital Gabor filtering to be successful (**Fig. 3-9**). The confinement of the Gabor filter to two wavelengths in the image lowers the

resolution of the filter in the frequency plane to such an extent that the bandwidth of the phase mask is much smaller than the bandwidth of the filter for all magnifications used here. What matters most, then, is the resolution of the image, in which oversampling in the image is the only remaining way to significantly increase sensitivity to the analysis. Therefore, because higher magnification is the only reliable way to improve accuracy of digital processing even when the object is not aliased, the dependency of digital processing on sampling is its primary limitation. This is also expected to be especially apparent for finite objects in which only one “period” of the object exists and where spatial confinement of the filter is essential.

Compared with digital post-processing, the optical processing method presented places the constraints of sensitivity solely in the sampling of the Fourier plane by the spatial light modulator; there is a much more lenient limitation on image resolution and staircasing error is eliminated by operating prior to digital sampling. Optical processing of the object’s period or size characteristics prior to digitization is particularly advantageous if the final digital result is aliased and should in general allow for imaging undersampled fields of view, potentially allowing significantly greater throughput in analyzing object morphology.

In this study, we used the optimum Gabor period, S_{\max} , giving maximum response as a measure of object size at each pixel. S_{\max} was obtained after fitting a Gaussian to the pixel response curve vs. Gabor filter frequency (**Fig. 3-5**). We chose the Gaussian because it is capable of extracting a local maximum (if one exists) necessary for the analysis within the data set while making few other assumptions about the remainder of the data. It is positive for all possible values of frequency, as a real signal should be as well. However, it is important to note that the Gaussian function was only used here to retrieve objectively and

reproducibly the spatial frequency position of the maximum response and for this purpose resulted in good fits with good correlation values. The nature of the actual response function will in general depend on the product of the Gabor filter with the object's transform, and may not be known a priori for arbitrary samples. Better function choices could ultimately be made for specific objects where the shape of the scatter is known. This technique is similar to OSI (72), in that it measures the change in signal of the forward scatter lobe of the particle relative to spatial frequency. However, by probing the angular scatter distribution of the particles finely with Gabor filters instead of implementing an optical scatter image ratio based on the intensity ratio of wide-to-narrow angle scatter as in OSI, better size discrimination may be achieved. This technique has additional advantages in that it is sensitive to detecting the shape of the angular scatter profile, can be used without a scatter model, and implements optimal spatial confinement of the filtered image via Gabor filtering.

Additionally, the parameter S_{\max} intrinsically describes the object size in the correct units of length, and the data in **Fig. 3-7** show that the relationship between S_{\max} and object size is linear for particles with diameter between $0.2\mu\text{m}$ and $1\mu\text{m}$ when imaged at $\text{NA} = 1.4$ and for particles with diameter between $0.5\mu\text{m}$ and $2\mu\text{m}$ when imaged at $\text{NA} = 0.75$. The linear relationship between the sphere size and Gabor period is supported by the 0.99 correlation coefficient (**Fig. 3-7**) although more sphere sizes would need to be tested in similar fashion to better define the dynamic range of this relationship. In particular, the sensitivity to the size of particles which are significantly below the resolution of the optical system will decrease due to signal truncation from the numerical aperture. This begins to be apparent in the broadening of the size distributions for the smaller sphere sizes in the histograms from **Fig. 3-5**. The slope of this relationship is also likely to depend on the

shape of the finite objects being measured. Thus, although the parameter S_{\max} is highly sensitive to changes in object size, it may not measure the absolute object size accurately in a sample consisting of objects other than spheres. Nonetheless, a linear relationship is still expected to retrieve relative changes in object size accurately in all cases. A linear relationship between S_{\max} and object size imparts this technique with an advantage over spectroscopic methods, which require a scattering model of the spectrum in order to translate spectral changes into change in object size measured in the correct units of length (72). The method presented here is therefore relevant for monitoring cell morphology in living samples, where the ability to detect subtle relative changes in structure without assumptions of a model may be of greater value than measuring absolute size accurately.

The current technique is an extension of OSI (72) and exhibits the same tradeoff between frequency sensitivity in the Fourier domain and image resolution in the space domain. The Gabor filter half-width in the image plane defines the extent of the object area being analyzed and is inversely proportional to the filter half-width in the Fourier plane. Due to their Gaussian envelopes, Gabor filters confine the band-pass filtering to local spatial areas. They also simultaneously achieve the optimal localizations in both the spatial and the spatial-frequency domains (83).

With respect to aspect ratio, the marine diatom and collagen gelation demonstrations illustrate perhaps the greatest strength of the Gabor filter - its inherent ability to detect texture, shape, and orientation. The marine diatom demonstrates the use of a DMD as a spatial Fourier filter that can be used to quantify the orientation and geometrical aspect ratio of complex structures, and is therefore useful in direct study of the shape of subcellular organelles.

Similarly, the collagen gelation experiment explores a method that arrives at aspect ratio of large data sets in addition to demonstrating high-speed acquisition on the LCD system. As a proof of principle, the results assure that it is possible to acquire data using large filterbanks in a stable, automated platform with sufficient time resolution to more closely probe biological phenomena. The collagen demonstration requires the use of more sophisticated analysis in order to synthesize a morphometric parameter. In this case, PCA was used to find the eigenvalues and eigenvectors of the data organized into a coordinate space based on the filter parameters directly. The eigenvalues were then used to calculate aspect ratio for the data which can be used to detect changes in structure from complex structures.

The subcellular-level information obtained from the orientedness method can be therefore be greatly increased by increasing the filter bank to include higher precision in the angular variation of the filter as well as additional choices of Gabor-like filter periods S to probe particles with varying width. Furthermore, although the Gabor filter technique essentially measures angular scatter information, it does not rely on a scattering model such as Mie theory. The morphometric features of the sample are directly characterized by their differential response to Gabor filters with different dimensions and orientations. This technique is therefore applicable to non-spherical organelles for which a precise theoretical scatter description is not easily given, and provides distinctive morphometric parameters that can be obtained within living cells to assess their function.

In conclusion, we have extended our first implementation on the DMD and LCD as a spatial Fourier filter (80) by using filter banks that use additional choices of Gabor-like filter periods S and φ to probe variations in object size and shape. This technique does not

rely on a predictive scatter model, and the morphology of both finite and periodic objects can be probed with very high sensitivity at low image resolution. It is expected that this technique will be useful in high-throughput morphological analysis of subcellular dynamics in greatly undersampled fields of view. The following two chapters describe how the optical Gabor filtering technique can be applied to study living cells undergoing apoptosis in an effort to demonstrate the capabilities of the method, and to develop the means of ascribing the changes in Gabor filter response to their structural origins.

CHAPTER 4 : DETECTION OF MITOCHONDRIAL FISSION DURING APOPTOSIS WITH ORIENTATION-DEPENDENT OPTICAL FOURIER FILTERS

- This chapter includes work published in (91), Pasternack RM, Zheng J-Y, Boustany NN. “Detection of mitochondrial fission with orientation-dependent optical Fourier filters”, *Cytometry Part A*. 79A(2):137-148, (2011), and in (92), Pasternack RM, Rabin B, Zheng J-Y, Boustany NN. “Quantifying subcellular dynamics in apoptotic cells with two-dimensional Gabor filters.” *Biomed. Opt. Expr.* 1(2), 720-728 (2010).

The previous chapters establish methods whereby the optical Gabor filtering technique can be used to measure changes in both size and shape with the appropriate choice of filterbank. In this chapter we investigate whether morphometric measurements during apoptosis can be associated with specific structures. For this study, the orientedness parameter is based on the Max/Avg calculation as described in Chapter 3, Section 3.5 and does not utilize the PCA and aspect ratio formalism of Chapter 3, Section 3.6. Both the DMD-based system and the LCD-based system were used in this study.

The results of this study demonstrate that imaging based on Gabor filters shows a significant decrease in the orientation of subcellular organelles at 60-100 min following apoptosis induction. Furthermore, this event is concomitant with mitochondrial fragmentation observed by fluorescence. The optical scatter changes can be detected at low resolution at the whole cell level. This work also develops a method whereby at high image resolution, one may combine fluorescence imaging of the mitochondria with optical Fourier-based imaging to demonstrate that the dynamic decrease in organelle orientation measured by optical Gabor filtering is spatially associated with fluorescent mitochondria and remains largely absent from nonfluorescent subcellular regions. These results provide strong evidence that the optical Gabor responses track mitochondrial fission during apoptosis and

can be used to provide label-free, rapid monitoring of this morphological process within single cells.

4.1: CHANGES IN GABOR FILTER RESPONSE DURING APOPTOSIS ARE SPATIALLY ASSOCIATED WITH MITOCHONDRIA

There are currently no standard assays that are specifically designed to quantify mitochondrial dynamics in an efficient rapid throughput setting. The morphology of mitochondria can be assessed by electron microscopy (44) or by high resolution fluorescence microscopy to allow observation, segmentation, and measurement of individual organelles within living cells (10; 25; 87; 93). However, these techniques have low throughput and can be experimentally demanding or costly to implement on a routine basis. Moreover the use of fluorescence labels can sometimes interfere with biological function.

Thus, one of the long-term aims underlying the results presented in this study is to investigate the feasibility of developing a rapid light-scattering-based cell assay to quantify subcellular morphological changes associated with mitochondrial dynamics. In the context of this thesis, this study was also aimed at investigating the feasibility of detecting mitochondrial fission during apoptosis with the Gabor filter approach in order to ultimately utilize this signal as a marker of apoptosis. This chapter, presents a proof-of-concept for detecting mitochondrial fission using the Gabor filters that we developed. The results of this study also suggest that the optical Gabor filtering modality remains sensitive to mitochondrial fragmentation at low image resolution and thus could be applicable to label-free, rapid screening of mitochondrial fission in large fields of living cells.

4.1.1: MATERIALS & METHODS

CELL CULTURE

Bovine Aortic Endothelial Cells (BAEC, Clonetics Lonza, Chicago, IL) are cultured as previously described (92) in 0.22 μ m-filtered low-glucose Dulbecco's Modified Eagle Medium (Invitrogen, Carlsbad, CA) supplemented with 10% FBS (Invitrogen), 1% L-Glutamine (100x) (Invitrogen), 9mg/mL bovine brain extract (Lonza), 10,000 u/mL Heparin (Sigma Chemical, St Louis, MI), and 1% penicillin/streptomycin (Invitrogen). For fluorescence imaging, the cells are incubated with growth medium supplemented with 100 nM Mito-tracker green (Invitrogen) for the last 45 minutes of incubation prior to viewing. For optical viewing, the cells are grown to ~50% confluence on no. 1 glass coverslips (Fisher Scientific, Pittsburgh PA). Coverslips are then mounted onto a steel plate (**Fig. 4-1**) for viewing. The steel plate has a ~1 cm hole drilled through the center with smaller channels on either side to allow for dispensing medium. A clean, unused coverslip is then attached with vacuum grease to the top side of the hole, effectively creating a sandwich in which the cells lie on the inside of the bottom coverslip. The space between the two coverslips is flushed 3x and finally filled with viewing medium (CO₂- independent Leibovitz L-15 medium (Invitrogen) supplemented with 10% FBS at room temperature and room air). The bottom coverslip of the sandwich (with cells attached to the interior facing the medium) is sealed to the steel plate by applying VaLaP (a 1:1:1 mixture of vaseline, lanolin, and paraffin) wax. A soldering iron on the low setting (~15 W) is used to melt the VaLaP and dispense molten VaLaP to the bottom coverslip edge. The completed cell sandwich is illustrated in **Fig. 4-1**. Immediately upon completing the cell plating, the cells are imaged as described.

Apoptosis was induced by exchanging the cells' normal viewing medium for viewing medium containing 1 μ M staurosporine (Sigma Chemical) prepared from a 4mM

staurosporine stock solution in DMSO (Sigma). Control studies consisted of loading L-15 + 10% FBS with DMSO only in the same volume in place of the STS solution.

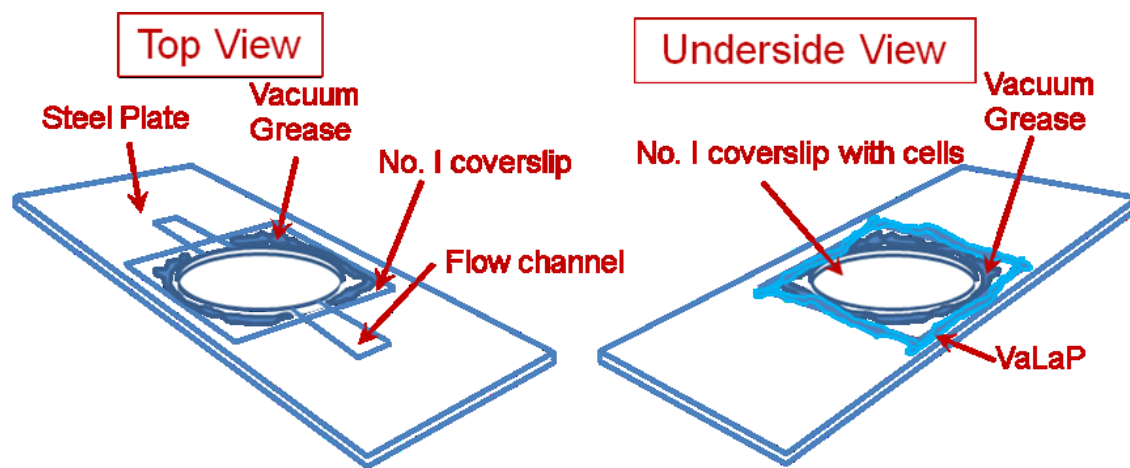


Fig. 4-1. Mounting the cells for imaging. The steel plate is machined with a 1 cm centered hole with channels halfway through the plate on either side of the hole. The top coverslip is mounted first with vacuum grease. The coverslip with live cells facing the inside of the chamber is then mounted on the bottom (Underside View) with vacuum grease. Medium is inserted into the space between coverslips by pipette. Finally, a layer of VaLaP is applied to the edge of the bottom coverslip to form a watertight and rigid seal.

APOPTOSIS ASSAY

BAEC are grown on coverslips as described above and then treated under experimental conditions with STS or DMSO for 3 hours. The coverslips were then rinsed with PBS 3x, fixed with 4% paraformaldehyde in PBS at room temperature for 15 minutes. Then, after 3x rinsing with PBS, the cells are permeabilized with 0.1% Triton-100 + 0.1% sodium citrate in PBS at room temperature for 5 minutes and then blocked with 2% FBS in PBS for 60 min at 37 °C. Cells are then incubated overnight at 4 °C with a fluorescently conjugated antibody to cleaved Caspase-3 (Asp175) (Alexa Fluor 488 Conjugate, #9669, Cell Signaling Technology, Danvers, MA) diluted at 10 µg/ml (1:100 dilution) in blocking solution and mounted on microscope slides sealed with nail polish for imaging.

OPTICAL IMAGING AND FOURIER FILTERING

All samples with the exception of those acquired at high time resolution are studied with the DMD-based optical Fourier processing microscope described in (80) fitted and

aligned with a 63x oil immersion objective with numerical aperture (NA) = 1.4, or a 20x dry objective with NA=0.75 (Carl Zeiss, Gottingen, Germany). For Fourier filtering, light from a ~5 mW Helium-Neon laser ($\lambda_o = 632.8$ nm) was passed through a spinning diffuser and coupled into a multimode fiber whose output was collimated and launched into the microscope's condenser aligned in central Köhler illumination (NA<0.05) to provide a spatially coherent plane wave illumination of the sample. Optically filtered images were acquired on a Cascade 512B charge-coupled device (CCD) (Roper Scientific, Trenton, NJ). Fourier filtering was achieved with a TI0.7XGADMD 1100 Digital Mirror Device (DMD) (Texas Instruments, Dallas, TX) placed in a conjugate Fourier plane outside the microscope side port (**Fig. 2-2**). Using the diffraction pattern of a graticule with known line spacing, the position of each mirror in the plane of the DMD is calibrated against spatial frequency. This calibration is performed for each of the two objectives utilized in this study (the 63x oil immersion and the 20x dry objective). Spatial frequency in cycles/ μm is taken as $n \times (\sin\theta) / \lambda_o$. θ is the diffraction angle incident on the objective, and n is the refractive index of the medium in front of the objective.

Gabor filtering is implemented on the DMD as described in Chapter 2, Section 2.2.2. An orientation-sensitive filter bank is used, consisting of Gabor-like filters with orientations $\varphi = 0^\circ$ to $\varphi = 180^\circ$ in 20° increments (**Fig. 4-2, Inset 1**). In the object space, the filters have a period $S = 0.9 \mu\text{m}$ and a Gaussian envelope standard deviation $\sigma = S/2 = 0.45 \mu\text{m}$. In the present study, this period, S , corresponds to a spatial frequency, $1/S$, positioned on mirror 91 on the DMD when using the 60x objective, and mirror 141 when using the 20x objective.

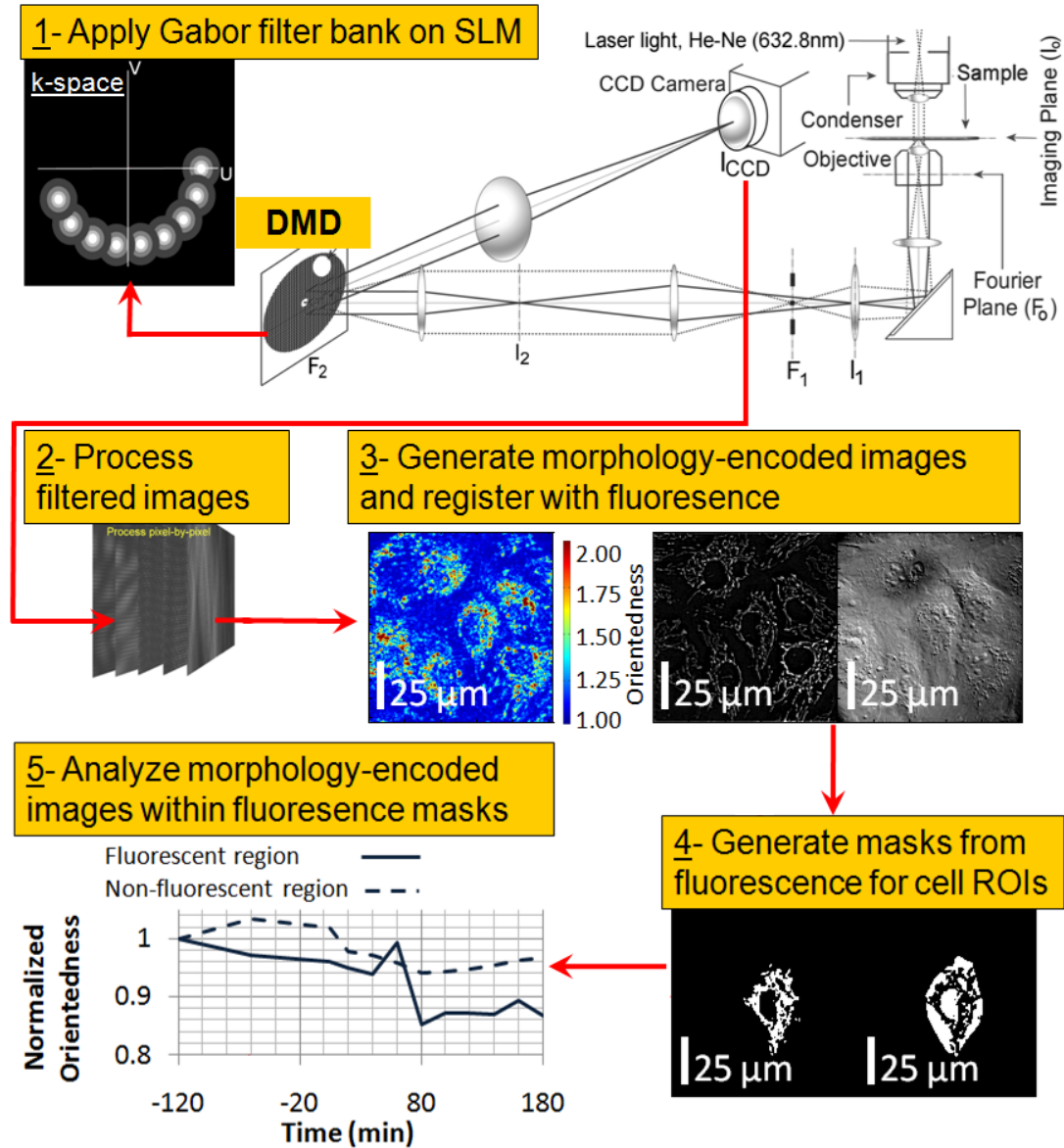


Fig. 4-2. Optical setup and data processing. The light scattered by the sample is Fourier-filtered by the DMD (Inset 1). The stack of filtered images (Inset 2) collected on the CCD is processed pixel-by-pixel and results in morphometrically encoded images (color-coded image) of the object that can be registered directly with the fluorescence and DIC images (Inset 3). Masks segregating bright fluorescent regions from dim ones for each cell ROI at each time point (Inset 4) allow study of orientation dynamics within regions dominated by mitochondria and those dominated by non-fluorescent subcellular structures (Inset 5).

Fluorescent imaging of the mitotracker-labeled cells is accomplished with a FTTC filter cube (filter No. 10; Carl Zeiss, Gottingen, Germany) with 450-490 nm excitation bandpass, and emission collected through a 510 nm dichroic mirror followed by a 515- 565 nm bandpass filter. Fluorescent image acquisition is accomplished without Fourier spatial

filtering, bypassing the DMD by sending the light through the trinocular port of the microscope to a CoolSnap CCD (Roper Scientific, Trenton, NJ). Differential interference contrast (DIC) images were also acquired on both the Cascade and the CoolSnap CCDs to aid in image registration. DIC imaging on the Cascade utilized the low NA laser illumination at $0.633\mu\text{m}$ used for optical Fourier filtering; for DIC imaging on the CoolSnap a higher illumination NA was used by briefly bypassing the $0.633\mu\text{m}$ incident laser light by mounting a collimated blue 470nm LED (Thorlabs, Newton, NJ) to the microscope's condenser arm and opening the condenser aperture.

For dynamic study of apoptosis, the Gabor filter bank is applied in time intervals of 20 minutes over a three hour time after STS addition, with each filtered image collected at 6000ms exposure. Before STS treatment, and for the cells treated only with DMSO (controls) the optical data were acquired every 50-60 minutes. At each timepoint, unfiltered dark field and DIC images are collected immediately before each stack of Gabor filtered images on the Cascade CCD. DIC and fluorescent images are taken on the CoolSnap CCD immediately after collection of the filtered image stack. Gabor-filtered background images consisting of imaging an empty glass sample are collected with 6000ms exposure at the start of each experiment at every filter angle φ , and subtracted from the corresponding filtered images collected during dynamic studies.

DATA ANALYSIS

The background-subtracted Gabor-filtered images are registered with the DIC and fluorescence images. For each time point, the degree of particle orientation, defined as “orientedness”, is extracted at each pixel from the Gabor-filtered images by taking the ratio of maximum to average signal response as a function of Gabor filter orientation, φ , as

described in (80), thereby generating “orientedness” response maps of the object (**Fig. 4-2, Insets 2-3**).

At each timepoint, each cell in the field of view is segmented manually into a region of interest (ROI). For whole cell studies, we track the mean orientedness within each ROI (and thus each cell) by plotting the average pixel value within the ROI over time. The mean orientedness per cell is then averaged over all cells studied to yield an average plot of orientedness as a function of time after STS or DMSO treatment. For subcellular analysis, fluorescence labeling of the mitochondria is used to determine the location of mitochondria within the cells studied at high resolution (using the 63x objective). Unsharp masking of the raw fluorescence images is achieved by applying a Gaussian lowpass filter with standard deviation $2\mu\text{m}$ to the raw image and subtracting this image from the raw image (**Fig. 4-3a-Fig. 4-3b**). This generates a high-contrast background-corrected fluorescence image highlighting the fluorescently labeled mitochondria (**Fig. 4-3c**). The background-corrected fluorescence image is convolved with a digital Gabor filterbank consisting of filters with the same orientation, period and Gaussian envelope as the Gabor filters implemented optically on the DMD ($\varphi=0-180^\circ$ in 20° increments, $S=0.9\mu\text{m}$, $\sigma=0.45\mu\text{m}$). These digitally filtered fluorescence images are then averaged resulting in a Gabor-resolved fluorescence image (**Fig. 4-3d**) with the same spatial resolution as the optically filtered data.

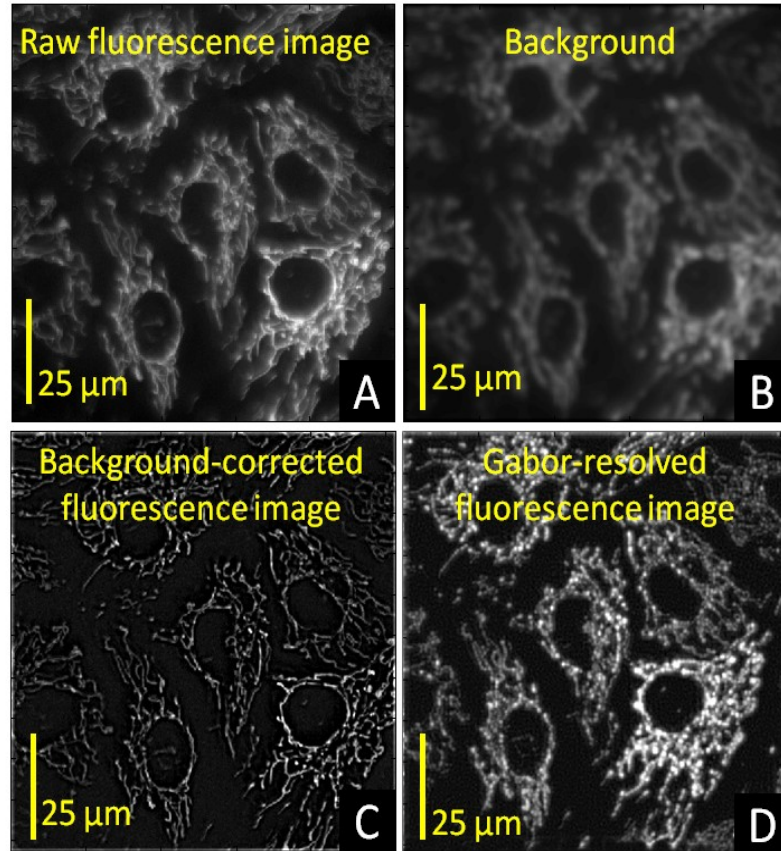


Fig. 4-3. Fluorescence image processing. The raw fluorescence image (A) is filtered with a lowpass filter. This generates a background image (B) which is then subtracted from the original image to generate a high-contrast mitochondrial fluorescence image (C). A digital Gabor filterbank with the same orientations, period and Gaussian envelope as the DMD Gabor filters used in the optical setup is applied to the background-corrected fluorescence image to yield a fluorescence image with the same spatial resolution as the optically filtered images (D).

The processed fluorescence signal within each cell ROI is intensity-thresholded using the mean of the ROI fluorescence intensity as the threshold level. This process is repeated at each timepoint for each field of cells studied. The choice of threshold is discussed in the Results section. Within each cell ROI, this thresholding procedure generates two sets of subcellular regions, one dominated by bright fluorescent mitochondria and the other by the remaining dim background (**Fig. 4-2, Inset 4**). All pixels within each single cell ROI are included in this analysis. The bright and dim fluorescent areas are then separately applied as a mask to the orientedness encoded Fourier processed images to compare the changes in

particle orientedness within the areas rich in mitochondria versus regions dominated by non-fluorescent subcellular structures (**Fig. 4-2, Inset 5**).

4.1.2: RESULTS

DETECTION OF SUBCELLULAR DYNAMICS AT LOW MAGNIFICATION

We first acquire images at low resolution using the 20x objective (NA=0.75, 0.625 $\mu\text{m}/\text{pixel}$) to investigate if we can detect changes in light scattering at the whole cell level in a relatively large field of view. At each time point, we apply the Gabor filterbank to the whole field of view. As described in Methods, we generate morphometric images encoding orientedness (**Fig. 4-4**), which corresponds to the amount of particle orientation at each pixel. The resolution of the corresponding fluorescence images is inadequate to discern any changes in mitochondrial morphology. However, the orientedness data derived from the optical scatter measurements using the Gabor-like filters show that orientedness markedly decreases between 20 and 120 minutes after STS was added as compared with control (**Fig. 4-4b, Fig. 4-4c**), indicating a drop in object aspect ratio despite the poor image resolution.

VALIDATION AT HIGH RESOLUTION

To investigate the source of the morphological changes detected by optical Fourier filtering at low resolution, we repeat the studies at high image resolution with the 63x NA=1.4 objective (sampling at 0.195 $\mu\text{m}/\text{pixel}$). At high resolution in the fluorescent images, mitochondria evolve from a long, filamentous morphology to shorter, smaller and rounder shapes between 60 and 120 minutes (**Fig. 4-5** see arrows in middle panels). During this time, orientedness (**Fig. 4-5**, bottom panels) decreases in the morphometric images. We observe a similar dynamic behavior in orientedness as found at low resolution (**Fig. 4-6**).

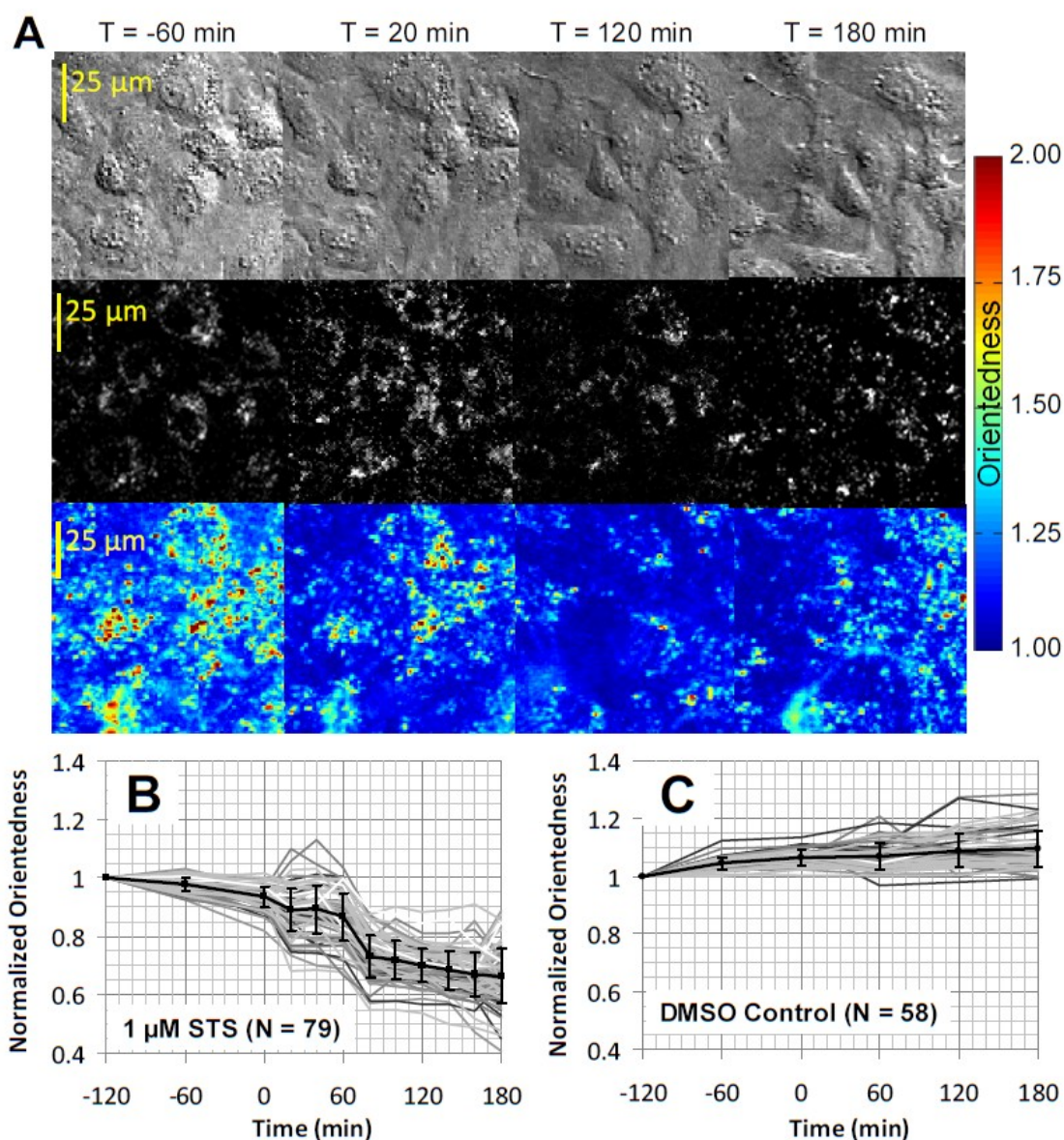


Fig. 4-4. Orientedness derived from Gabor-like filter responses for BAEC studied at low resolution (objective NA=0.75, 0.625 μm/pixel). A: Images of BAEC exposed to STS taken -60 min, 20 min, 120 min. and 180 min. from STS exposure (T=0). Top: DIC. Middle: Fluorescence images of labeled mitochondria. Little difference in mitochondrial morphology is discernible at these time points at low resolution. Despite this, the morphometric images encoding orientedness (color scale in bottom panels) report a decrease in orientedness as a function of time after STS addition. B, C: Time traces plotting the mean orientedness within individual cells treated with STS (gray traces in B) or DMSO (gray traces in C). In B-C, the solid bold black trace represents the mean \pm standard deviation of the individual gray traces. The data were normalized to T=-120 min.

The resolution gained in the fluorescence image allows for breaking down each cell ROI into two subcellular regions – bright, mitochondria-rich areas in the fluorescence

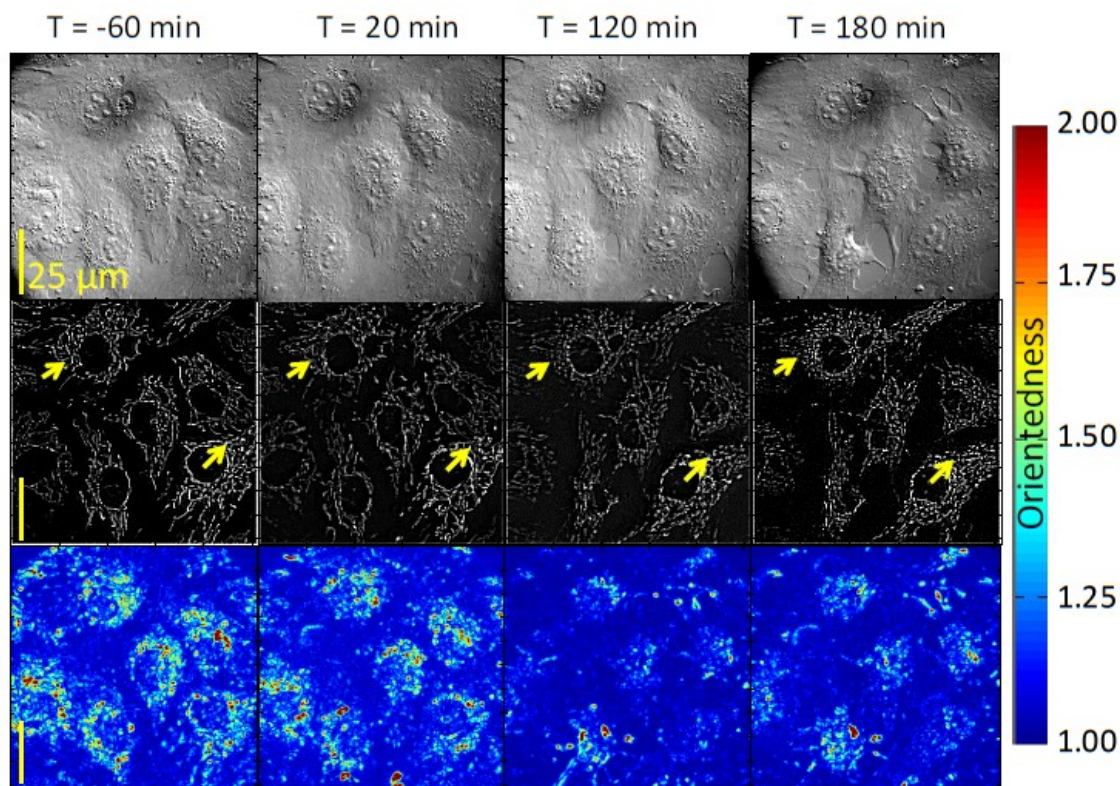


Fig. 4-5. High resolution study of BAEC exposed to STS (objective NA= 1.4, 0.195 $\mu\text{m}/\text{pixel}$). A: Images of BAEC exposed to STS at -60 min, 20 min, 120 min. and 180 min. from STS exposure ($T=0$). Top: DIC. Middle: Fluorescence images of labeled mitochondria. Arrows point to fragmenting mitochondria. Bottom: Morphometric images encoding orientedness (color scale) reporting decrease in orientedness as a function of time after STS addition at $T=0$.

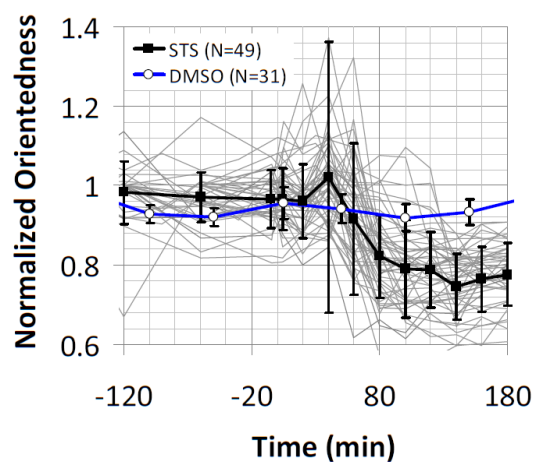


Fig. 4-6. Time traces plotting the mean orientedness within individual cells tested at high resolution (objective NA= 1.4, 0.195 $\mu\text{m}/\text{pixel}$) and treated with STS (gray traces). Bold black trace with solid squares represents the mean +/- standard deviation of the gray traces of cells exposed to STS. The blue trace with open circles corresponds to the average orientedness per cell +/- standard deviation as a function of time for DMSO control. The STS data were normalized to $T=-180$ min.; the DMSO data to $T=-200$ min.

images and dim, mitochondria-poor ones – by applying the thresholding method discussed in the Methods to each cell ROI at each time point. We exploit the high resolution condition to implement this segregation in order to investigate whether the dynamics observed in the cells exposed to STS are spatially associated with the mitochondria. We first studied the segregation of the mitochondria-rich and mitochondria-poor compartments derived for each ROI by modulating the threshold value (**Fig. 4-7**). As shown in **Fig. 4-7** for a representative cell, when the threshold is set too high, pixels that are clearly fluorescent are designated as non-fluorescent and the optical signal changes in both the fluorescent (above threshold) and non-fluorescent (below threshold) regions (**Fig. 4-7e - Fig. 4-7f**). As the threshold is decreased, less of the fluorescent pixels are included in the region designated as non-fluorescent, and the decrease in orientedness becomes more pronounced in the fluorescent segment compared with the non-fluorescent one (**Fig. 4-7b - Fig. 4-7c**). For very low thresholds, pixels that are clearly nonfluorescent are designated as fluorescent and the optical signal changes in the fluorescent segment become less pronounced than at higher thresholds (**Fig. 4-7a**). By choosing the threshold as the average fluorescence intensity of the cell ROI (and assigning this derived average a value of unity, i.e. $Th = 1.0$, **Fig. 4-7c**), we found that we could arrive a good signal separation between the background and fluorescent areas within the ROI taken at high resolution. We therefore chose this threshold, $Th = 1$, to derive the fluorescent and non-fluorescent regions in all cells for all time points.

Fig. 4-8 shows the results of studying the fluorescent (**Fig. 4-8a**) and nonfluorescent regions (**Fig. 4-8b**) separately within each cell. In the fluorescent regions, orientedness decreases significantly (**Fig. 4-8a**, bold black time trace with solid squares), especially between 60 and 100 minutes ($p < 0.05$ comparing these two time points), but does not decrease significantly in the non-fluorescent regions (**Fig. 4-8b**, bold black time trace with

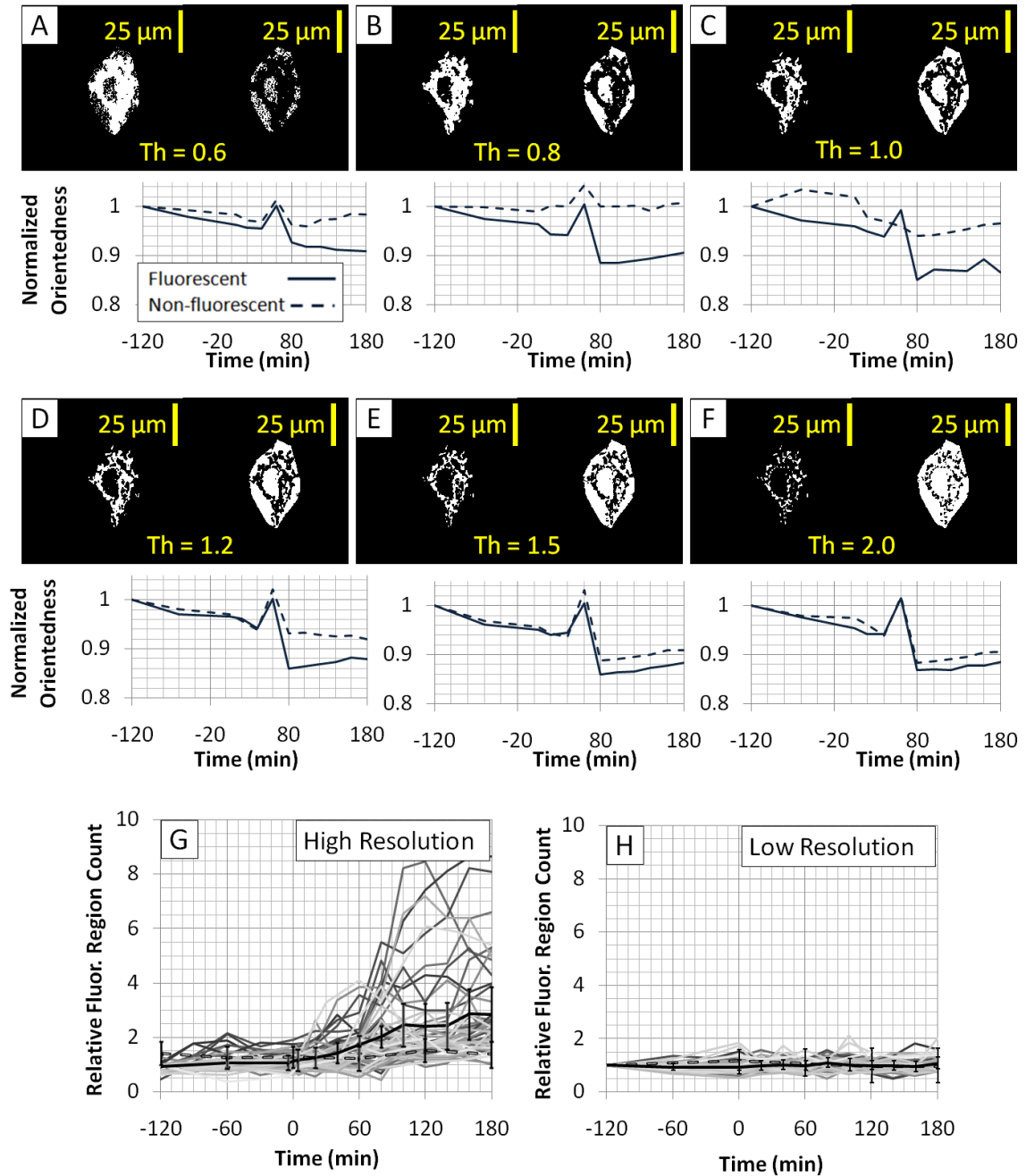


Fig. 4-7. Effect of threshold level on separating dynamics of fluorescent and nonfluorescent regions within cell ROIs at high resolution (objective NA = 1.4, 0.195 $\mu\text{m}/\text{pixel}$). A representative cell from the center of the field of view shown in Fig. 4-5 is illustrated here. A-F show the fluorescent (above threshold, left) and non-fluorescent (below threshold, right) region pairs generated by applying a threshold to the corresponding Gabor-resolved fluorescence image (Fig. 4-3d). The time traces for normalized mean orientedness evaluated within the designated fluorescent mask (above threshold, solid black line) and the non-fluorescent mask (below threshold, dashed line) are shown below the corresponding binary mask images. The threshold level, Th , is given as a fraction of the average fluorescence signal within the cell ROI (e.g. $Th = 2.0$ indicates that twice the average of the intensity of the Gabor-resolved fluorescence images within that ROI was used to generate the region pair).

solid squares). This behavior is different from DMSO control studies (blue traces with open circles in **Fig. 4-8a - Fig. 4-8b**), in which neither the fluorescent nor the nonfluorescent regions show such a decrease in orientedness over this timeframe. Thus the optical scattering changes measured by Gabor filtering are isolated to the mitochondria-rich compartment of BAEC during exposure to STS.

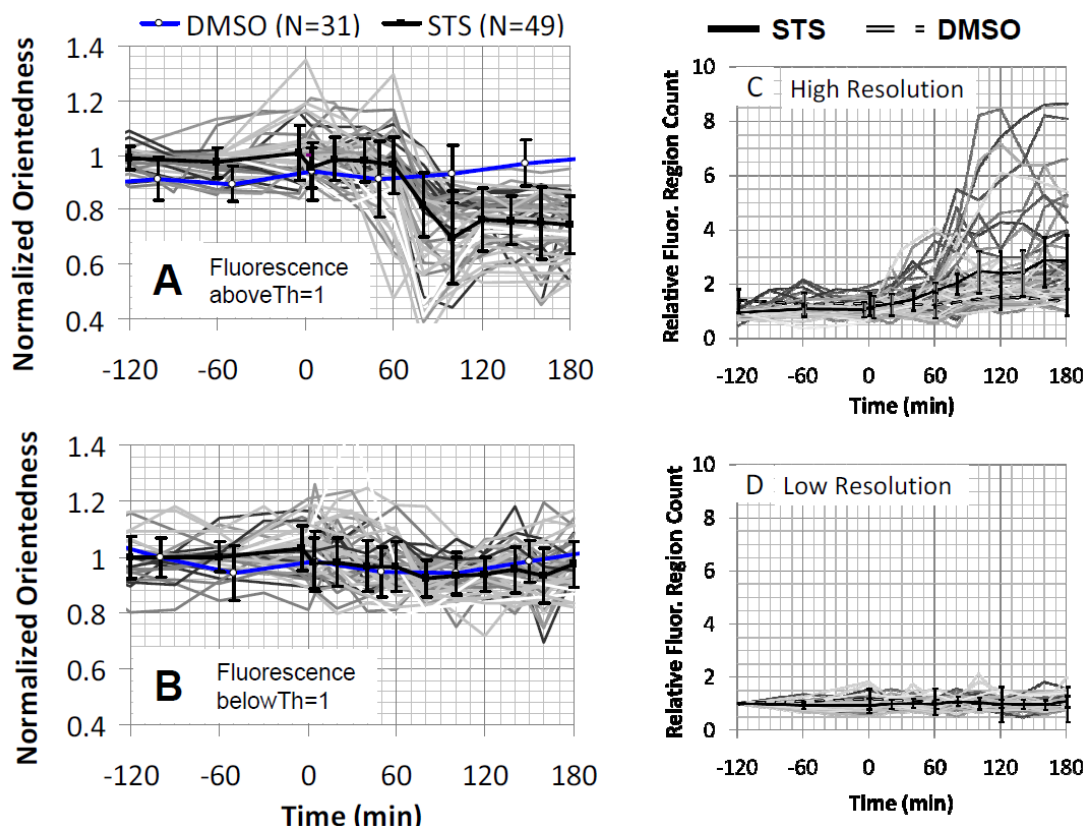


Fig. 4-8. A-B: Time traces plotting orientedness for the bright, above-threshold fluorescent regions (A) and for the dim, below-threshold regions (B) within individual STS-treated cells (gray traces). The average fluorescence intensity in the processed fluorescence image defined the threshold value within each cell and corresponds to Th=1 (see also **Fig. 4-7**). Bold black trace with solid squares represents the mean \pm standard deviation of the gray traces of cells exposed to STS. Blue trace with open circles corresponds to the mean \pm standard deviation for DMSO control (average of all cells). C-D: Normalized number of non-contiguous fluorescent regions counted in the above threshold fluorescent mask generated at high resolution (Panel C, NA=1.4, $0.195\mu\text{m}/\text{pixel}$) and at low resolution (Panel D, NA=0.75, $0.625\mu\text{m}/\text{pixel}$) with Th=1. The rise in the number of fluorescent regions beyond T = 60 min. is statistically significant ($p < 0.05$) comparing average STS response with DMSO control at high resolution (C) but is not statistically significant ($p = 0.72$) at low resolution (D). In C-D, bold black trace represents the mean \pm standard deviation of the gray traces of cells exposed to STS. Dashed trace corresponds to the mean \pm standard deviation for DMSO control (average of all cells).

We also tracked the relative number of non-contiguous regions within the masks generated for Th=1. At high resolution, we found that the number of regions within the

masks increases by about a factor of 2.5 between 0 and 180 minutes after STS exposure, most of which occurs between 60-120 minutes, consistent with mitochondrial fragmentation during this time (**Fig. 4-8c**). This behavior is absent when the control data are processed in this manner, suggesting this behavior is STS-specific. When repeating the segmentation process on the low resolution fluorescence images (**Fig. 4-8d**), the masks fail to recapitulate this response; the number of fluorescent segments does not appreciably increase over time or over control, implying that high resolution is required for the masks to be effective in segmenting the mitochondria well.

ASSESSMENT OF MOVEMENT

To assess movement of the mitochondria between time points as apoptosis and mitochondrial fragmentation proceed, we compared the fluorescent and non-fluorescent masks (using the threshold value $Th=1$) at the beginning and end of the entire time span. We find that ~26% of the pixels within a given cell ROI may move from one segment to the other during fragmentation. This necessitated taking new fluorescent images of the cells and defining the fluorescent and non fluorescent regions above and below threshold at every time point. However, movement may also exist in the 7-8 min time span over which the data set for a single time point is acquired under relatively steady-state conditions, well before or well after fragmentation.

Fig. 4-9 shows the prevalence of movement in a 10 minute time span after STS addition but well before fragmentation occurs. We acquired fluorescence images over 10 minutes at 5 second intervals for the first minute and then every 15 seconds thereafter. We repeated the process of segmenting each cell ROI into designated fluorescent and non-fluorescent segments above and below the ROI's average fluorescence intensity ($Th=1$) and compared

these segments at each time point with the initial segments at $T=0$ in order to quantify movement over the 10 minute time span. As shown in

Fig. 4-9, in the first 15 seconds, only 3% of pixels change between being classified as fluorescent and non-fluorescent. By 1 minute this value rises to 5% and by 10 minutes, 8% of the total number of pixels within the first ROI has changed designation. This effect is most prominent in the periphery of the cell where mitochondrial density is lowest (yellow areas in

Fig. 4-9c). These results suggest that the fluorescent masks remain accurate to within 8% during image acquisition for time points away from the moment of fragmentation under approximately steady-state experimental conditions.

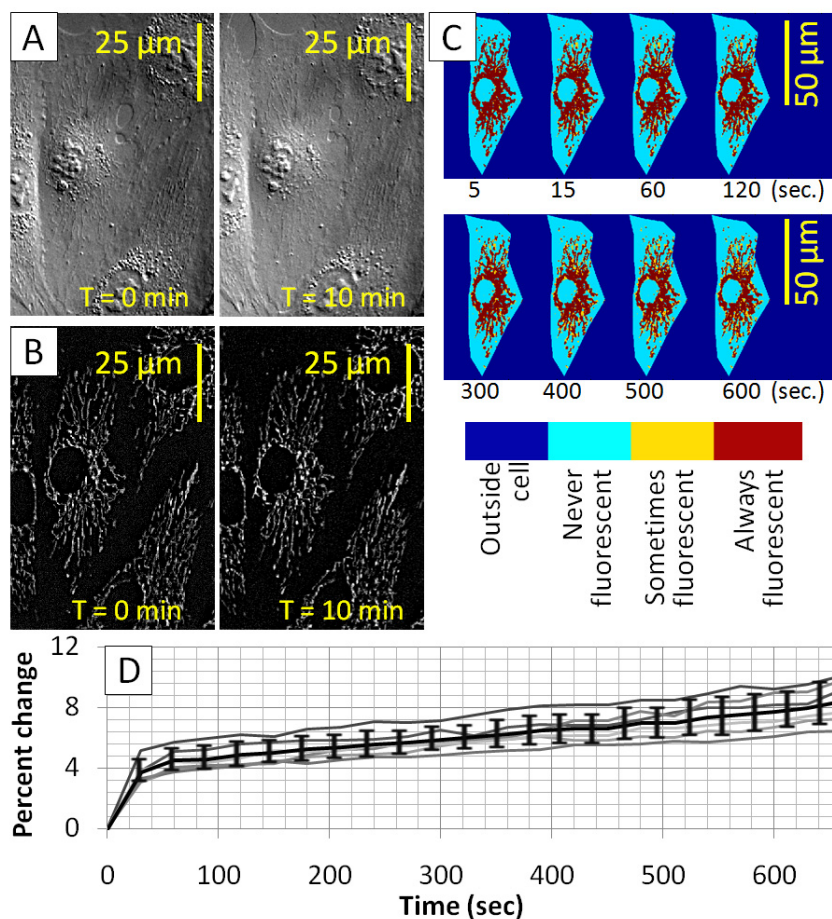


Fig. 4-9. Effect of movement on accuracy of masks. DIC (A) and fluorescence (B) image of BAEC labeled with Mitotracker green under experimental conditions taken immediately after

STS exposure ($T = 0$ min.) and 10 minutes later. C: Color coded segments demonstrating how the segments within the ROI of a representative cell change over time. Each ROI is compared with the initial ROI at $T=0$ in order to quantify movement over a 10 minute time span. D: Time trace plotting the fraction of pixels that change between fluorescent and non-fluorescent regions over time. After an initial jump from zero to 5% by 1 minute, the error increases at a fairly constant rate of .4% per minute. Solid bold black trace represents the mean \pm standard deviation of the gray traces of cells exposed to STS in this experiment.

CONFIRMATION OF APOPTOSIS

To confirm the apoptotic fate of the BAEC treated with STS, we assessed the cleavage and activation of caspase 3 by immunofluorescence (**Fig. 4-10**). A long exposure (> 2 sec.) was used in collecting the fluorescent images. Low intensity background fluorescence is detected within most cells for both treated and control cells. Cells positive for caspase 3 activation are identified as cells with bright fluorescence with intensity at least 50% higher than background levels. After three hours of treatment with STS at room temperature, the

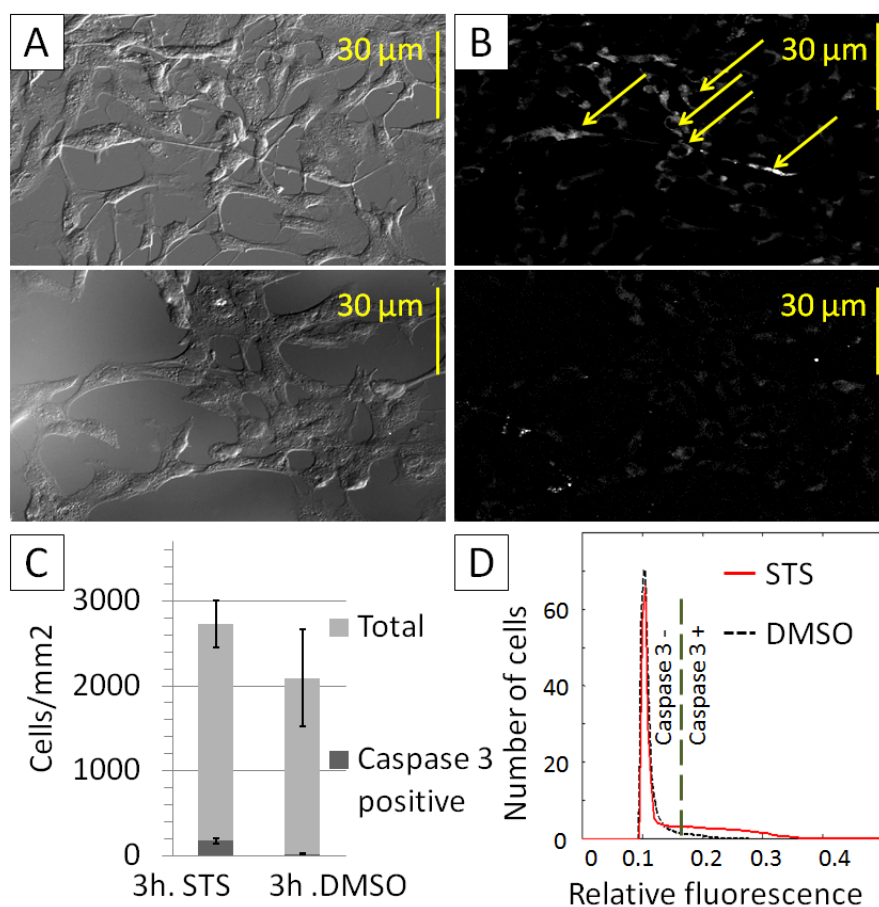


Fig. 4-10. Immunofluorescence of cleaved caspase 3 in BAEC under experimental conditions. Representative DIC (A) and immunofluorescence (B) images of cells treated with STS (top) or DMSO

(bottom) for 3 hours. C: Number of caspase 3 positive cells (dark gray) as a fraction of the total number of cells tested (light gray) for STS- and DMSO-treated cells. The ordinate cells/mm² is calculated by manually counting cells and normalizing to the area of the field of view measured with the aid of a stage micrometer. While small, the fraction of cleaved caspase 3 positive cells is significantly greater ($p < 0.01$) in the cells treated with STS than cells treated with DMSO. D: Relative fluorescence intensity distributions for the STS- and DMSO-treated cells. Cells with intensity greater than 50% the background intensity (0.11) were taken as positive for caspase 3 activation.

results show caspase 3 activation in 7.3% of the STS treated cells compared with 0.5% in the cells treated with only DMSO (control). This difference is significant ($p < 0.01$) and provides evidence of apoptosis initiation in the STS treated cells.

4.1.3: DISCUSSION

Using optical imaging with Gabor-like filtering, we demonstrate sensitivity to changes in light scattering from BAEC cells undergoing apoptosis in response to STS treatment. We observed a significant drop in the degree of orientation (“orientedness” parameter) of subcellular structures 60-100 minutes after apoptosis induction by STS. These scattering changes, which result from alterations in subcellular structure, could be detected and monitored at a low resolution at which subcellular structural dynamics could not be directly visualized by fluorescence or DIC (**Fig. 4-4**). These results were reproduced at high image resolution where they occurred concurrently with mitochondrial fragmentation observed by fluorescence (**Fig. 4-5-Fig. 4-6**). At high resolution, the optical light scatter changes could be isolated to the subcellular compartments dominated by fluorescent mitochondria, while optical scatter changes remained negligible in regions with dim fluorescence signal dominated by non-fluorescent background (non-mitochondria) (**Fig. 4-8a - Fig. 4-8b**). Thus, our results strongly suggest that the drop in orientedness between 60-100 minutes is due to mitochondrial fragmentation, a process in which relatively large, filamentous structures (contributing to high orientedness) become smaller and rounder (yielding low orientedness).

Validation of the optical scatter signatures is dependent on the ability to label the mitochondria and use this labeling to segment the subcellular mitochondria-rich regions from the remainder of the cell based on a fluorescence intensity threshold as described in **Fig. 4-7**. Mitochondrial movement is an inherent limitation to the ability of this method. However we find that the two fluorescent segments above and below threshold do not shift by more than 26% over the course of fragmentation and change only by 8% during a 10 minute time span taken under quasi steady-state conditions. Thus, while mitochondria move during fragmentation, the fluorescent pixels associated with them at a given measurement timepoint remain sufficiently spatially confined within the resolution of the designated fluorescent segment such that we still can separate the background from the dynamic signal associated with mitochondria reasonably well. Our data does not completely exclude the presence of mitochondrial pixels from the background segments below threshold or the presence of some background pixels in the fluorescent segments above threshold. However our data demonstrate that the optical scatter dynamics are significantly reduced, if not completely absent, in cell segments dominated by nonfluorescent organelles (“background”). This suggests that any background contribution to the dynamic scattering signal is likely to be negligible within the brightly labeled regions dominated by the presence of mitochondria. Based on previous work demonstrating the larger contribution of mitochondria to the light scatter signal relative to other organelles (62; 88; 94), we may also assume that other organelles present in close association with the mitochondria (e.g. the endoplasmic reticulum) do not contribute appreciably to the optical scatter dynamic observed within the mitochondria-rich fluorescent regions. Thus the measured optical scatter dynamics are largely associated with mitochondria in the designated fluorescent regions above threshold. Low resolution and whole-cell detection of the decrease in orientedness (**Fig. 4-4, Fig. 4-6**)

was therefore also possible because of this null background contribution to the optical dynamic.

In addition, several findings support the hypothesis that mitochondrial alterations are the source of the measured optical scatter changes. Modulating the threshold which defines the fluorescent and non-fluorescent segments, results in modulating the optical scatter changes in the two compartments, suggesting that the optical scatter changes are spatially correlated with the fluorescence signal (**Fig. 4-7**). By considering the changes in orientedness at steady state time points well before and well after fragmentation, when the designated fluorescent and non-fluorescent segments should be accurate within 8%, we still find that orientedness is significantly changed only in the designated fluorescent regions and remains absent from the non-fluorescent ones (**Fig. 4-8**). Finally, the decrease in orientedness measured at the moment of fragmentation (between $T=60$ and $T=100$) in the designated fluorescent regions was not accompanied by an increase in orientedness in the designated non-fluorescent regions (**Fig. 4-8**). Thus, the measured decrease in orientedness could not be purely attributed to movement of oriented mitochondria from one segment to the other. Instead, mitochondrial fragmentation accompanied by movement of the mitochondria, would give rise to a decrease in orientedness in the fluorescent regions. At the same time, possible movement of the fragmented mitochondria, which have low orientedness on the order of background (more blue in **Fig. 4-4** and **Fig. 4-6**), to the non-fluorescent regions would keep the optical signal constant in these background regions. Still, current work focused on increasing light throughput and automation of the hardware, is under way to obtain faster optical scatter image acquisition, and thus minimize the effect of movement on the accuracy of multi-image registration, and allow better time resolution of subcellular dynamics.

As expected, the fragmentation of mitochondria (**Fig. 4-5**) and evidence of caspase 3 activation observed in the STS treated BAEC (**Fig. 4-10**) reproduces previous evidence of mitochondrial fission in apoptotic cells treated with STS (30). In addition, alterations in light scattering concurrent with alteration in mitochondrial function during apoptosis have been reported (65; 72; 95). The present results extend these previous studies by showing that orientation-dependent changes in light scattering within the first three hours of apoptosis are spatially associated with mitochondria undergoing fragmentation, and can be directly quantified with an optical scatter imaging method based on Fourier filtering with Gabor-like filters.

4.2: HIGH TIME-RESOLUTION STUDY OF APOPTOSIS

The mitochondrial fragmentation study described in Chapter 4 Section 4.1.2 was repeated with the automated LCD-based system with the intent of using more filters applied at more frequent time intervals to gain a more complete understanding of the dynamics previously observed using the DMD and manual acquisition. This study aims to repeat the optical measurements of Chapter 4 Section 4.1.2, and to reveal more rapid dynamics that may be present but could not be temporally resolved in the previous study. The Gabor filter-based acquisition on the LCD-based system is automated and allows for acquiring many more filtered images much more rapidly than otherwise possible. The added filters and time points can yield more information by interrogating more areas of the Fourier plane than previously possible and can aid in discovering additional optical scatter behaviors measured by the system.

4.2.1: CELL PREPARATION AND OPTICAL SETUP

Using the same experimental model consisting of endothelial cells treated with the apoptosis inducer, staurosporine (STS), this method is applied with the LCD system to analyze mitochondrial and nuclear dynamics during the first three hours of apoptosis. Using the setup described in Chapter 2, Section 2.3.1, this study utilizes a filter bank consisting of five filter periods ($S = 0.6 \mu\text{m}$, $S = 0.9 \mu\text{m}$, $S = 1.2 \mu\text{m}$, $S = 1.8 \mu\text{m}$, and $S = 3.6 \mu\text{m}$) over $0^\circ \leq \varphi < 360^\circ$ in 15° increments. This yields a filterbank of 120 filters that probes the entire Fourier plane of scattered light.

Bovine aortic endothelial cells (BAEC) were cultured and plated on glass coverslips and labeled with Mitotracker Green (Invitrogen) as previously described (Section 5.2). Apoptosis was induced in the same manner as in Section 5.2 by replacing the existing medium with medium containing $1 \mu\text{M}$ of the apoptosis inducer staurosporine (STS), obtained from a 4mM STS stock in dimethylsulfoxide (DMSO). Control studies consisted of loading the viewing medium with DMSO only in the same volume in place of the STS solution as in Section 5.2.

4.2.2: DATA ACQUISITION AND ANALYSIS

Optical filtering was applied for three hours after STS addition at $T = 0$. For each filter, background images of a glass coverslip with no sample were also collected and subtracted during post-processing.

At each pixel we measured the total filter response summed over all angles at each filter period. For each filter period, we also measured the degree of particle orientation, or “orientedness” at each pixel. Orientedness was calculated as the ratio of maximum to average filter response as a function of filter orientation φ . For the data collected with φ varying over 360° , orientedness was calculated by taking the average of the centrally-

symmetrical maximums over the average filter response as a function of φ . At each timepoint, each cell studied was segmented manually into a region of interest (ROI) and data analysis was confined to these ROIs.

4.2.3: RESULTS AND DISCUSSION

Fig. 4-11 shows unfiltered dark field images of representative cells at $T = 0$ and 180 min after STS treatment. The images in the lower panels show optically processed images of the same cells. In each of these images, the color brightness encodes the total response (summed over all orientation angles) of the Gabor filters at a given period, S . The color hue encodes the degree of orientation at each Gabor period, taken as the ratio of maximum over average response as a function of orientation angle φ . The images show a decrease in orientedness for $S = 0.9\text{-}1.2\ \mu\text{m}$.

In **Fig. 4-12** (middle panels) we show quiver plots which encode the local orientation angles of the subcellular structures with responses at $S = 0.9\ \mu\text{m}$. The polar plots (**Fig. 4-12** bottom panels) depict sample Gabor filter responses measured in the cytoplasm and the nucleus of the cells. As can be observed in these examples, the filter responses in the cytoplasm show a preferred angle of orientation, while the responses in the nucleus are more isotropic. The polar plots suggest that in the cytoplasm, the signal from features corresponding to Gabor filter periods of $S = 0.6\text{-}1.2\ \mu\text{m}$ increases after three hours of apoptosis. At the same time the subcellular particles with responses at $S = 0.9\ \mu\text{m}$ become significantly less oriented after the first three hours of apoptosis as also depicted in the quiver plots. On the other hand the signal in the nucleus remains more isotropically

distributed and shows stronger responses around values of $S \leq 1.2$. In **Fig. 4-13** the loss of orientedness for $S = 0.9 \mu\text{m}$ is plotted as a function of time for the cells in the field of view.

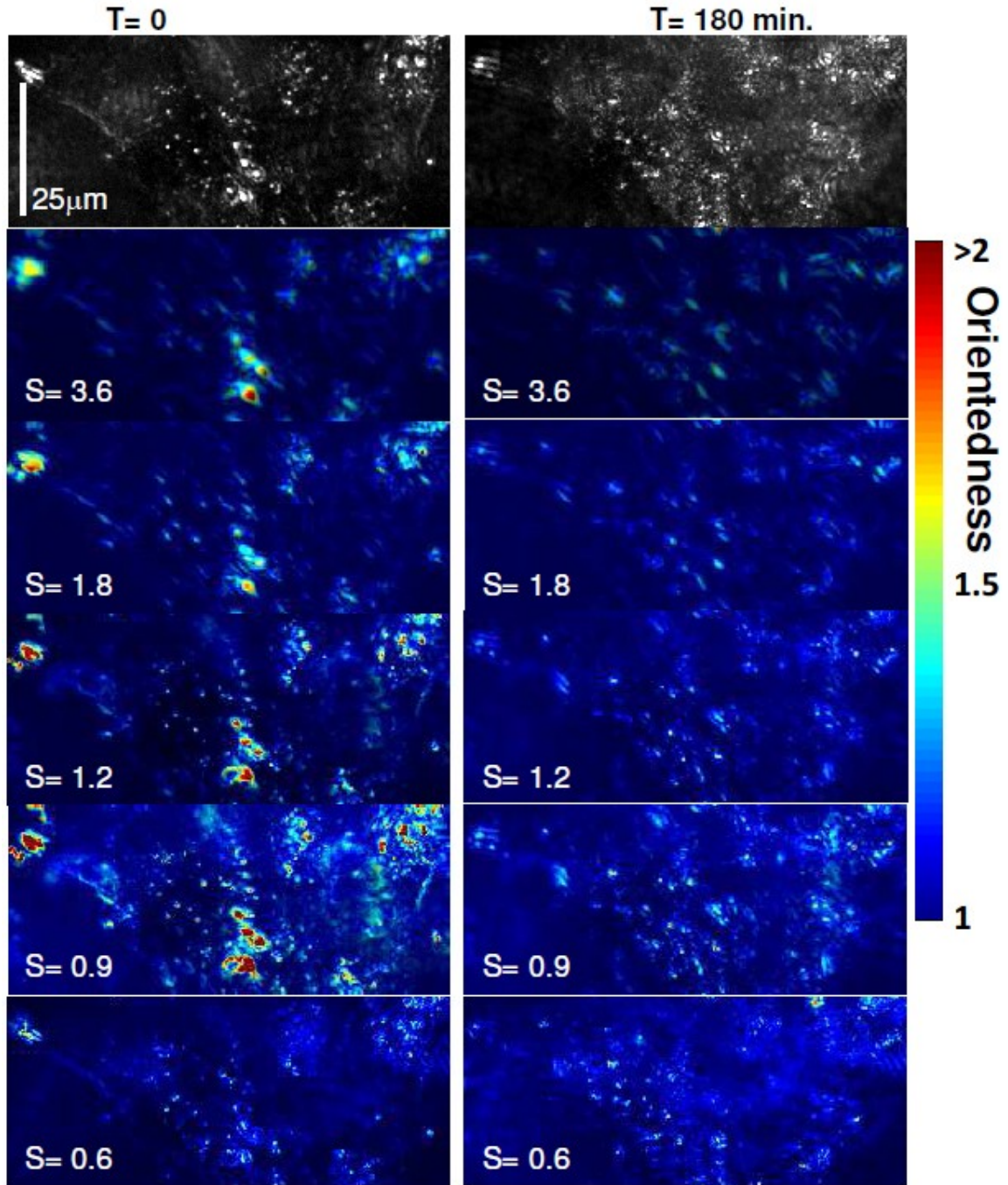


Fig. 4-11. Dark-field (top panels) and optically processed images of a representative field of view just before and 180 min. after STS treatment. For a given filter period S (in μm), orientedness (color scale) is taken as the ratio of maximum over average filter response as a function of filter orientation φ . The color brightness gives the total response at the filter period, S , summed over all angles.

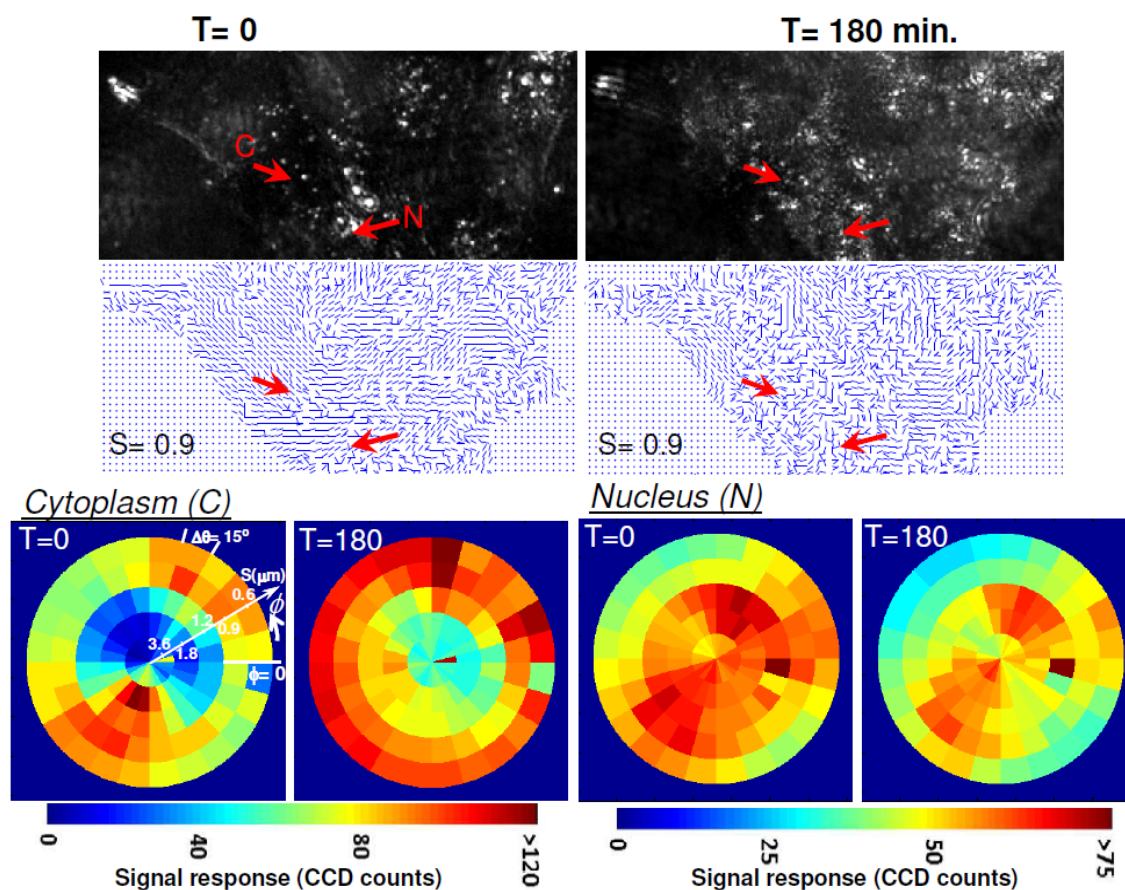


Fig. 4-12. Dark-field (top panels) and quiver plots (middle panels) showing the orientation angle of subcellular structures with filter responses at $S = 0.9 \mu\text{m}$. The polar plots show representative data collected with the optical system. Filtered signal responses are shown as a function of filter period S and filter orientation φ for two 4×4 pixel regions (arrows) located in the cytoplasm (C) and nucleus (N) just before ($T = 0$), and 180 min. after STS treatment.

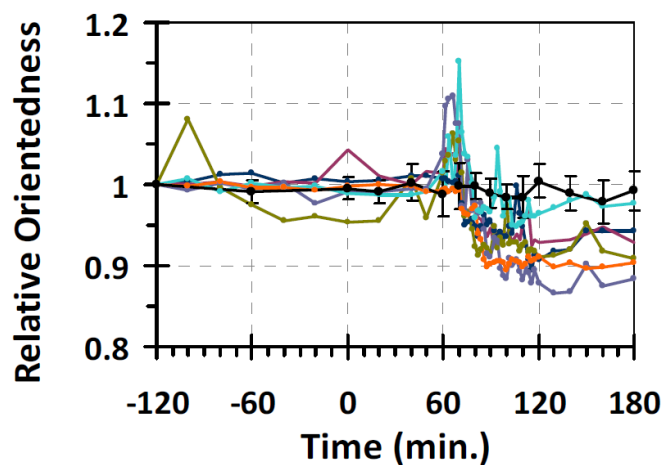


Fig. 4-13. Average orientedness per cell plotted as a function of time for filter responses at $S = 0.9 \mu\text{m}$. The data were normalized to the value at $T = -120 \text{ min}$. STS or DMSO was administered at $T = 0$. Individual traces are shown for the STS-treated cells in the field of view tested in

Fig. 4-11 and **Fig. 4-12** ($N = 6$). The black line with solid black circles is the mean orientedness \pm 95% confidence interval of cells treated with DMSO ($N = 7$).

We had found that the Gabor filter responses are maximized when the diameter of the scatterers correspond to approximately half the Gabor filter period (84). Thus, particles with a high signal at $S = 0.9 \mu\text{m}$ are approximately $0.45 \mu\text{m}$ in diameter. This size range corresponds to the reported width of mitochondria between $0.3 \mu\text{m}$ and $0.6 \mu\text{m}$ (96) and is therefore consistent with the strong measured response of mitochondria at this spatial frequency. The orientedness dynamics and mitochondrial fragmentation observed in this study corroborate previous reports of mitochondrial fragmentation in apoptotic cells (24; 25; 34). Interestingly our results also show that orientedness increases immediately before it starts decreasing upon mitochondrial fragmentation. This dynamic could reflect the reported elongation of mitochondria prior to fragmentation (31).

In summary, the light scattering data measured in this study report on mitochondrial fragmentation early during apoptosis. Further work will be aimed at investigating whether these light scattering changes are correlated with a final commitment to cell death. Light scattering changes resulting from subcellular dynamics later in the apoptotic cascade also remain to be determined by use of the methods presented here. While we have used two-dimensional Gabor filters in this study, other two-dimensional Fourier filtering approaches may also be considered.

4.3. DISCUSSION:

In summary, the data presented in this chapter provide strong evidence that mitochondrial fission can be monitored in situ within living cells through the use of light scattering signatures that depend on the degree of particle orientation. This method would have significant advantages in applications where sample labeling is cumbersome or where

fluorescence labels may interfere with biological function. The ability to monitor the process at low image resolution at the whole cell level would also permit a higher cell analysis throughput. This method could be utilized to detect fragmentation of mitochondria during apoptosis as shown here or in other systems. In this context, our results indicate that this technique may provide a tool that can be combined with molecular and biochemical methods to help facilitate elucidation of the structure-function relationship of mitochondria in apoptosis. In particular, the method can be used to investigate the presence of mitochondrial fission in response to activation (e.g. Bid activation) or knock out (e.g. Bax/Bak knock out) of Bcl-2 family proteins. Thus, aided by the measurement method presented here, future studies of mitochondrial fission in response to Bid activation, Bax/Bak knock out, or Bcl-x_L over-expression, could ultimately lead to important clues regarding the apoptotic function of mitochondrial dynamics.

The work presented in the following chapter investigates whether this response is specific to apoptosis by measuring the response of both bax/bak expressing and bax/bak null cells in an immortalized baby mouse kidney cell line. The results of Chapter 5 show that there is a response in the wild-type immortalized bax/bak expressing cells that is reminiscent of the response seen in the BAEC. They also show that this response is absent in the bax/bak knockouts. The side-by-side comparison of bax/bak expressing cells and bax/bak knockouts sheds light on whether the optical detection of mitochondrial fragmentation yielded by this study can be used as a marker for apoptosis and is therefore an integral component to this thesis.

CHAPTER 5 :

USING OPTICAL GABOR FILTERS TO DETECT DIFFERENTIAL RESPONSE TO APOPTOSIS IN NATIVE IBMK AND IBMK BAX/BAK KNOCKOUTS

- This chapter includes work published in (80), Pasternack RM, Qian Z, Zheng J-Y, Metaxas DN, White E, Boustany NN. “Measurement of subcellular texture by optical Gabor-like filtering with a digital micromirror device.” Opt. Lett. 33, 2209-2211 (2008)

5.1: APPLYING OPTICAL GABOR FILTERS TO MEASURE TEXTURE AND ORIENTEDNESS IN NATIVE IBMK AND IBMK BAX/BAK KNOCKOUTS

The optical Gabor filter approach shows great potential in its sensitivity and versatility in measuring morphological parameters under ideal conditions of known sample morphology and high SNR. With the completion of characterizing the setup and Gabor filter performance, the next step was to conduct a measurement under the more challenging condition of monitoring subcellular morphology in living samples. The next series of experiments works with a cell line consisting of two variants of immortalized baby mouse kidney (iBMK) cells. One of the variants is apoptosis-resistant, in which the pro-apoptotic genes encoding the proteins bax and bak are genetically knocked out (which herein will be referred to as iBMK-D3). In the other apoptosis-competent variant, the bax/bak-encoding genes are preserved. This cell model is described in detail in (17) The cells were generously provided by Dr. Eileen White at CINJ.

As detailed in the introduction, apoptosis execution by the BCL-2-family pro-apoptotic proteins Bax and Bak converges on the mitochondria. Bax and Bak promote the eventual release of cytochrome c and collateral substances by increasing mitochondrial permeability, and their localization to the mitochondria is associated with significant structural changes in which the mitochondria undergo fission (9). Additionally, mitochondria

are very highly scattering and nearly ubiquitous in the cytoplasm, and most of the scatter generated by the cytoplasm is derived from the mitochondria (88). Finally, recent data also shows that mitochondria in cells lacking Bax and Bak are shorter and have lower fusion rates compared with cells expressing Bax and Bak (9).

This cell model therefore constitutes an ideal test-bed for assessing the optical Gabor filtering approach in measuring morphological characteristics in apoptosis and in turn for developing the Gabor filtering approach into an apoptosis assay. The cells provide a means to study apoptosis and furnish a genetic control for differences observed between cells that undergo apoptosis (bax/bak present) and cells that do not (bax/bak absent). The use of these cells will therefore greatly facilitate the study of dynamic response to apoptosis. Any differences observed between the two cell variants, all other things being equal, necessarily implicates the effect of bax/bak on cell morphology. This section discusses measurements on living iBMK-W2 and iBMK-D3 cells without staining by using the filter scheme tested on the marine diatom sample discussed above, and, in the case where the automated LCD-based setup is used, Principal Component Analysis (PCA) of the scattering response at individual pixels to arrive at a similar metric for orientedness.

As a proof of principle, this chapter shows that by filtering with a Gabor filterbank sensitive to object orientedness, one can discern differences in overall orientedness between each cell type under identical conditions. Because these differences necessarily arise from the presence or absence of bax/bak, this proof of principle determines whether or not the approach can be sensitive to biological differences in morphology, and therefore is a significant milestone of the development of the optical Gabor-filtering process.

This chapter then shows how the rudimentary "orientedness" parameter could be used to study differential response to apoptosis induction in the two cell variants by

conducting time-lapse studies of the cells under apoptotic and control conditions. Finally, the iBMK cell model is used to study differential response to apoptotic and control conditions with automated acquisition and longer (12 h) dynamic studies with more filters used in the applied filterbank and the PCA analysis.

5.1.1: METHODS

OPTICAL SETUP

The DMD (*TI 0.7 XGA DMD 1100*) was placed in the conjugate Fourier plane of an inverted microscope (Axiovert 200M, Zeiss, Göttingen Germany) fitted with a 20x objective with numerical aperture (NA) = 0.75. Light from a ~5 mW Helium-Neon laser ($\lambda_0 = 632.8$ nm) was passed through a spinning diffuser and coupled into a multimode fiber whose output was collimated and launched into the microscope's condenser aligned in central Köhler illumination (NA < 0.05) (**Fig. 2-2**). Image acquisition consisted of collecting on the CCD a stack of spatially filtered images using a spatial filter bank generated by the DMD (exposure time = 2000ms). Using the diffraction pattern of a graticule with line spacing $b = 10\mu\text{m}$, we converted mirror positions on the DMD to spatial frequency in cycles/ μm and calibrated as described in section 2.4. The calibration gave 12.74 mirrors per diffraction order, or 0.00785 cycles/ μm /mirror. The maximum aperture (NA = 0.75) corresponds to $\text{NA}/\lambda_0 = 1.185$ cycles/ μm or a radius of 151 DMD mirrors. The microscope aperture was not projected on the full width of the DMD to avoid image aberrations originating from the edges of the DMD as discussed in section 2.2. All images discussed in this section are taken at a magnification of 0.275 μm /pixel .

In the present analysis, $S = 0.9 \mu\text{m}$, and $0^\circ \leq \varphi < 180^\circ$ in 20° increments. S corresponds to 1.11 cycles/ μm , or an object size of approximately 450 nm diameter, a good

first estimate for an average width of mitochondria and well within their measured size range ((62; 96) with $\sigma_s = S/2$. The set of nine Gabor-filtered images of the cells were processed pixel-by-pixel for object orientation θ and orientedness O as described in section 3.5. The images shown are encoded as in **Fig. 3-12**, where Color scale indicates degree of orientation (aspect ratio) while brightness encodes significance of the total Gabor filter response.

CELL CULTURE

iBMK-W2 and iBMK-D3 were cultured separately in high glucose Dulbecco's modified Eagle's medium (DMEM, Invitrogen, CA) supplemented with 10% fetal bovine serum (FBS, Invitrogen) and 100 U/ml penicillin, and -100 g/ml streptomycin (Invitrogen). The cells were kept in culture at 38°C in a 8.5% CO₂ in humidified air. One day prior to experiments, the cells were passaged and plated at 40,000 cells/cm² on No. 1 coverslips (Fisher). On the day of the experiment, these coverslips were removed from incubation with the attached live cells, rinsed with Leibowitz L-15 medium with 10% FBS ("viewing medium"), and attached to a steel plate with vacuum grease (see Chapter 4, Section 4.1.1). For 12 hour time lapse, the steel plate is exchanged for a closed chamber without flow channels with total chamber volume 1mL and are otherwise loaded and mounted as in Chapter 4, Section 4.1.1.

5.1.2 Results

Fig. 5-1 and **Fig. 5-2** illustrate the result of the aspect ratio and orientation analysis. **Fig. 5-1** shows that the orientedness information (**Fig. 5-1c** and **Fig. 5-1g**) can be spatially confined and can be registered with DIC (**Fig. 5-1a** and **Fig. 5-1e**) and DF (**Fig. 5-1b** and **Fig. 5-1f**). The overall signal level (encoded by pixel intensity) within the cells shows brighter regions associated with the cytoplasm while the nucleus is comparatively dim,

indicating that the objects in these areas respond favorably to the filter period applied and that this signal could be mitochondrial in origin. Panels (d) and (h) of **Fig. 5-1** shows the effect of a 4x4 pixel block processing on the filtered images before processing to simulate a 4x demagnification. In this case, resolution is lowered, but the distribution of signal and orientedness (indicated by pixel hue) is preserved. Pixel histograms (**Fig. 5-2**) of all cells tested in each variant show that there are more round features in the D3 cells compared with the W2 cells; the mean aspect ratio per cell was 1.58 for W2, 1.38 for D3 ($p \leq 0.04$ by student t test). This difference is preserved even with a 4x demagnification (**Fig. 5-1d**, **Fig. 5-1h**). The histograms in **Fig. 5-2** could be consistent with these variations to the extent that shorter mitochondria in our D3 cells will result in a larger number of particles having a lower mean aspect ratio.

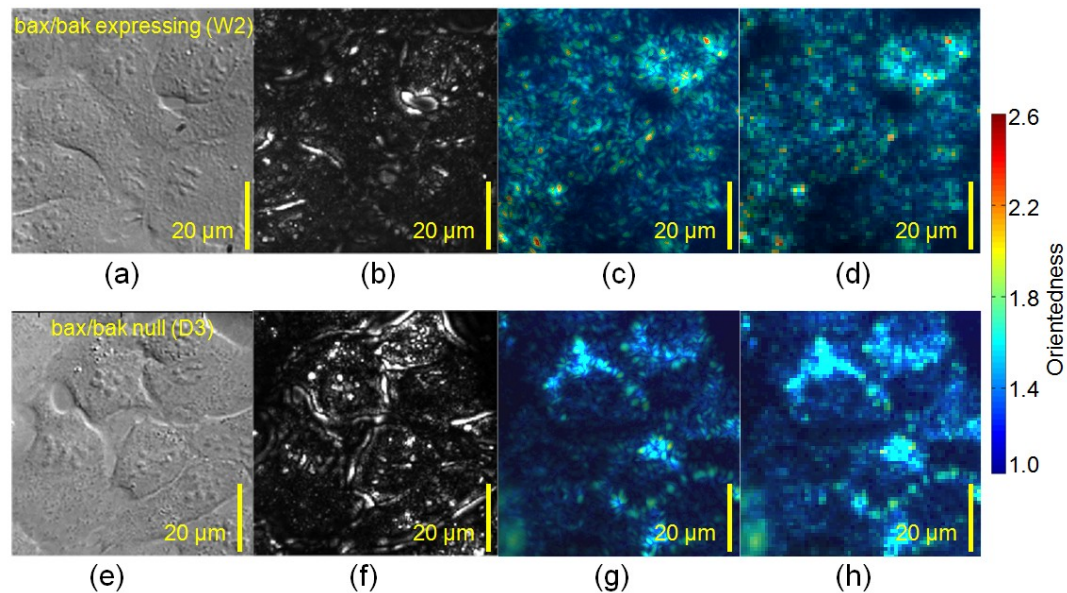


Fig. 5-1. W2 (bax/bak expressing) and D3 (bax/bak null) cells images. (a), (e): Differential interference contrast, (b), (f): Dark field (DF). Little difference can be discerned between the two cell types using these modalities. (c), (g): Object orientation as in **Fig. 3-12**. More highly oriented objects (red areas) are present in the W2 compared with the D3 cell. (d), (h) & F: W2 and D3 cell whose filtered images were block-processed to simulate a 4x demagnification before orientation analysis.

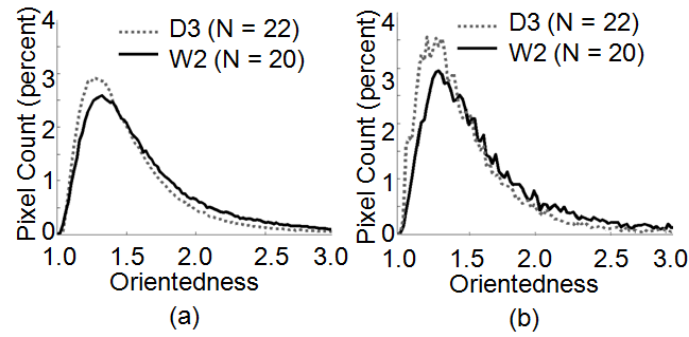


Fig. 5-2. Pixel histogram of all W2 and D3 aspect ratios. A: Histogram for subcellular orientedness without block processing. W2 cells have a higher orientedness distribution ($p < 0.04$) than D3 cells. B: With 4x4 pixel block processing. W2 cells' higher orientedness distribution remains significant ($p < 0.05$).

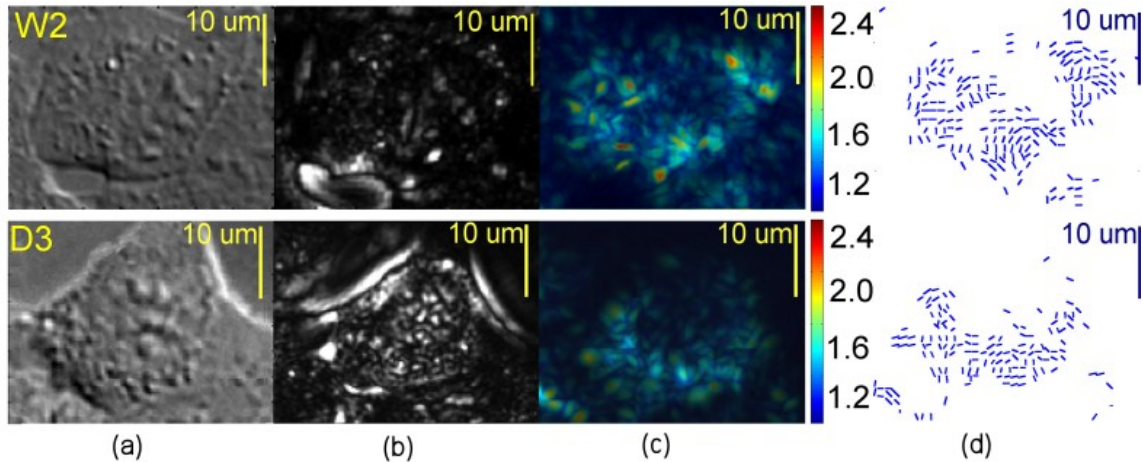


Fig. 5-3. Illustration of orientation measurement from W2 and D3 images. (a) Differential interference contrast. (b) Dark-field. (c) Object orientation as in **Fig. 3-12**. (d) Orientation of objects with response intensity 15% of maximum. Line segment indicates the corresponding structure's long axis.

5.1.3 DISCUSSION

This series of experiments with the iBMK cells is successful at discriminating between the iBMK-W2 and iBMK-D3 cell types. These results establish the feasibility and potential for the optical Gabor filtering technique to make further measurements of subcellular morphology in the apoptosis setting. Given the choice of the filtering parameters used in the results of **Fig. 5-1** and **Fig. 5-3**, the Gabor filter responses should have been confined to object areas on the order of $0.9 \times 0.9 \mu\text{m}^2$. However, by positioning the Gabor filter near the NA passed by the microscope, the Gaussian envelope of our filters was

effectively truncated on the side facing the NA in the Fourier plane. Objects such as mitochondria with signal at high frequencies require analysis near the edge of the NA in many optical settings, and in such situations, this caveat may be unavoidable, but does not fundamentally compromise the ability of the filtering technique to detect object orientation as indicated in the diatom and cell data sets. Eliminating the filter truncation in the Fourier plane by shifting S to $1\mu\text{m}$ and halving the standard deviation of the Gaussian in the frequency plane, resulted in similar differences between the aspect ratio histograms of the W2 and D3 cells, but the sensitivity tradeoff manifests as lower resolution orientation data images in the image plane. This tradeoff is still a limitation to the technique, as histogram differences became less pronounced once the frequency confinement of the filter was further decreased to correspond to an expanded object area of $\sim 3 \times 3\mu\text{m}^2$. The degree of particle orientation is thus decreasingly detectable as the subcellular regions being probed begin to include several particles with different orientations and is averaged out.

It is reiterated that analog processing confers the advantage over digital post-processing that frequency resolution is entirely decoupled from image quality, and depends only on the quality of the design and implementation of the optical filter.

Block processing the initial Gabor filtered images such that every adjacent 4 by 4 pixel region is averaged into one pixel before orientation processing, effectively demagnifies the filtered images from 512×512 to 128×128 pixels, or approximately $1\mu\text{m}^2/\text{pixel}$ (**Fig. 5-1**). Although the pixels in the resulting images are large, they still demonstrate orientation detection substantially similar to that of the higher magnification with aspect ratio mean = 1.54 for W2, and 1.35 for D3 ($p < 0.05$). Because the spatial filtering occurs before undersampling, one can undersample the image plane considerably while still maintaining sensitivity to objects that would otherwise reside well beyond the limit of digital resolution.

Because Fourier plane resolution is no longer tied to image resolution, it is therefore possible to detect oriented sub-micron particles in a larger field, and potentially analyze cells with very high throughput.

5.2 APPLYING GABOR FILTERBANKS TO DETECT DIFFERENTIAL EXECUTION OF APOPTOSIS IN NATIVE IBMK AND BAX/BAK IBMK KNOCKOUTS

With the DMD-based system, it was practical to acquire a handful of filtered images per time point. Beyond this, the constraints of exposure time and manual acquisition prohibit adequate time resolution. With the automated LCD-based system, however, much larger Gabor filterbanks can be acquired quickly and automatically. This opens the door to time-lapse study with many Gabor filters, and this study takes full advantage of this capability.

The operative advantage of this method lies in its potential to monitor the evolution of subcellular processes noninvasively. As described in Chapter 1, apoptosis is a process in which significant morphological events occur in a well-orchestrated and highly conserved sequence. Simultaneously, major difficulties arise when probing dynamic processes with methods that require cell fixation or homogenates, often resulting in the requirement to interrupt or inactivate the process (Chapter 1). The Gabor method therefore has the potential to complement the sensitive but invasive techniques currently used by filling the role of a complementary method whose response can then be correlated with other techniques. (One way this can be accomplished is demonstrated in the previous chapter). In this study, the optical Gabor filtering technique is applied to the iBMK W2/D3 cell model in the apoptosis setting in order to optically distinguish apoptosis-specific dynamics.

5.2.1 METHODS

CELL CULTURE & OPTICAL SETUP

iBMK cells are cultured closely following the methods described in Section 4.3.1.2. and imaged using the optical system described in Chapter 2, Section 2.3.1. Cells are grown to ~90% confluence on No. 1 coverslips prior to imaging. For mounting the cells, the steel plate is exchanged for a sealed microfluidic chamber of similar design. Coverslips are attached and sealed to the chamber as described in 4.3.1.2. Immediately upon completing the cell plating, the cells are imaged as described and maintained at 37-38 °C with a heated stage. Cells were induced to undergo apoptosis by replacing the medium of the sample with viewing medium (Chapter 4, Section 4.3.1.2) with added staurosporine (0.4 μ M or 0.8 μ M final concentration diluted from 4mM in DMSO) and time lapsed with the Gabor filterbanks. Cells in viewing medium with the same volume of DMSO are studied as control.

MONITORING MITOCHONDRIAL POTENTIAL

In order to track changes in mitochondrial potential in parallel with the optical study, separate iBMK are also grown on No. 1 coverslips and labeled with JC-1 (Invitrogen) mitochondrial potential sensitive dye. JC-1 forms red-fluorescing aggregates associated with mitochondria with high membrane potential while the green fluorescing-monomers associate with areas of low potential. JC-1 is applied to the cells for 45 min (38 °C, 8.5% CO₂) at 1.0 μ g/mL prepared from stock solution of 5 mg/mL JC-1 in sterile deionized water in growth medium (growth medium described in Section 4.3.1.2.). The same procedure is followed for W2 and D3 cells. Both live cell time lapse imaging and fixed cell imaging are done for this study.

After incubation with JC-1, cells are rinsed with fresh growth medium and then introduced into viewing medium (STS or control). Cells to be imaged alive are then viewed.

Cells to be fixed are introduced into to experimental conditions (STS or control) and incubated at 37°C for 0 (brief transfer to account for effect of switching medium) or 4 hours but are not imaged during this time. After the desired amount of time has elapsed, cells are then rinsed with PBS and fixed with 2% paraformaldehyde in PBS at room temperature for 10 minutes. The fixed cells are then mounted to microscope specimen slides and sealed with VaLaP. Green fluorescence (non-aggregated JC-1) was acquired with a FITC filter cube (filter No. 10; Carl Zeiss, Gottingen, Germany) with 450-490 nm excitation bandpass, and emission collected through a 510 nm dichroic mirror followed by a 515- 565 nm bandpass filter. Red fluorescence (JC-1 aggregates) was detected with a standard rhodamine filter cube (filter No. 20; Carl Zeiss): with 546-612 nm excitation bandpass and emission collected through a 560 nm dichroic mirror followed by a 575–640 nm bandpass filter.

OPTICAL IMAGING AND FOURIER FILTERING

Gabor filtering is implemented on the LC-R 2500 LCD as described in Chapter 2, Section 2.3.2. An extensive filter bank is used, consisting of Gabor filters with orientations $\varphi = 0^\circ$ to $\varphi = 180^\circ$ in 15° increments and $S = 3.6 \mu\text{m}$, $S = 1.8 \mu\text{m}$, $S = 1.2 \mu\text{m}$, $S = 0.9 \mu\text{m}$ and $S = 0.6 \mu\text{m}$ for a total of 120 individual filters. All filters have a Gaussian envelope standard deviation $\sigma = S/2 = 0.45 \mu\text{m}$. Background signal is measured through a glass specimen slide with no sample and is collected for all filters. Fluorescent image acquisition from the fixed and labeled cells is accomplished without Fourier spatial filtering, bypassing the LCD by sending the light through the trinocular port of the microscope to a CoolSnap CCD (Roper Scientific, Trenton, NJ). Differential interference contrast (DIC) images of labeled cells were also acquired on the CoolSnap CCD.

For dynamic study of apoptosis in unlabeled live cells, the Gabor filter bank is applied in time intervals of 10 minutes (STS treated) or 60 minutes (control) over a 12 hour

time period after STS addition. Each filtered image is collected at 50ms exposure. At each timepoint, unfiltered dark field are collected immediately before each stack of Gabor filtered images on the Cascade CCD. Gabor-filtered background images consisting of imaging an empty glass sample are collected with 50ms exposure at the start of each experiment at every filter angle φ and period S , and subtracted from the corresponding filtered images collected during dynamic studies.

DATA ANALYSIS

The data in this section are analyzed for PCA-based aspect ratio as described in Chapter 3, Section 3.6.3. Morphometric images encoding aspect ratio are scaled in a similar manner as used for the marine diatom: Brightness of indicates intensity of response while hue represents the aspect ratio parameter.

Although the nearly confluent preparation (Cell Culture and Optical Setup, Chapter 4, Section 4.4.1) results in a full field of view, in general there may exist background regions whose response must be excluded. To eliminate these areas, MATLAB image processing tools are used on the unfiltered dark-field images to automatically segment and remove background. A straightforward threshold to signal is inadequate owing to the dynamic range of response typical of dark field imaging. However, cells are rich in structure, and therefore have very textured morphologies. Conversely, background is generally smooth in texture. Therefore, a texture-based thresholding technique based on image gradient is used to delineate background from cells. The DF image gradients are calculated to highlight areas of high variability in the image (these areas correspond to structures and therefore are of interest); areas of low variability correspond to smooth background in the image. This image is then blurred using lowpass filtering to the resolution of the largest Gabor filter period used and then thresholded. The resulting mask preserves clearly cellular regions and discards

background (**Fig. 5-4**). These masks dictate which pixels are to be included in the analysis and are evaluated for each time point. In all cases, the gradient threshold is set conservatively to minimize the exclusion of any cellular areas.

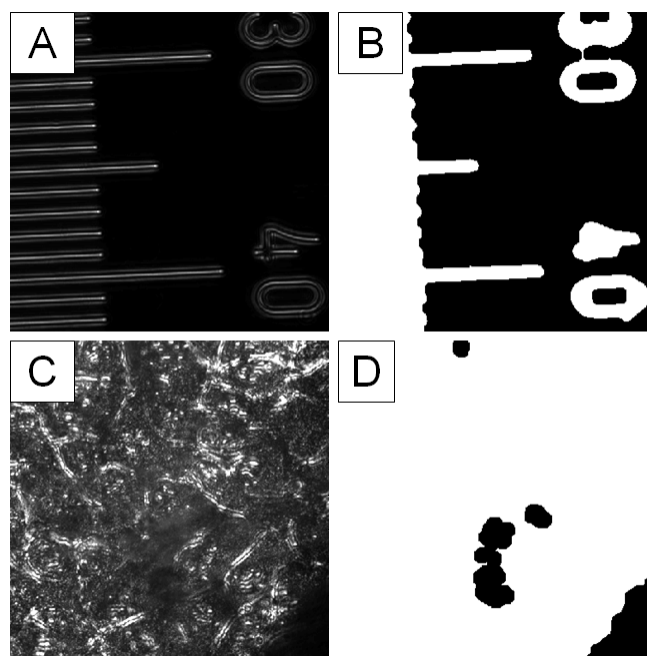


Fig. 5-4. (a): DF image of graticule. (b): Mask resulting from image segmentation routine applied to (a). (c): Representative field of iBMK cells under typical experimental conditions. (d): Mask resulting from image segmentation routine applied to (c).

5.2.2 RESULTS

There are several useful alternative methods used to render the data, including morphometric encoded images, histograms, and time traces, each with strengths and drawbacks, and each capable of highlighting different features of collected data. **Fig. 5-5** shows representative aspect ratio renderings of W2 cells at $T = 0$, $T = 2$ h and $T = 4$ h post-STS exposure. Areas excluded by the segmentation routine appear as black areas in the morphometric encoded images. Morphometric images have the advantage of spatial registration with the unfiltered images, and thus provide insight into which areas of the cell

are associated with a particular response. However, morphometric images do not easily lend themselves to global study of overall response, and so are most useful for close inspection of specific areas of the cell (as given in the analysis described in Chapter 4, for example).

Histograms of time response such as those given in **Fig. 5-6** provide a detailed global impression morphometric data. In **Fig. 5-6**, the morphometric data encoding aspect ratio pixel-by-pixel in **Fig. 5-5** is deposited into a histogram for aspect ratio values. Each time point shown is rendered in a separate histogram, thus generating the 3-dimensional evolution of aspect ratio over time shown in **Fig. 5-6**. Differential response to STS introduction is evident between W2 cells (**Fig. 5-6a**) and D3 cells (**Fig. 5-6b**). While histograms do not preserve the spatial information of morphometric images, they provide the highly quantitative description of aspect ratio behavior over time.

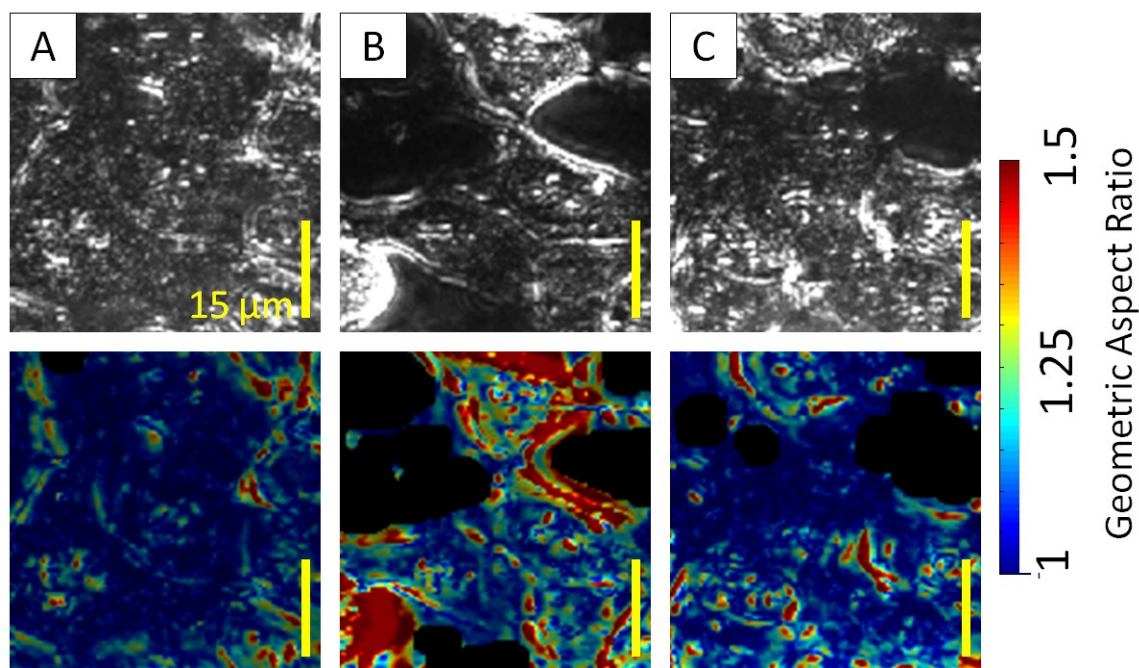


Fig. 5-5. Representative dark-field (top panels) and morphometric-encoded images (bottom panels) of PCA-based aspect ratio of W2 cells treated with 0.5 μ M staurosporine at $t = 0$ (a), $t = 2$ h (b), and $t = 4$ h (c) after staurosporine is introduced. Color hue indicates orientedness and color saturation is scaled to response intensity (the relative cumulative signal intensity collected from all Gabor filters). Figures are scaled to intensity of Gabor signal response as in **Fig. 5-1**, **Fig. 7-1**, and **Fig. 5-3**.

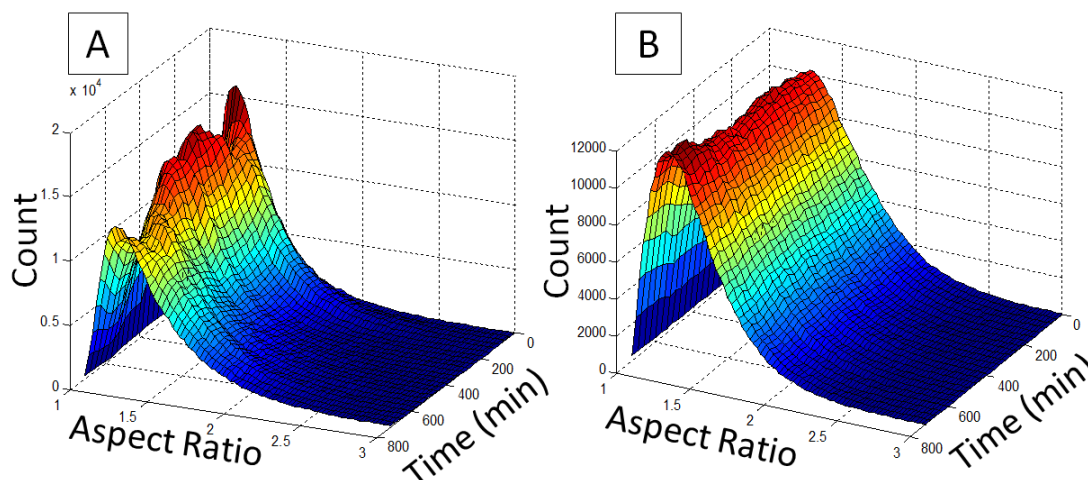


Fig. 5-6. Representative time response of aspect ratio histogram for W2 (a) and D3 (b) cells exposed to STS. A significant ($p < 0.01$) rise at ~ 1 -2 h, and subsequent drop (3-6h) in aspect ratio is detected for the W2 cells while little response is noted for the D3 cells. Number of W2 cells (N_{W2}) and D3 cells (N_{D3}) are ~ 30 each.

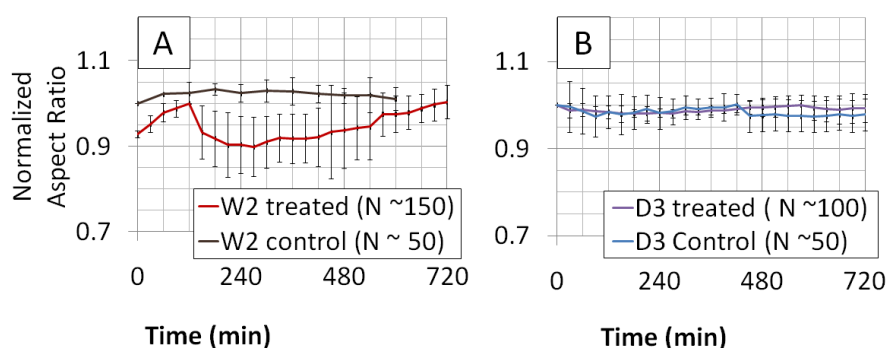


Fig. 5-7. Mean normalized aspect ratio time response of (a) apoptosis competent (W2) and (b) apoptosis resistant (D3) iBMK cells. W2 time response is normalized to maximum aspect ratio ($t = 120$ min.). All other time responses are normalized to first time point ($t = 0$). Due to difficulty in counting unlabeled cells in a confluent culture in DF, number of cells is approximate and is based on average cell density for preparation conditions.

Time traces (**Fig. 5-7**) are useful to detect global changes in morphology. The time traces shown in **Fig. 5-7** plot the mean normalized aspect ratio over all pixels for each time point (i.e. the mean of the histograms in Fig. 4-10) yielding an average plot of aspect ratio as a function of time after STS or DMSO treatment. **Fig. 5-7** indicates that the overall orientedness of the W2 cells behaves significantly ($p < 0.01$) differently from the D3 or control studies. A marked rise ($T = 1$ -2 hours, **Fig. 5-7a**) followed by a drop ($T = 2$ -4 hours, **Fig. 5-7a**) is observed for STS-treated W2 cells while there is little response from W2 under

control conditions. Additionally, the D3 cells show no global response to STS treatment and have similar responses for both STS and control treatments.

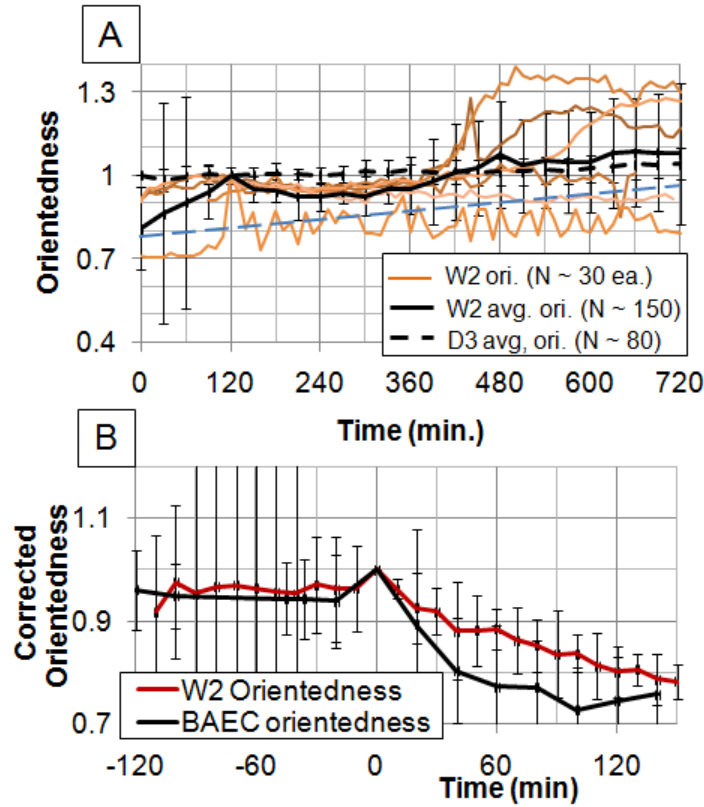


Fig. 5-8. Orientedness response of STS-treated iBMK cells for $S = 0.9 \mu\text{m}$. (a): Time traces of pixel-averaged orientedness for W2 cells treated with STS (orange traces), average W2 orientedness (solid black trace), and average D3 orientedness (dashed black trace) over time. Dashed blue trace represents slope of linear best fit to average W2 orientedness data ($y = .77 - 0.001x$) which is subtracted from average W2 orientedness data to achieve background correction. (b): Comparison of background-corrected W2 iBMK orientedness (red) with whole-cell BAEC orientedness as in Fig. 4-6 (black). Correlation between background-corrected W2 iBMK orientedness and whole-cell BAEC orientedness is 0.93. Error bars indicate standard deviation of the mean.

Although the changes in aspect ratio given in **Fig. 5-7** are reminiscent to those of BAEC, a direct comparison requires data analysis for orientedness on the iBMK data. Therefore, orientedness is calculated for the iBMK cells using the $S = 0.9 \mu\text{m}$ portion of the acquired filterbank and averaged over all pixels retained by thresholding described in

Chapter 5, Section 5.2.1 (**Fig. 5-8**). This analysis is similar to the results processing for aspect ratio (**Fig. 5-7**), and in both cases, a slow, steady upward trend is noted under which the suspected mitochondrial fragmentation signal is buried. Because the established mitochondrial signal is a rapid dynamic, and the uptrend is a slow process, the two are likely unrelated.

Therefore, in an effort to isolate the presumable mitochondrial signal from the remainder of the dynamic response, a background subtraction is performed on the iBMK W2 orientedness data. The background subtraction consists of a linear least-squares best-fit to the data, yielding a fit of $y = .77 - 0.001x$, whose slope is then subtracted from the dataset. The resulting background-corrected time trace (**Fig. 5-8b**, red trace) is then compared to the overall cell orientedness response for BAEC given in **Fig. 4-6** (**Fig. 5-8b**, black trace). When normalized such that the peak response is considered orientedness = 1 (instead of normalizing to start), and aligning the peak response position temporally ($\Delta t = 40$ min), the correlation between the two datasets is 0.93. This strong correlation indicates very similar dynamics embedded within both cell types, and mitochondrial fragmentation is highly suspected as a result.

MITOCHONDRIAL POTENTIAL

Live cell imaging of iBMK loaded with JC-1 indicates that JC-1 acts as a photosensitizing agent in iBMK cells (**Fig. 5-9**). Under the experimental conditions used for this study (imaging every 10 minutes with red laser light for Gabor filter collection), iBMK cells remain healthy and viable based on morphological appearance. However, when loaded with JC-1 and imaged to capture both Gabor data and red and green fluorescence, the W2 cells tested photosensitize and begin to deteriorate within 30 minutes. Moreover, this effect

occurs only within the irradiated field (**Fig. 5-10**), strongly suggesting that the toxic effect is light-dependent.

W2 cells labeled with mitotracker green (Invitrogen, 50 nM in growth medium for 30 min at 38 °C, 8.5% CO₂) reacted similarly under experimental conditions (imaging every 10 minutes with red laser light for DIC image collection in addition to capturing green fluorescence), suggesting that the photosensitivity is particularly associated with adverse effects to the mitochondria (**Fig. 5-11**). In order to visualize the "bull's-eye" pattern of cell deterioration, **Fig. 5-11** is comprised of several adjacent and overlapping fields of view aligned into a photographic montage. The time lapse for cells treated with mitotracker green was 12 h (because of photobleaching, the fluorescent images are not shown) for **Fig. 5-11**. The iBMK cells' photosensitivity to mitochondrial labels necessitates using fixed samples in order to monitor mitochondrial changes in fluorescence.

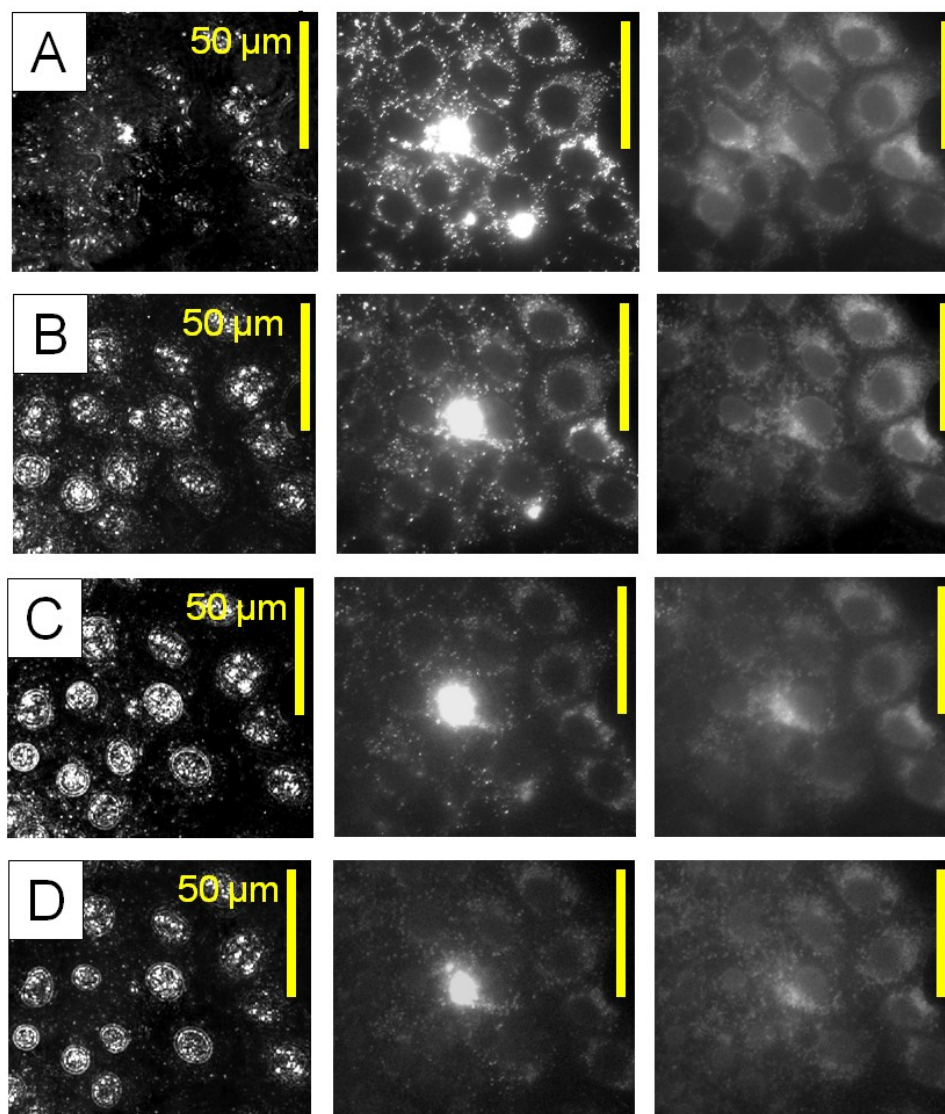


Fig. 5-9. JC-1 time lapse imaging. DF images (left column of image panels, exposure time 50 ms), red JC-1 fluorescence (middle column, exposure time 200 ms) and green JC-1 fluorescence (right column, exposure time 200 ms) of W2 cells labeled with 1 $\mu\text{g}/\text{mL}$ JC-1 under experimental conditions, without STS treatment. Imaging commenced at $T = 0$ (a) immediately after mounting the cells to the microscope stage. At this time point, healthy polarized mitochondria are abundant as evidenced by the numerous bright, punctate regions in (a, center panel). After 30 minutes (b), 1 hour (c) and 2 hours (d) of imaging, the cells steadily deteriorate. The DF presentation worsens as the cytoplasm becomes less distinct and structured and the cell nuclei shrink markedly. This is accompanied by an almost total disappearance of bright punctate regions of red fluorescence (center column) indicating a commensurate loss of mitochondrial potential.

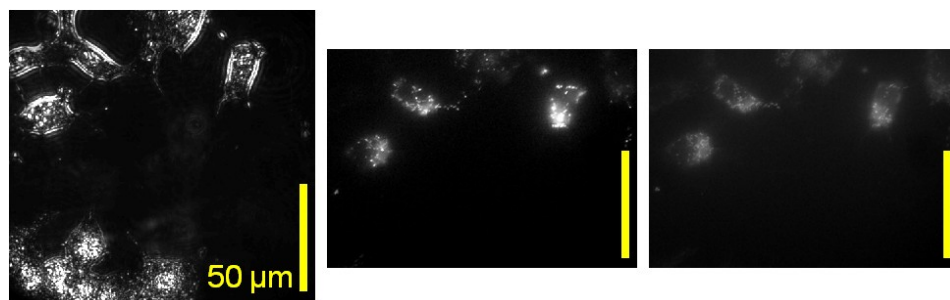


Fig. 5-10. DF images (left, exposure time 50 ms), red JC-1 fluorescence (center, exposure time 200 ms) and green JC-1 fluorescence (right, exposure time 200 ms) of W2 cells labeled with 1 µg/mL JC-1 under experimental conditions, without STS treatment. The field of view shown is adjacent to the one imaged in **Fig. 5-9**. The edge of the field irradiated for time lapse imaging lies approximately halfway up from the bottom of the DF image. The bottom cells (irradiated in time lapse) closely resemble the appearance of those in **Fig. 5-9** after the time lapse while the cells in the top portion of the image (not irradiated in time lapse) resemble the W2 cells in **Fig. 5-9a** at the start of imaging ($T = 0$). The cells not imaged in time lapse (top) also have similarly high levels of red fluorescence in bright, punctate regions indicating healthy mitochondria (center panel).

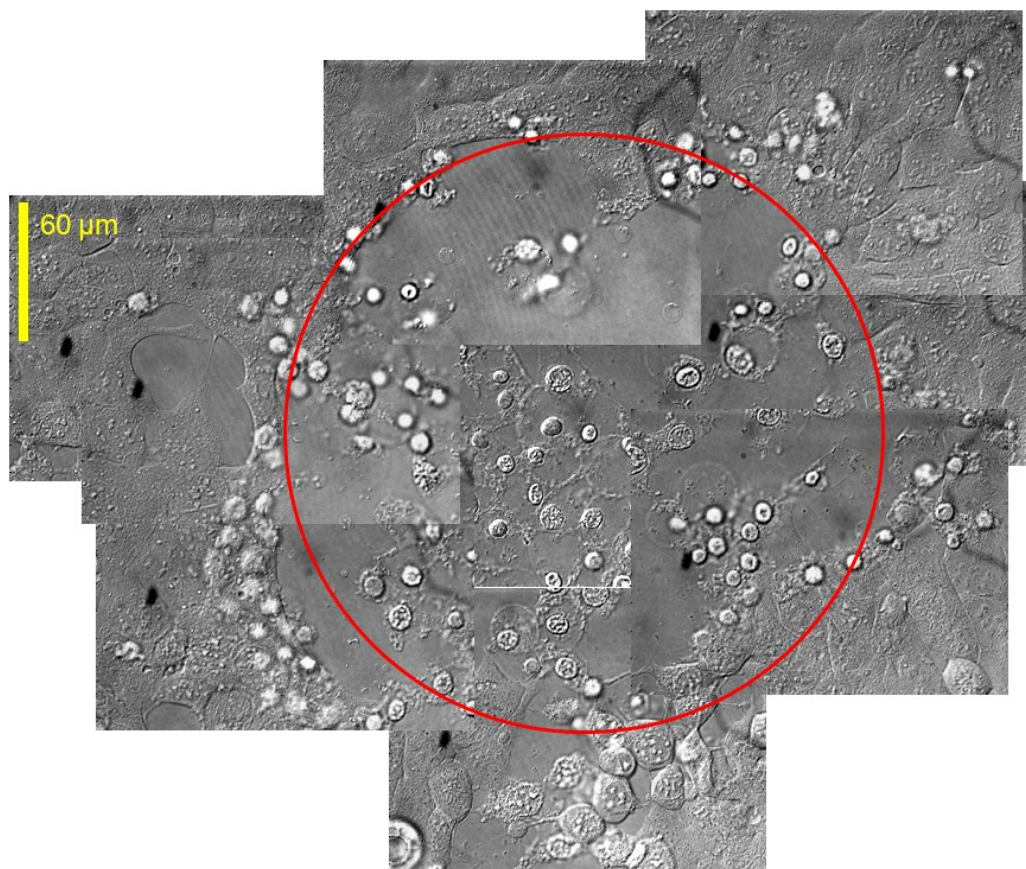


Fig. 5-11. DIC montage of irradiated field of view and surrounding vicinity. Sample consists of W2 cells labeled with 50 nM mitotracker green in growth medium for 30 min at 38 °C, 8.5% CO₂ which was then subsequently given 200 ms of blue fluorescent excitation every 10 minutes over 12 h under experimental conditions. The time-lapse irradiated area (enclosed by red circle) is roughly 250 µm in diameter. Cells within this area are highly deteriorated in comparison with cells removed from the circle.

Fig. 5-12 shows representative data for JC-1 fluorescence of fixed W2 and D3 cells at $T = 0$ and $T = 4$ h for STS. Unlike cells that are continually irradiated, cells that are labeled, incubated without irradiation, and fixed remain healthy in appearance. W2 cells and D3 cells fixed at $T = 0$ (i.e. immediately after brief transferral to microscope viewing medium after removal from JC-1 incubation) show numerous regions of red punctate fluorescence indicating the presence of healthy polarized mitochondria. W2 cells fixed at $T = 4$ h post STS introduction show a significant decrease (56%) in the relative amount (red/green intensity ratio) of red fluorescence as compared with $T = 0$ indicating a loss of mitochondrial membrane polarization during this time. In contrast, D3 cells show only a 4% decrease over the same period. For both W2 and D3, the $T = 0$ and $T = 4$ hour images represent separate specimens (one each of W2 specimen prepared at $T = 0$, W2 specimen prepared at $T = 4$ h, D3 specimen prepared at $T = 0$, specimen prepared at $T = 4$ h) from fresh fields of view to minimize effects on measured signal from photobleaching.

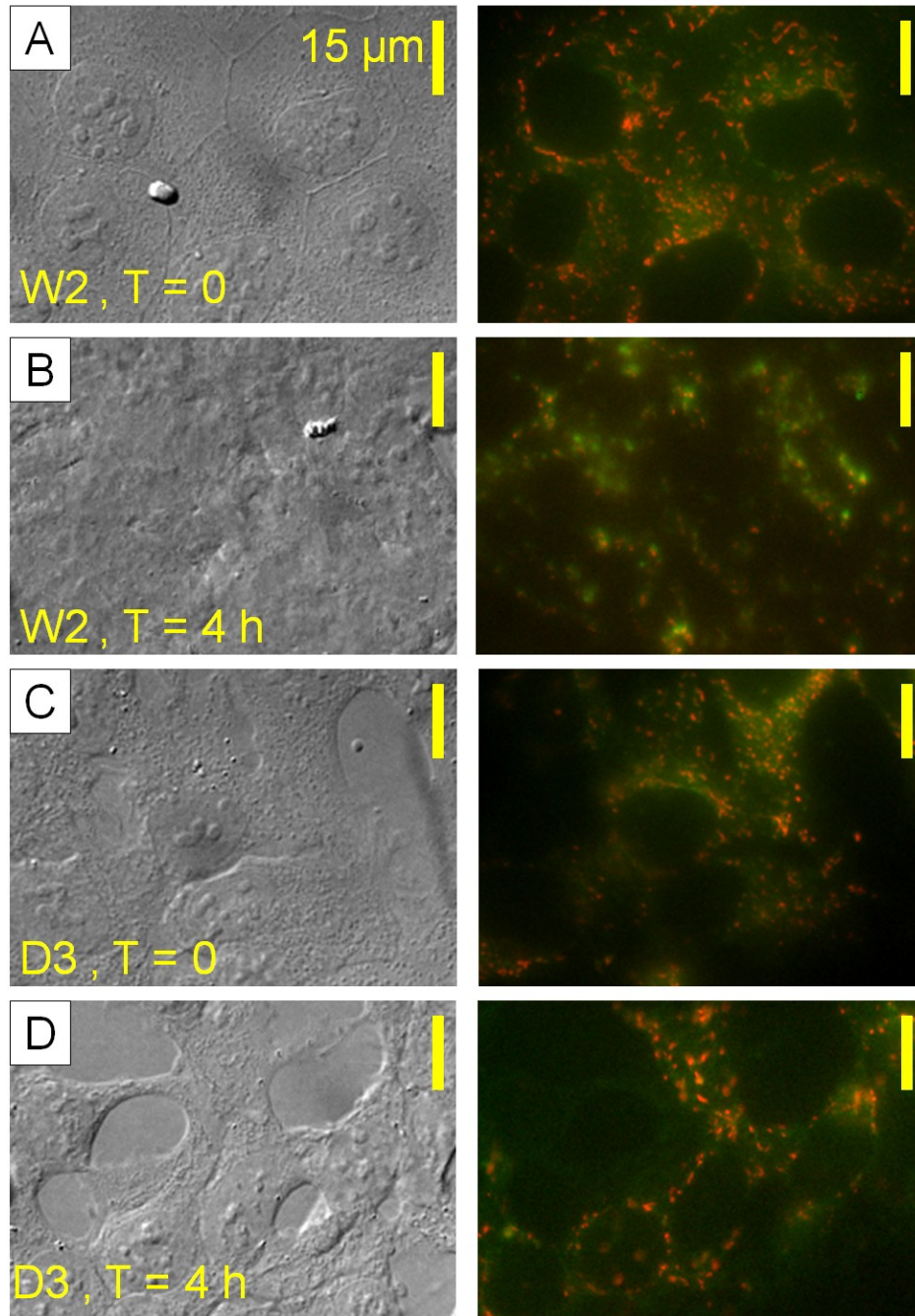


Fig. 5-12. Fixed iBMK JC-1 fluorescence (a): DIC (left panel) and dual-channel fluorescence (right panel) in W2 cells at $T = 0$. Punctate red regions correspond to mitochondria with high membrane polarization (negative potential) and green diffuse areas correspond to areas of low potential. (b): DIC (left panel) and dual-channel fluorescence (right panel) in W2 cells at $T = 4$ h. Reduced red fluorescence indicates a generalized loss of mitochondria membrane potential consistent with apoptosis. (c): DIC (left panel) and dual-channel fluorescence (right panel) in D3 cells at $T = 0$. (d): DIC (left panel) and dual-channel fluorescence (right panel) in D3 cells at $T = 4$ h. In contrast to W2 (B), no reduction in membrane potential as reported by JC-1 is noted after 4 h STS treatment.

5.2.3: DISCUSSION

By using optical imaging with Gabor spatial filtering, this study demonstrates sensitivity to changes in light scattering from iBMK cells in response to STS treatment. Because the results from Chapter 4 suggest mitochondrial fragmentation is detectable as a drop in orientedness early in apoptosis, this study utilizes PCA analysis in order to study aspect ratio of the aggregate filter-bank response, pixel-by-pixel, over time. This study handles the data by taking the integrative approach whereby all the data contribute to a single morphometric parameter. The advantages of this approach lie primarily in the ease of interpretation of the analysis. A parameter such as aspect ratio is straightforward to interpret physically. Other morphometric parameters (such as size (Chapter 3) or eccentricity (i.e. the degree to which antipodal signal in the Fourier plane is asymmetric) would also involve an integrative synthesis of the data and could be similarly useful. On the other hand, this approach has drawbacks, the most serious of which is the loss of information associated with data reduction, and (depending on the analysis method) the extensive computation required. Overall, in the context of using these data to arrive at a simple, easy-to-interpret, and sensitive morphological metric, the advantages of using this approach outweigh these drawbacks.

Using the PCA approach to arrive at an aspect ratio metric, a differential response to staurosporine is observed for W2 and D3 cells (**Fig. 5-7**). W2 cells undergo a rise-then-drop dynamic between 0-4 hours in aspect ratio while for D3 cells this effect is absent under the same conditions. Incubation and fixation of W2 and D3 cells show that W2 cells' mitochondria lose membrane polarization over the same time frame while D3 cells remain unchanged (**Fig. 5-12**), suggesting a correlation between the rise-then-drop dynamic and loss of mitochondrial polarization. It is interesting to note that the rise-then-drop dynamic is

different from the drop in orientedness noted for the study of BAEC (Chapter 4). Although responses may be cell-type dependent, future analysis should rule out the possibility of additional or different dynamics in the iBMK cells other than mitochondrial fragmentation in a manner similar to that used in Chapter 4. Overall, however, the presentation and timing of the rise-then-drop event, combined with its absence from untreated and resistant (D3) cells supports the hypothesis that this event is apoptosis-related.

Difficulty with live cell imaging of the fluorescently labeled iBMK cells (**Fig. 5-10**, **Fig. 5-11**) showcases the usefulness of label-free methods such as optical Gabor filtering. In this case, the adverse reaction is extreme and results in the complete destruction of the cells within hours, and therefore required independent incubation and fixation of separate samples in order to investigate mitochondrial potential (**Fig. 5-12**) alongside the optical study. However, this results also makes validation difficult, as the spatial information gained by tracking organelles (as in Chapter 4) is very useful in validating the optical response.

The W2/D3 model is useful because it allows for probing the apoptotic response with respect to the presence/absence of bax/bak. During apoptosis, Bax translocates to mitochondria and coalesces with Drp-1 and Mitofusin 2 (Mfn-2) at mitochondria fission sites (35). Bax seems to be required to stabilize Drp-1 localization on the mitochondria (36), implying that its absence (as in the D3 cells) disrupts the mitochondrial fission process. Recent studies indeed suggest that mitochondrial fragmentation is downstream of bax localization to the outer mitochondrial membrane, and that mitochondrial fragmentation mediated by Drp-1 requires colocalization of bax at fission sites and occurs after bax/bak colocalization (35) (the downstream hypothesis). As alluded to in Chapter 1, Arnoult et al. (39) show that Drp-1 activation may proceed retroactively from DDp/Timm8a (an

mitochondrial intermembrane space protein) release after permeabilization. Arnoult et al. also propose that Opa-1 (also released from the intermembrane space after permeabilization) may be similarly recruited to fragment the mitochondrial network (40). If the aspect ratio dynamic of the W2 cells is indeed caused by mitochondrial fragmentation, these results are consistent with the downstream hypothesis inasmuch as the aspect ratio response is absent from the D3 cells.

In this study, the comparison between aspect ratio responses of the W2 and D3 cells shows divergent responses for each. However, it is not immediately clear from this study whether or not these optical changes are associated with mitochondria directly. Although the iBMK orientedness and aspect ratio responses are similar to those of BAEC, their attribution to mitochondrial fragmentation remains unproven. This method, while sensitive, does not provide structural information with biological specificity, and therefore a study of iBMK cells with fluorescent labeling is warranted.

4.3 DISCUSSION

This chapter explores the iBMK W2/D3 cell model and studies the differences between W2 and D3 cells using the optical Gabor filtering methodology. The orientedness response of the W2 is slightly higher overall than the D3 cells (Chapter 4, Section 4.1) under normal conditions. Time-dynamic studies of apoptosis (Chapter 4, Section 4.1) show significant differences in aspect ratio response for W2 and D3 cells, suggesting that difference in the response observed for W2 cells can be used as archetypical apoptosis optical aspect ratio response. Further study is required to establish that this response is unique to apoptosis; however, the work here shows that it is possible to detect the effect of

the presence/absence of bax/bak and thus to detect apoptosis without the need for labeling, fixation, or protein assays. The measurement was successfully made with minimal disturbance to the cells themselves.

The optical Gabor filtering method is not dependent on the digital image resolution and does not require any dyes or labels. However, dyes and labels are extremely important to establish biological specificity and therefore to validate the significance of the measured response. In this case, validation proved problematic because of the severe effect that the dyes which would have been used to assist in validation were highly photosensitizing. It is necessary to establish the biological structure responsible for the optical response directly in order to render this method biologically specific. Therefore, although the measured optical response is similar (but not identical) to the BAEC response and the presentation and timing of the response are consistent with mitochondrial fragmentation, future studies will be aimed at arriving at a validation for the optical response directly in iBMK cells. By labeling the mitochondria and using the registered fluorescent images to create two distinct regions (mitochondria-rich and mitochondria-poor), the Gabor filter response may be segregated to these regions and the hypothesis that the drop in aspect ratio is indeed arising from mitochondrial fission events may be tested in iBMK directly.

CHAPTER 6 : OPTICAL SCATTER IMAGING AT THE ONSET OF APOPTOSIS

- This chapter includes work published in (97) Pasternack RM, Zheng J-Y, Boustany NN. “Optical Scatter Changes at the Onset of Apoptosis Are Spatially Associated with Mitochondria”, *Journal of Biomedical Optics Letters*.15, 040504; doi:10.1117/1.3467501, (2010).

6.1: INTRODUCTION

The previous chapters describe work whose aim was to design, develop, characterize, and employ the optical Gabor microscopy method in studying mitochondrial morphology during the onset of apoptosis. This study revealed morphometric dynamics which could be associated with mitochondria in BAEC cells and which are mediated by Bax/Bak in iBMK cells. The work in this chapter uses the DMD-based system to perform OSI under the same conditions. Boustany et al. (74) discovered changes in optical scatter during the first hour of apoptosis using the OSI method. In continuity with the work begun by Boustany et al. (74) and Zheng et al. (75), the DMD setup was also employed to perform OSI on apoptotic BAEC in conjunction with the Gabor filtering study of Chapter 4 in order to confirm and extend the findings of these earlier studies, and to determine the source of this dynamic using the fluorescence-based pixel segregation method described in Chapter 4 Section 2 and Chapter 4 Section 3.

Programmed cell death (apoptosis) is regulated by a balance between pro-survival and pro-death factors that converge on the mitochondria (Chapter 1). Mitochondrial permeabilization by pro-apoptotic proteins Bax and Bak is a critical event in the apoptosis pathway, as it allows cytochrome c release and downstream caspase activation, and cell death (4). In addition, Bax/Bax localization to the outer mitochondrial membrane occurs nearly simultaneously with Drp1-mediated mitochondrial fragmentation (5). From an optics

standpoint, mitochondria are highly scattering and account for most of the light scattered by organelles in the cytoplasm (88). Thus, several studies have shown alterations in light scattering concurrent with alteration in mitochondrial function and structure during apoptosis (65; 74; 95). In this work, we extend these previous studies by demonstrating that optical scatter changes occurring within the first three hours of apoptosis are spatially registered with mitochondria, therefore lending significant support to the hypothesis that mitochondria act as the source of optical scatter changes early during apoptosis.

6.2: METHODS

We used bovine aortic endothelial cells (BAEC, Clonetics Lonza, Chicago, Illinois) cultured on glass coverslips as previously described in Chapter 4. For fluorescence imaging, the cells were labeled with 100-nM Mitotracker Green (Invitrogen, Carlsbad, California), which specifically localizes in the mitochondria. The coverslips were mounted and viewed in non-CO₂-dependent Leibovitz L-15 medium (Invitrogen) supplemented with 10% fetal bovine serum (FBS) at room temperature and room air. Apoptosis was induced by exchanging the cells' normal viewing medium for viewing medium containing 1- μ M staurosporine (STS) (Sigma Chemical, Saint Louis, Missouri) prepared from a 4-mM staurosporine stock solution in dimethyl sulfoxide (DMSO) (Sigma). Control studies consisted of loading L-15 +10% FBS with only DMSO in the same volume in place of the STS solution. The apoptotic fate of BAEC treated with STS was separately confirmed by positive immunofluorescence of cleaved caspase 3.

The cells were studied on the optical Fourier processing microscope described in (80), fitted and aligned with a 63x oil immersion objective with a numerical aperture (NA) of 1.4. Optically filtered images were acquired on a Cascade 512B charge-coupled device (CCD)

(Roper Scientific, Trenton, New Jersey). Fourier filtering was achieved with a TI0.7XGADMD 1100 digital mirror device (DMD) (Texas Instruments, Dallas, Texas). We applied the variable-diameter irises to the DMD to implement our previous OSI method (72), which consists of taking the ratio of two central dark ground images collected at high and low NA. In the present setup, the high NA iris had an outer radius of 180 mirrors (corresponding to the objective's full NA=1.4). The low NA iris had an outer radius of 34 mirrors (corresponding to $NA_{\text{low}}=0.26$). The beam block at the center of the irises was 16 mirrors wide and blocked an NA of 0.06. Images of background consisting of a glass coverslip with no sample were collected with the same high and low NA apertures. The dark-field images were processed as described previously (72) by taking the ratio of the background-subtracted high and low NA images to generate ratiometric images encoding the OSIR, giving a measure of wide-to narrow angle scatter at each pixel. As established in Boustany et al. (72), a larger OSIR is associated with smaller particle size. Based on our work with different cell types, we have found that the OSIR signal from mitotracker labeled cells is not significantly different compared with unlabeled cells.

OSI was applied in time intervals of 20 min over a three-hour time after STS addition at $T=0$. For cells treated only with DMSO (controls), we repeated the optical acquisition taking data every 50 to 60 min over a six-hour time. At each time point studied with the OSI technique, fluorescent images of the mitotracker-labeled cells were acquired with a fluorescein isothiocyanate (FITC) filter cube (filter number 10, Carl Zeiss, Gottingen, Germany), and without Fourier spatial filtering, bypassing the DMD by sending the light through the trinocular port of the microscope to a CoolSnap CCD (Roper Scientific). Differential interference images of the cells were acquired on both cameras. This allowed for registration of the background-subtracted dark-field images, and therefore the OSI images,

with the DIC and fluorescence images. The cells were segmented manually and data analysis was confined to these cell segments.

6.3: RESULTS

Morphometric images encoding the OSIR are shown in **Fig. 6-1** for a representative cell, along with DIC and fluorescence images at $T=0$ (immediately after STS treatment), and 40 and 140 min. after STS addition. For cells treated with STS, the average value of the OSIR per cell, normalized to the value at the start of the experiments ($T=-120$ min) shows that the OSIR drops within the first 60 min of exposure to STS, and then steadily rises between 60 and 180 min (**Fig. 6-2** black diamonds). In contrast, the OSIR remains largely unchanged for cells treated with only DMSO (**Fig. 6-2** white diamonds). In the fluorescent images, mitochondria evolve from a long, filamentous morphology to shorter, smaller, and rounder shapes between 60 and 140 min (**Fig. 6-1c**). This is consistent with previous observations of mitochondrial fragmentation in cells undergoing apoptosis.² However, no gross changes in mitochondrial morphology could be discerned during the first 60 min of STS treatment.

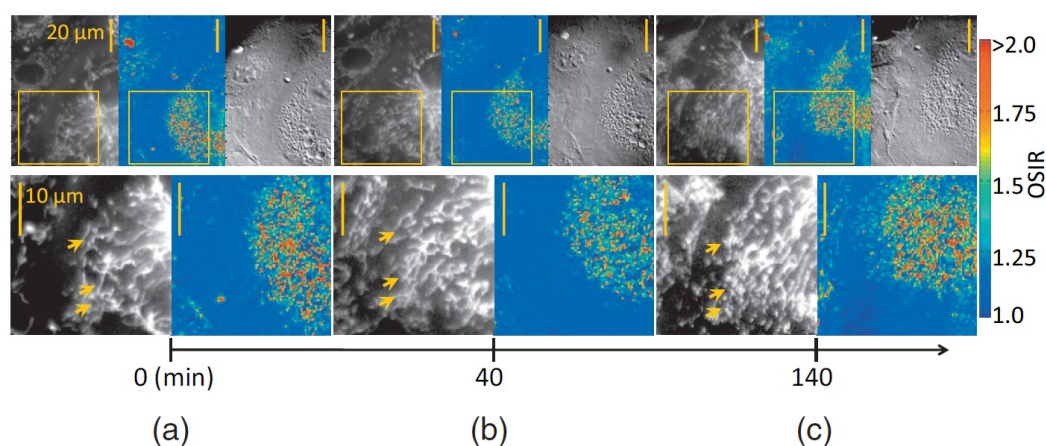


Fig. 6-1. Top row: fluorescence (left), OSI (middle), and differential interference contrast (right) images of a representative cell immediately after 1- μ M STS treatment at (a) $T=0$, (b) $T=40$ min, and (c) $T=140$ min after STS addition. Bottom row: magnified fluorescence and OSI insets showing mitochondrial fragmentation (arrows).

Since the OSI method allows for spatially localizing the optical scatter changes within the cells, we investigated if the OSIR changes measured at the whole cell level (**Fig. 6-2**) could be specifically associated with subcellular regions containing mitochondria based on the fluorescence images of the labeled mitochondria. To correct for fluorescence background, each raw fluorescent image (**Fig. 6-3a**, top panel) was filtered using a digital Gabor filterbank as in (91) composed of filters with period S , equivalent to $0.9\ \mu\text{m}$ in the object, Gaussian envelope $\sigma_s = S/4 = 0.225\ \mu\text{m}$, and orientations from 0 to 160 deg with 20-deg increments. Because the Gabor filter period S is most sensitive to object features $\sim S/2$ in size, S was once again chosen to be twice the average short-axis diameter of mitochondria (0.3 to $0.6\ \mu\text{m}$) (96).

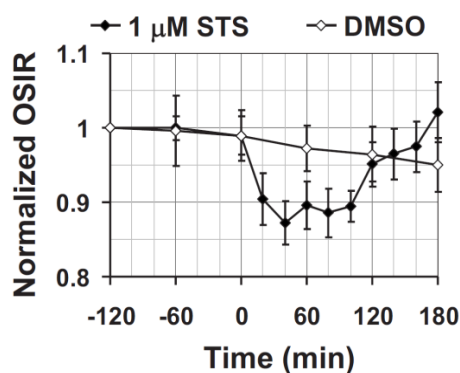


Fig. 6-2. OSIR change as a function of time for STS (black diamonds) and DMSO (white diamonds) treated cells. The value at each time point is the mean OSIR per cell normalized to the mean OSIR per cell at $T = -120$ min. Error bars indicate \pm the 95% confidence interval of the mean. STS ($1\ \mu\text{M}$) or DMSO was added at $T = 0$.

The Gabor filtered fluorescent images were then summed to yield a background-corrected fluorescent image (**Fig. 6-3a**, bottom panel). At each time point, each cell segment was further divided into two regions, one dominated by bright fluorescent mitochondria and the other by the remaining dim background consisting of other nonfluorescently labeled organelles (**Fig. 6-3b**) by applying an intensity threshold. This threshold was normalized to

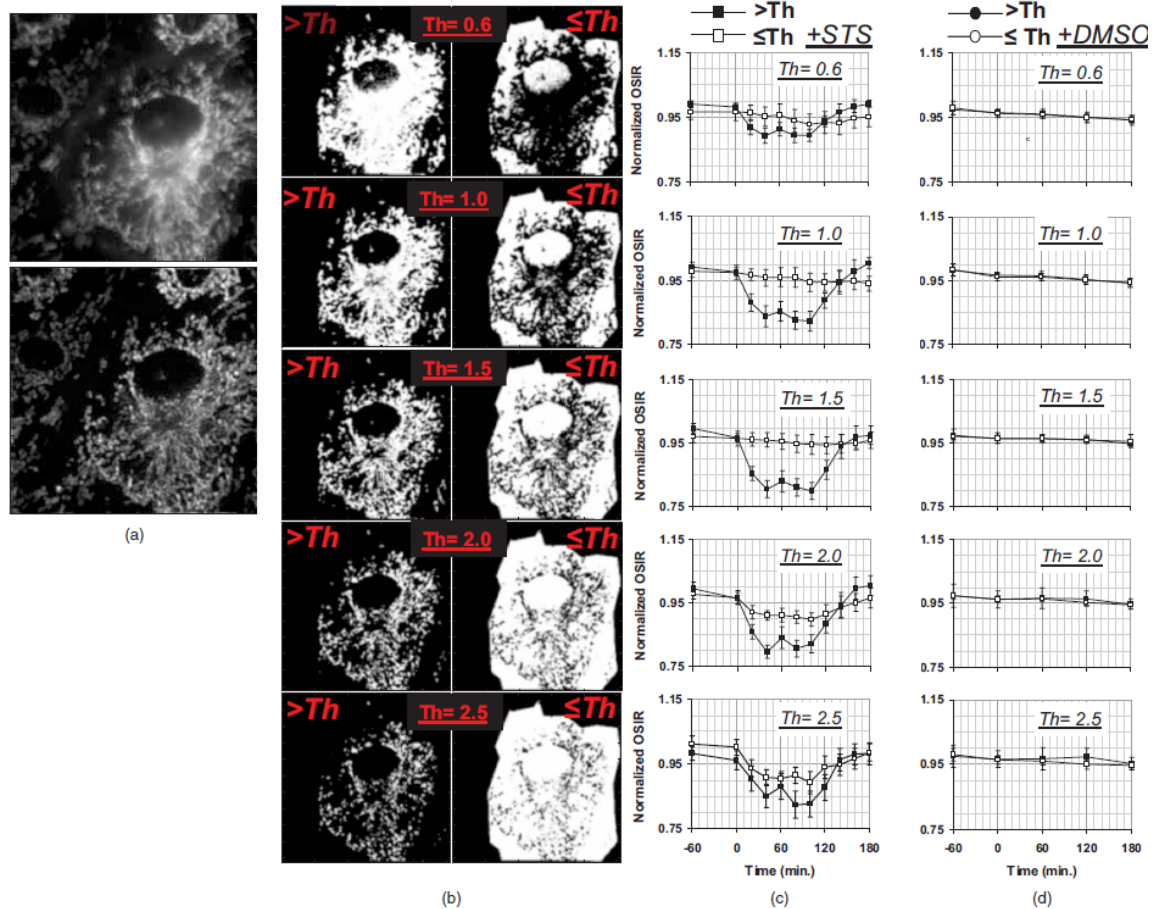


Fig. 6-3. (a) Representative raw fluorescence image (top panel) and Gabor filtered fluorescence image (bottom panel) used for thresholding study (images are shown for $T=-60$). (b) Representative binary subcellular masks (shown for one cell) with fluorescence intensity above ($>Th$) or below ($\leq Th$) threshold. The threshold value (Th) was normalized to the average fluorescence intensity within a given cell segment. (c) and (d) Mean OSIR per masked cell $\pm 95\%$ confidence interval as a function of time in the subcellular regions with fluorescence above threshold (filled squares) or below threshold (open squares). Data are shown for (c) STS and (d) DMSO treated cells, and for different values of Th .

the average fluorescence intensity within a given cell segment. For example, if a threshold of 1 ($Th=1$) is chosen, all the fluorescent pixels with intensity values greater than the average intensity value for that cell are taken as fluorescent, and all the pixels with values less than or equal to the average intensity are taken as nonfluorescent. Once chosen, the normalized threshold value was the same for all the cell segments studied, and all pixels within each single cell segment were included in this analysis. The bright and dim fluorescent areas were then separately applied as a mask to the OSI images to compare the optical scatter changes

within the brightly fluorescent areas rich in mitochondria, versus dim regions dominated by nonfluorescent organelles. **Fig. 6-3** shows the results of this analysis for different choices of threshold values.

For the STS-treated cells (**Fig. 6-3c**), as the threshold is increased from $Th=0$ (corresponding to whole cell analysis), less of the nonfluorescent pixels are included in the region designated as fluorescent, and the decrease in OSIR becomes more pronounced in the fluorescent region compared with the nonfluorescent one. Up to a threshold $Th=1.5$, changes in OSIR are negligible in the designated nonfluorescent regions below threshold. By choosing the threshold around the average fluorescence intensity ($Th=1.0$ to 1.5), we were able to clearly separate the OSIR dynamic between the fluorescent areas above and below threshold. For very high thresholds ($Th \geq 2.0$), pixels that are clearly fluorescent are designated as nonfluorescent, and the optical signal changes become detectable in both the regions above and below threshold. These behaviors are absent from DMSO control studies (**Fig. 6-3**), in which neither the above-threshold nor the below-threshold regions show significant changes in OSIR over this time frame.

6.4: DISCUSSION

The results in **Fig. 6-3c** suggest that the optical scatter changes is spatially localized in subcellular regions containing mitochondria. If the OSIR changes were nonspecifically associated with all or most organelles within the cells, then all subcellular regions would be expected to be altered equally, and the changes in OSIR could not have been modulated by changing the fluorescence threshold value, as was done in **Fig. 6-3c**. If, on the other hand, the OSIR changes were associated with organelles other than mitochondria, then the trends in **Fig. 6-3c** for the regions above and below threshold would have been reversed. Instead,

we find that the regions with fluorescence intensity below $Th=1.5$ experience negligible OSIR change, showing that subcellular regions dominated by organelles other than mitochondria (“background”) do not contribute appreciably to the measured scattering change, and that the source of the optical scatter change exists within the designated fluorescent segments. This value of $Th=1.5$, which could separate well mitochondria from background in our system, could vary depending on the extent of fluorescence staining and the concentration of mitochondria within the cells under study. While the thresholding approach is computationally very simple, a more robust criterion could be found by utilizing a nonthreshold-based segmentation algorithm (e.g., texture-based) to isolate the mitochondria-rich regions.

The increase in the OSIR signal between 60 and 120 min after STS addition was visibly accompanied by mitochondrial fragmentation, as observed in the fluorescence images. Thus, the increase in OSIR after 60 min likely reflects an overall decrease in particle size due to this fragmentation process. Current results (91; 92) utilizing orientation-dependent light scattering measurements support this hypothesis by showing a decrease in the degree of particle orientation at the time of mitochondrial fragmentation. The decrease in OSIR within the first hour of apoptosis reproduces previous data (72; 74), but is more difficult to interpret from a biophysical standpoint. While we show here that this decrease spatially registers with mitochondria, it was not accompanied by discernable changes in the fluorescent images. These scattering changes could reflect ultrastructural changes in the mitochondrial matrix. This is possible because the OSI technique, which does not rely on the visualization of the scatterers, can be sensitive to changes in particle size that are below the imaging resolution limit (72). In addition, in our previous work, we found that changes in

light scattering could be accompanied by changes in mitochondrial ultrastructure (75) without necessarily resulting in changes in morphology visible in fluorescence.

The spatial extent of the mitochondria-rich, above threshold ($>Th=1.5$) fluorescent segment is limited by optical resolution and imperfect thresholding and segmentation, and could include a small percentage of nonfluorescent organelles surrounding the mitochondria. However, in our discussion so far, we have assumed that the potential presence of these organelles in the designated fluorescent regions would only add a static background based on the static scatter response of nonfluorescent organelles in the adjacent designated nonfluorescent regions ($\leq Th=1.5$). Still, it is possible that organelles that are structurally less active away from the mitochondria may be subject to mitochondrial signaling during apoptosis. Thus, when closely associated with mitochondria, some organelles (e.g., the endoplasmic reticulum) may change their structure during apoptosis, potentially giving rise to the OSIR changes observed in the designated fluorescent segments. This possibility may be unlikely, given the strong scattering contribution of mitochondria compared to other organelles (88). But to completely rule it out, the structural changes accounting for the OSIR decrease within the first hour of STS treatment remain to be fully elucidated. In conclusion, our results strongly point to the mitochondria as the likeliest source of the optical scatter changes measured in the first three hours of apoptosis induced by staurosporine. Mitochondria may give rise to these optical scatter changes directly through alterations in mitochondrial structure, or indirectly via signaling from mitochondria to organelles in their immediate vicinity.

CHAPTER 7 : SUMMARY & IMPLICATIONS FOR FURTHER RESEARCH

This section describes work published in (98), Pasternack RM, Zheng J-Y, Qian Z, Zhou J, Metaxas DN, White E, Boustany NN. “Optical Processing of Cell and Tissue Structure”, Workshop on Microscopic Image Analysis with Applications in Biology (MIAAB2009), NIH Campus, Bethesda, MD, Sep 3-4 2009.

7.1: SUMMARY

This thesis demonstrates the feasibility of an apoptosis assay using optical Gabor filtered dark field images to extract quantitative morphometric information from living cells. It is possible to generate encoded images of morphometric parameters such as size and orientedness to quantify subcellular morphology associated with important biological processes such as apoptosis.

The apoptosis assay approach using optical Gabor filtering was developed conceptually as an extension OSI (Chapter 2). The present method uses the same approach of placing a spatial filter (in this case a DMD or LCD) in a conjugate Fourier plane to the back focal plane of the objective to achieve the optical Fourier filtering. Gabor filters were chosen based on their sensitivity to specific morphological parameters while remaining spatially confined, and their tunability to specific sizes and orientations (Chapter 3). Because the morphological parameters of the filter are embedded in the impulse response of the filter directly, the resulting filtered image yields morphological information directly, without the need for a predictive scatter model.

The optical setup constructed to implement the optical Fourier filtering accommodates the addition of the SLM (DMD or LCD). Both the DMD-based system and LCD-based system are used throughout this work, each using specific optical configurations to optimize the performance of each. Zheng et al. had replaced the manual iris with the

DMD (79) to allow for greater precision in the OSI measurement as well as the possibility of other filtering schemes. They chose the DMD for its superior contrast ratio, as the OSI measurement cannot be made without high contrast between on and off pixels. Initially, Gabor filtering was implemented on the DMD, but the need to cycle binary concentric discs on the DMD to implement the filtering was inconvenient, and the limitations in transfer function and ultra-narrow-band illumination were overly restrictive (Chapter 2). The DMD was therefore replaced with an LCD device, and the LCD's superior transfer function and 8-bit grayscale amplitude modulation proved critical to improving and simplifying the overall performance of the system. This change also simplified the automation of the hardware by eliminating the need for binary image cycling as the CCD is exposing. The improved transfer function allowed us to improve the optical design and fill more of the device within the Fourier plane, improving spatial frequency resolution (Chapter 2).

A key concept developed in this thesis is the filterbank (Chapter 2). By using a series of Gabor filters applied sequentially, it is possible to generate a stack of spatially filtered images, each yielding a specific morphological response to each filter. This stack of images may then be subject to post-processing to derive quantitative morphological information about the specimen as a whole. The nominal sensitivity and dynamic range of sensitivity to changes in object size for $NA = 0.75$ and $NA = 1.4$ imaging conditions and the nominal sensitivity to changes in the spatial frequency of periodic objects is established, and in both cases demonstrate regimes in which digital post-processing fails while the optical acquisition remains sensitive (Chapter 3). We establish that analog processing confers advantage in that digital processing is limited by digital image resolution while optical processing is achieved independently of digital image resolution at the CCD.

Developing a simple metric ("orientedness") based on signal aspect ratio calculated pixel-by-pixel (Chapter 3) allows for the detection of quantitative differences in subcellular morphology between apoptosis competent cells (iBMK W2 and BAEC cell models) and bax/bak knockout cells (iBMK D3 cell model) (Chapters 4, 5). This approach is applied to monitor apoptosis in endothelial cells in time lapse, which measured a significant decrease in orientedness during the first 1-2 hours after apoptosis induction by STS that was absent from control preparations. With the aid of DIC and fluorescence multi-modal acquisition, the work in the endothelial cells demonstrated that the source of this decrease was localized to pixels spatially associated with the labeled mitochondria (Chapter 5).

The development of the automated LCD system allowed for easy acquisition of much more extensive filterbank image stacks. As a result, the simple "orientendess" metric had to be generalized to accommodate filterbanks that probe over both size and azimuthal angle. An aspect ratio metric was developed by using PCA to determine the eigenvalues and eigenvectors of the data (Chapter 4). The eigenvalues and eigenvectors form the basis of an aspect ratio representation of the data whose aspect ratio may be calculated.

Taking full advantage of the LCD system, the iBMK cell model was used to probe the differential optical response to apoptosis induction by staurosporine in an effort to establish morphological dynamics associated with the apoptosis process (Chapter 4). The apoptosis competent (W2) cells showed an early dynamic response consistent with, but not identical to, the results from the endothelial cell studies while the D3 (apoptosis resistant) cells showed little response. Fluorescent labeling and imaging for mitochondrial potential confirmed a loss of mitochondrial potential in the W2 cells consistent with the onset of apoptosis. This response was also absent from the D3 cells.

In an effort to connect these results with the OSI measurements previously reported in Boustany et al. (72) and Zheng et al. (75), fluorescence multi-modal acquisition was also used to demonstrate that OSI decrease previously reported during the first 10-60 minutes of STS treatment is also localized to pixels spatially associated with the labeled mitochondria (Chapter 6).

7.2: IMPLICATIONS FOR FUTURE RESEARCH

Future work in this area should take two specific directions: (1) Augmenting the current prototype LCD-based setup, and (2) establishing that the optical morphometric responses observed in the iBMK cells are indeed resulting from mitochondrial fragmentation, and more generally, that this response is not only consistent with apoptosis but that it also arises exclusively (or nearly so) from apoptosis.

The LCD setup can be improved immediately with the addition of a microscope incubation system that allowed for maintenance of the cell specimen under physiological conditions. The Zeiss microscope currently includes a heated stage insert allowing for temperature control. However, the current system does not allow for humidity or atmosphere control. This necessitated the use of non-bicarbonate buffered medium, and for frequent replacement of medium and/or using a sealed chamber. A stage incubation system would alleviate both of these constraints, allow physiological bicarbonate buffered medium and humidity control. Additionally, if this system takes the form of a microscope flow chamber, then medium switching would be greatly facilitated.

The LCD-system can also be improved by implementing hardware triggering in the automation package. Currently all hardware is software-triggered, which introduces speed constraints from the computer processor's ability to effectively thread all of the commands

involved in controlling the software. A hardware trigger directly from the LCD to the camera would bypass the computer completely. This would allow the camera and LCD to operate in synchrony directly, and the speed would be limited only by the physical limitations of the devices, specifically the 60 Hz refresh rate of the LCD and the ~ 25 Hz readout rate of the Cascade CCD. In comparison, the nominal accusation speed of the LCD setup is currently ~ 7 Hz. Additionally, an automated stage integrated into the hardware control system would allow for much higher throughput acquisition and is highly recommended as well.

The second area of continued research involves future biological studies designed to rule out other non-apoptotic sources of the measured morphological dynamics of Chapter 4 and Chapter 5. Recent studies in the literature have linked Drp-1-mediated mitochondrial fission as downstream from and dependent on bax/bak colocalization to the mitochondrial outer membrane (36; 89). If true, the evidence in Chapter 5 combined with the results of Chapter 4 suggests that mitochondrial fission is the earliest morphological event after the cell's apoptotic fate is sealed. Future studies will be conducted in the iBMK cell system to determine with which structure(s) the dynamic responses are associated (as was done in Chapter 4) by using a suitable fluorescent label that does not result in photosensitization (Chapter 5). The differences in dynamics measured from the iBMK cells and BAEC (rise-then-drop of aspect ratio vs. drop in orientedness, respectively) will be closely studied and compared to determine common underlying dynamic associated with common structures. The work in this thesis supports this hypothesis in that the fission response is absent from bax/bak null cells (Chapter 4), and by extension, the optical dynamics measured can be used as a constitutive marker for apoptosis. However, it remains to be established unequivocally (i.e. by using the approach taken in Chapter 5 on iBMK cells) that this response is spatially

associated with the mitochondria in iBMK cells. It is recommended that a less invasive labeling method be employed (perhaps by transfection methods to generate stable iBMK cell lines expressing mito-GFP).

In the future, the work will also move to a more clinically relevant apoptosis inducer such as TNF- α instead of staurosporine. Instead of broad-acting metabolic disruption, TNF- α induces apoptosis through a specific and well-characterized t-BID-mediated pathway (99) which then leads to conformational activation of bax and its translocation to the mitochondrial outer membrane (100). Using this well-described pathway, it would potentially be easier to tease out information on the underlying molecular mechanisms and associate those with measured morphological changes.

7.3: LONG-TERM OUTLOOK

The goal of this work is to produce an apoptosis assay out of the optical methods and instruments described in this thesis. Because apoptosis is a dynamic process, this work studies the process over time in order to get a full time-dynamic response. This method has great potential in filling the need for a non-invasive time-sensitive probe for morphological changes, but in general requires validation in order to infer biological meaning. In the long-term, it is possible to repeat the study of Chapter 4 in several cell types under different conditions, and extract the common signatures spatially and temporally associated with mitochondrial fragmentation, allowing for the definition of the pure mitochondrial fragmentation responses. This could then be tested against unlabeled apoptotic cells. This pure signature could then be found embedded in the overall response. It would then be necessary to exclude all possible other sources for this type of optical signal (if any). Because

this measurement is time-dynamic, both the response and the timing of that response can be used to distill a unique apoptosis response out of the measurement.

Longer-term research will use the optical Gabor filter technique as an assay to measure apoptotic response in a clinically relevant context. One application for such an assay would be to determine the performance of different apoptosis inducing agents onto a tissue biopsy for drug screening and individualized medicine. To test the feasibility of such an application, we applied the same method to iBMK tumor tissue slices to demonstrate that enough signal can be obtained from a multilayered sample so as to apply the Gabor filtering method successfully.

The iBMK tumors were grown in SCID/NCR hairless mice (autosomal recessive nu/nu, NIH) to a diameter of ~ 1 cm subcutaneously. This work could not have been accomplished without the invaluable support of Kevin Bray and Dr. Eileen White (The Cancer Institute of New Jersey, New Brunswick, NJ, 08901, USA (CINJ)) for assistance in maintaining the mice, for tissue harvesting and for use of the CINJ vivarium. Tissue was harvested immediately after sacking and packed on ice in the same medium used for the iBMK cell growth (Chapter 5) and then transported to the optical measurements site ($t < 2$ h). Tissue slices were made by mounting double-sided tape (thickness = $75\text{ }\mu\text{m}$) on a no. 1, 22mm x 22 mm square coverslip (Fisher) and a 1 inch diameter round no. 2 coverslip (VWR) with double-sided tape placed in between to form a $75\text{ }\mu\text{m}$ thick channel open at both ends. Vacuum grease was used to seal the sides of the channel. A small sample of tumor is sandwiched by placing it in the channel and pressing the other coverslip onto it to achieve a uniform thickness. Optical study consisted the same filterbank with rotational resolution $0^\circ \leq \varphi < 180^\circ$ in 20° increments as before, and $S = 0.9\text{ }\mu\text{m}$. Calibration was achieved in the usual manner. Tissue samples were induced to undergo apoptosis by

replacing the medium of the sample with staurosporine (0.4 μM or 0.8 μM final concentration in viewing medium diluted from 4mM in DMSO) and time lapsed with the Gabor filterbanks.

Fig. 7-1 shows the results of the tissue time-lapse study on iBMK-W2 tumor tissue. Staurosporine induces a reduction in the orientedness of particles over the course of 3 hours, while a control with imaging medium supplemented with the same volume of DMSO only shows no such decrease in the same time span (**FIG. 7-1(a)**, **Fig. 7-1(b)**). Average orientedness across the field of view is measured and plotted every 10 minutes over time (**Fig. 7-1(c)**) and clearly shows a marked reduction in orientedness after 20 minutes for treated cells.

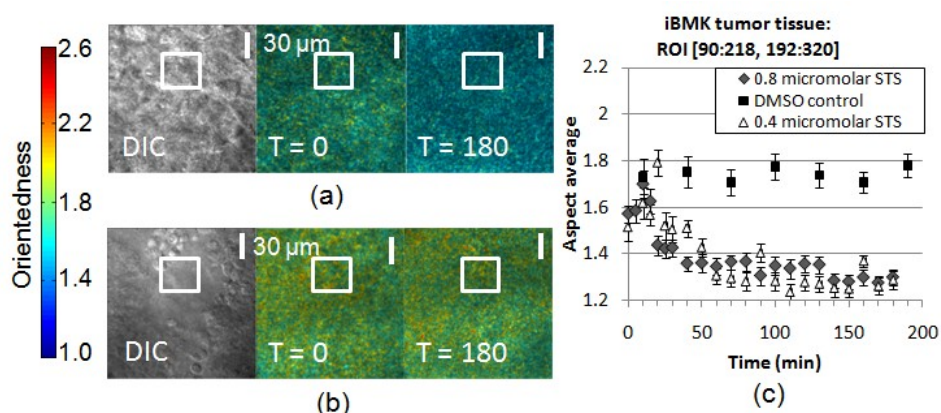


Fig. 7-1. iBMK-W2 tumor tissue studied with orientedness detection Gabor filter bank to detect effect of staurosporine in time lapse. A: DIC (T = 0 min.) and processed images (T = 0 min. and T = 180 min.) produced as in **Fig. 3-12**. For tissue exposed to 0.8 μM staurosporine (STS). B: For tissue exposed to DMSO only (no STS). C: Plot showing time dependency of particle orientedness for each of the three STS concentrations. Particle orientedness decreases when exposed to STS and does not when exposed to a control lacking STS.

The results of this preliminary study suggest that it is possible to measure dynamics from tissue samples, opening up avenues of application for the Gabor filtering method in the clinical setting. Once the setup has been optimized for rapid, high throughput acquisition, high screening for drug discovery and individualized medicine can be within

reach. However, it is once again emphasized that the optical measurement of subcellular dynamics cannot be interpreted directly without being applied in the context of other existing biologically specific assays. This technique therefore is not intended to supplant or replace any other described in Chapter 1. Rather, it is a useful screening tool that allows the user to discover differences in behavior amongst different specimens and/or treatments that can then be thoroughly probed with other methods.

Finally, in the future we will explore how advanced computational methods can be combined with our optical processing method to optimize the analysis of the scattering responses and establish the specific combinations of size, orientation and aspect ratio parameters that are unique to the biological processes under study. Ultimately, a cascade of classifiers can also be built to achieve increased detection performance and reduced computation time. The primary goal of using classification methods at this stage is to establish a robust training set that can be used to guide human-based analysis. Ultimately, future work in this area may be aimed at learning how to automatically differentiate different types of unknown unstained samples solely based on their Gabor filter responses.

REFERENCES

1. Kerr JFR, Wyllie AH, Currie AR. "Apoptosis: A Basic Biological Phenomenon with Wide-ranging Implications in Tissue Kinetics." *Br J Cancer*, 26(4): 239–257, (1972).
2. Chen Y, Zhao, X. "Shaping limbs by apoptosis." *Journal of Experimental Zoology*, 282(6) 691 – 702, (1998).
3. Norbury CJ, Hickson ID. "Cellular responses to DNA damage." *Annu Rev Pharmacol Toxicol* 41:367–401, (2001).
4. Danial NN, Korsmeyer SJ. "Cell death: critical control points." *Cell* 116, 205–19 (2004).
5. Suen D-F, Norris K-L, Youle, R-J. "Mitochondrial dynamics and apoptosis." *Genes & Dev.*, 22:1577-1590, (2008).
6. Karbowski M, Youle RJ, Melino G., Ed. "Dynamics of mitochondrial morphology in healthy cells and during apoptosis. *Cell Death and Differentiation* 10:870-880, (2003).
7. Detmer SA, Chan DC. "Functions and dysfunctions of mitochondrial dynamics." *Nature Rev. Mol. Cell Biol.* 8:870-879, (2007).
8. Yang J, Liu X, Bhalla K, Kim CN, Ibrado AM, Cai J, Peng T, Jones DP, Wang X. "Prevention of Apoptosis by Bcl-2: Release of Cytochrome c from Mitochondria Blocked." *Science* 275(5303): 1129 – 1132, (1997).
9. Karbowski M, Norris KL, Cleland MM, Jeong S-Y, Youle RJ. "Role of Bax and Bak in mitochondrial morphogenesis." *Nature* 443, 658-662 (2006).
10. Karbowski M, Arnoult D, Chen H, Chan DC, Smith CL, Youle RY. "Quantitation of mitochondrial dynamics by photolabeling of individual organelles shows that mitochondrial fusion is blocked during Bax activation of apoptosis." *J Cell Biol*, 164: 493-499 (2004).
11. Nagata, S. "Apoptosis by Death Factor." *Cell*, 88: 355-365, (1997).
12. Joza N. et al. Essential role of the mitochondrial apoptosis-inducing factor in programmed cell death. *Nature*, 410(6828):549-54, (2001).
13. Chao DT, Korsmeyer SJ. "BCL-2 family: regulators of cell death". *Annu. Rev. Immunol.* 16: 395–419, (1998).
14. Zamzami N, Brenner C, Marzo I, Susin SA, Kroemer G. "Subcellular and submitochondrial mode of action of Bcl-2-like oncoproteins". *Oncogene* 16 (17): 2265–82, (1998).
15. Adrain C, Creagh, EM, Martin SJ. "Apoptosis-associated release of Smac/DIABLO from mitochondria requires active caspases and is blocked by Bcl-2." *The EMBO Journal* , 20, 6627–6636, (2001).
16. Gaur U, Aggarwal BB. "Regulation of proliferation, survival and apoptosis by members of the TNF superfamily". *Biochem. Pharmacol.* 66 (8): 1403–8, (2003).
17. Degenhardt Km White E. "A mouse model system to genetically dissect the molecular mechanisms regulating tumorigenesis." *Clin. Cancer Res.*, 12(18): 5298-5304, (2006).

18. Savill J, Fadok V. "Corpse clearance defines the meaning of cell death." *Nature* 407:784–8, (2000).
19. Kurosaka K, Takahashi M, Watanabe N, Kobayashi Y. "Silent cleanup of very early apoptotic cells by macrophages." *J Immunol*, 171:4672–9, (2003).
20. Hacker G. "The morphology of apoptosis." *Cell Tissue Res*, 301:5–17, (2000).
21. Vander-Heiden, MG, Chandel NS, Williamson EK, Schumacker PT, Thompson CB. "Bcl-xL regulates the membrane potential and volume homeostasis of mitochondria." *Cell*. 91:627–637, (1997).
22. Martinou I, Desagher S, Eskes R, Antonsson B, Andre E, Fakan S, Martinou JC. "The release of cytochrome c from mitochondria during apoptosis of NGF-deprived sympathetic neurons is a reversible event." *J. Cell Biol.* 144:883–889, (1999).
23. Mootha VK, Wei MC, Buttle KF, Scorrano L, Panoutsakopoulou V, Mannella CA, Korsmeyer SJ. "A reversible component of mitochondrial respiratory dysfunction in apoptosis can be rescued by exogenous cytochrome C." *EMBO J.* 20:661–671, (2001).
24. Chan DC. "Mitochondrial fusion and fission in mammals." *Annu. Rev. Cell Dev. Biol.* 22, 79–99 (2006).
25. Frezza C, Cipolat S, Scorrano L. "Measuring mitochondrial shape changes and their consequences on mitochondrial involvement during apoptosis." *Methods in Molec. Biol.* 372, 405–420 (2007).
26. Camilleri-Broet S, Vanderwerff H, Caldwell E, Hockenbery D. "Distinct alterations in mitochondrial mass and function characterize different models of apoptosis." *Exp. Cell Res.* 239:277–292, (1998).
27. Scorrano L, Ashiya M, Buttle K, Weiler S, Oakes SA, Mannella CA, Korsmeyer SJ. "A distinct pathway remodels mitochondrial cristae and mobilizes cytochrome c during apoptosis." *Dev. Cell.* 2:55–67, (2002).
28. Olichon A, Baricault L, Gas N, Guillou E, Valette A, Belenguer P, Lenaers G. "Loss of OPA1 perturbs the mitochondrial inner membrane structure and integrity leading to cytochrome c release and apoptosis." *J Biol Chem* 278: 7743–7746, (2003).
29. Gonzalez F, Pariselli F, Jalmar O, Dupaigne P, Sureau F, Dellinger M, Hendrickson EA, Bernard S, Petit PX. "Mechanistic issues of the interaction of the hairpin-forming domain of tBid with mitochondrial cardiolipin." *PLoS One*; 5: e9342, (2010).
30. Gonzalez F, Pariselli F, Dupaigne P, Budihardjo I, Lutter M, Antonsson B, Diolez P, Manon S, Martinou JC, Goubert M, et al. "tBid interaction with cardiolipin primarily orchestrates mitochondrial dysfunctions and subsequently activates Bax and Bak." *Cell Death Differ*; 12: 614–626, (2005).
31. Frank S, Gaume B, Bergmann-Leitner E-S, Leitner WW, Robert EG, Catez F, Smith CL, Youle RJ. "The role of dynamin-related protein 1, a mediator of mitochondrial fission, in apoptosis." *Developmental Cell.* 1: 515–525, (2001).

32. Alirol E, Martinou J. "Mitochondria and cancer: is there a morphological connection?" *Oncogene*, 25:4706-4716, (2006).
33. Alirol E, James D, Huber D, Marchetto A, Vergani L, Martinou J, Scorrano L. "The mitochondrial fission protein hFis1 requires the endoplasmic reticulum gateway to induce apoptosis." *Mol Biol Cell*, 17: 4593–4605, (2006).
34. Jourdain A, Martinou JC. "Mitochondrial outer-membrane permeabilization and remodelling in apoptosis." *Internat. J. Biochem. Cell Biol.*, 41(10), 1884-1889, (2009).
35. Karbowski M, Lee Y-J, Gaume B, Jeong S-Y, Frank S, Nechushtan A, Santel A, Fuller M, Smith CL, Youle RJ. "Spatial and temporal association of Bax with mitochondrial fission sites. Drp1, and Mfn2 during apoptosis." *J Cell Biol*, 159: 931–938, (2002).
36. Wasiak S, Zunino R, McBride HM. "Bax/Bak promote sumoylation of DRP1 and its stable association with mitochondria during apoptotic cell death." *J Cell Biol*, 177: 439–450, (2007).
37. Cassidy-Stone A, Chipuk JE, Ingberman E, Song C, Yoo C, Kuwana T et al. "Chemical inhibition of the mitochondrial division dynamin reveals its role in Bax/Bak-dependent mitochondrial outer membrane permeabilization." *Dev. Cell* 14, 193–204 (2008).
38. Montessuit S, Somasekharan SP, Terrones O, Lucken-Ardjomande S, Herzig S, Schwarzenbacher R, Manstein DJ, Bossy-Wetzel E, Basanez G, Meda P, Martinou JC. "Membrane Remodeling Induced by the Dynamin-Related Protein Drp1 Stimulates Bax Oligomerization." *Cell* 142: 889–901 (2010).
39. Arnoult D, Rismanchi N, Grodet A, Roberts RG, Seeburg DP, Estaquier J et al. "Bax/Bak-dependent release of DDP/TIMM8a promotes Drp1-mediated mitochondrial fission and mitoptosis during programmed cell death." *Curr Biol* 15:2112–2118, (2005).
40. Arnoult D, Grodet A, Lee YJ, Estaquier J, Blackstone C. "Release of OPA1 during apoptosis participates in the rapid and complete release of cytochrome c and subsequent mitochondrial fragmentation." *J Biol Chem* 280:35742–35750, (2005).
41. Frezza C, Cipolat S, de Brito OM, Micaroni M, Bezoussenko GV, Rudka T, Bartoli D, Polishuck RS, Danial NN, De Strooper B, Scorrano L. "OPA1 Controls Apoptotic Cristae Remodeling Independently from Mitochondrial Fusion." *Cell*, 126(1): 177-189, (2006).
42. Baumeister W, Grimm R, Walz J. "Electron tomography of molecules and cells." *Trends Cell Biol.* 9(2), 81-85 (1999).
43. Perkins G, Frey TG. "Recent structural insights into mitochondria gained by microscopy." *Micron* 31, 97–111 (2000).
44. Mannella CA. "The relevance of mitochondrial membrane topology to mitochondrial function." *Biochim. et Biophys. Acta (BBA) – Molec. Basis of Disease*, 1762(2), 140-147 (2006).
45. Nicastro D, Frangakis AS, Typke D, Baumeister W. "Cryo-electron tomography of *Neurospora* mitochondria." *J. Struct. Biol.* 129, 48–56 (2000).
46. Martinez MM, Reif RD, Pappas D. "Detection of apoptosis: A review of conventional and novel techniques." *Anal. Methods*, 2, 996-1004 (2010).

47. Yasuhara S, Zhu Y, Matsui T, Tipirneni N, Yasuhara Y, Kaneki M, Rosenzweig A, Martyn JAJ. "Comparison of Comet Assay, Electron Microscopy, and Flow Cytometry for Detection of Apoptosis." *J. Histochem. and Cytochem.*, 51, 873-885 (2003).
48. Vermes I, Haanen C, Steffens-Nakken H, Reutelingsperger C. "A novel assay for apoptosis Flow cytometric detection of phosphatidylserine expression on early apoptotic cells using fluorescein labelled Annexin V." *J. Immunol. Meth.* 184(1), 39-51, (1995).
49. Bardales RH, Hailey LS, Xie SS, Schaefer RF, Hsu SM. "In situ apoptosis assay for the detection of early acute myocardial infarction." *Am. J. Pathol.*, 149(3), 821–829 (1996).
50. Grasl-Kraupp B, Ruttkay-Nedecky B, Koudelka H, Bukowska K, Bursch W, Schulte-Hermann R. "In situ detection of fragmented DNA (tunel assay) fails to discriminate among apoptosis, necrosis, and autolytic cell death: A cautionary note." *Hepatology*, 21(5): 1465-1468, (1995).
51. van Engeland M, Nieland LJW, Ramaekers FCS, Schutte B, Reutelingsperger CPM. "Annexin V-Affinity Assay: A Review on an Apoptosis Detection System Based on Phosphatidylserine Exposure." *Cytometry* 31:1–9 (1998).
52. Singh NP, McCoy MT, Tice RR, Schneider EL. "A simple technique for quantitation of low levels of DNA damage in individual cells." *Exper. Cell Res.*, 175(1): 184-191, (1988).
53. Roberg K. "Relocalization of Cathepsin D and Cytochrome c Early in Apoptosis Revealed by Immunoelectron Microscopy." *Lab. Invest.* 81, 149–158, (2001).
54. Dittrich W, Göhde W, "Flow-through Chamber for Photometers to Measure and Count Particles in a Dispersion Medium", U.S. patent #3761187, Filed Dec. 23, 1971, Issued Sep. 25, 1973. .
55. Rizzuto R, Brini M, Pizzo P, Murgia M, Pozzan T. "Chimeric green fluorescent protein as a tool for visualizing subcellular organelles in living cells." *Curr. Biol.* 5, 635-642 (1995).
56. -Tong JJ. "Mitochondrial Delivery Is Essential for Synaptic Potentiation." *Biol. Bull.* 212, 169-175. (2007).
57. Stack EC, Ferro JL, Kim J, del Signore SJ, Goodrich S, Matson S, Hunt BB, Cormier K, Smith K, MatsonWR, Ryu H, Ferrante RJ. "Therapeutic attenuation of mitochondrial dysfunction and oxidative stress in neurotoxin models of Parkinson's disease." *Biochimica et Biophysica Acta - Molec. Basis of Disease* 1782(3): 151-162, (2008).
58. Sprague BL, Pego RL, Stavreva DA, McNally JG. "Analysis of Binding Reactions by Fluorescence Recovery after Photobleaching." *Biophys. J.* 86(6), 3473-3495 (2004).
59. Zhou Z, Wong STC. "Informatics challenges of high-throughput microscopy." *IEEE Sig. Proces.* 23(3), 63-72 (2006).
60. Glory E, Murphy RF. "Automated Subcellular Location Determination and High-Throughput Microscopy." *Dev. Cell* 12(1), 7-16 (2007).
61. Heifetz A, Simpson JJ, Kong S-C, Taflove A, Backman V. "Subdiffraction optical resolution of a gold nanosphere located within the nanojet of a Mie-resonant dielectric microsphere." *Opt. Express* 15, 17334-17342 (2007).

62. Wilson JD, Foster TH. "Mie theory interpretations of light scattering from intact cells." *Opt. Lett.* 30(8), 2242-2244 (2005).
63. Wilson JD, Bigelow CE, Calkins DK, Foster TH. "Light Scattering from Intact Cells Reports Oxidative-Stress-Induced Mitochondrial Swelling." *Biophys. J.* 88(4), 2929-2938 (2005).
64. Schuele G, Vitkin E, Huie P, O'Connell-Rodwell C, Palanker D, Perelman LT. "Optical spectroscopy noninvasively monitors response of organelles to cellular stress." *J. Biomed. Opt.* 10, 051404 (2005).
65. Wilson JD, Giesselman BR, Mitra S, Foster TH. "Lysosome-damage-induced scattering changes coincide with release of cytochrome c." *Opt. Lett.* 32(17), 2517-2519 (2007).
66. Mourant JR, Johnson TM, Carpenter S, Guerra A, Aida T, Freyer JP. "Polarized angular dependent spectroscopy of epithelial cells and epithelial cell nuclei to determine the size scale of scattering structures," *J. Biomed. Opt.* 7(3), 378-387 (2002).
67. Huang D, Swanson EA, Lin CP, Schuman JS, Stinson WG, Chang W, Hee MR, Flotte T, Gregory K, Puliafito CA, Fujimoto JG. "Optical coherence tomography." *Science* 254, 1178-1181 (1991).
68. Drexler W, Fujimoto JG. "State-of-the-art retinal optical coherence tomography." *Prog. Retin. Eye Res.* 27(1), 45-88 (2008).
69. Mogensen M, Morsy HA, Thrane L, Jemec GBE. "Morphology and Epidermal Thickness of Normal Skin Imaged by Optical Coherence Tomography." *Dermat.* 217(1), 14-20 (2008).
70. Lam S, Standish B, Baldwin C, McWilliams A, leRiche J, Gazdar A, Vitkin AI, Yang V, Ikeda N, MacAulay C. "In vivo Optical Coherence Tomography Imaging of Preinvasive Bronchial Lesions." *Clin. Cancer. Res.* 14(7), 2006-2011 (2008).
71. Repka MX, Kraker RT, Tamkins SM, Suh DW, Sala NA, Beck RW. "Retinal Nerve Fiber Layer Thickness in Amblyopic Eyes." *Amer. J. Ophthal.*, In press (2009).
72. Boustany NN, Kuo SC, Thakor NV. "Optical scatter imaging: subcellular morphometry in situ with Fourier filtering." *Opt. Lett.* 26(14), 1063-1065 (2001). *Opt. Lett.*, pp. 26(14), 1063-1065.
73. Zheng J-Y, Tsai Y, Kadimcherla P, Zhang R, Shi J, Oyler GA, Boustany NN. "The C-Terminal Transmembrane Domain of BCL-xL Mediates Changes in Mitochondrial Morphology." *Biophys. J.* 94, 286-297 (2008).
74. Boustany NN, Tsai Y-C, Pfister B, Joiner WM, Oyler GA, Thakor NV. "BCL-xL-Dependent Light Scattering by Apoptotic Cells." *Biophys. J.*, 87(6), 4163-4171 (2004).
75. Zheng, J-Y. *Microscopy with Spatial Filtering for Monitoring Subcellular Morphology*. Doctoral dissertation, Rutgers University, New Brunswick, New Jersey, USA. (2009).
76. Bansal V, Patel S, Saggau P. "High-speed addressable confocal microscopy for functional imaging of cellular activity." *J. Biomed. Opt.*, 11, 034003 (2006).
77. Lu Y, Chen S. "Direct write of microlens array using digital projection photopolymerization." *Appl. Phys. Lett.* 92(4), 041109 (2008).

78. Zhoua W, Xua Q, Yua Y, Asundi A. "Phase-shifting in-line digital holography on a digital micro-mirror device." *Opt. and Las. Eng.*, 47(9), 896-901 (2009).
79. Zheng J-y, Pasternack RM, Boustany NN. "Optical Scatter Imaging with a digital micromirror device." *Optics Express*, 17(22): 204010-20414, (2009).
80. Pasternack RM, Qian Z, Zheng J-Y, Metaxas DN, White E, Boustany NN. "Measurement of subcellular texture by optical Gabor-like filtering with a digital micromirror device." *Opt. Lett.* 33, 2209-2211 (2008).
81. Fogel U, Sagi D. "Gabor filters as texture discriminator." *Biological Cybernetics* 61(2), 103-113, (1989).
82. Dunn D, Higgins WE, Wakeley J. "Texture segmentation using 2-D Gabor elementary functions," *IEEE Trans. Pattern Anal. Mach. Intell.* 16(2), 130–149, (1994).
83. Daugman JG. "Uncertainty relation for resolution in space, spatial frequency, and orientation optimized by two-dimensional visual cortical filters," in *J. Opt. Soc. Am.*, A2: 1160-1169, (1985).
84. Pasternack RM, Qian Z, Zheng J-Y, Metaxas D, Boustany, NN. "Highly sensitive size discrimination of sub-micron objects using optical Fourier processing based on two-dimensional Gabor filters." *Optics Express*, 17(14), 12001-12012, (2009).
85. Koopman WJH, Visch H-J, Smeitink JAN, Willems PHGM. "Simultaneous quantitative measurement and automated analysis of mitochondrial morphology, mass, potential, and motility in living human skin fibroblasts." *Cytometry Part A*, 69A(1), 1 - 12 (2006).
86. Songa W, Bossya B, Martina OJ, Hicksa A, Lubitza S, Knotta AB, Bossy-Wetzel E. "Assessing mitochondrial morphology and dynamics using fluorescence wide-field microscopy and 3D image processing." *Methods*, 46(4), 295-303 (2008).
87. Gerencsér ÁA, Doczi J, Töröcsik B, Bossy-Wetzel E, Adam-Vizi V. "Mitochondrial Swelling Measurement In Situ by Optimized Spatial Filtering: Astrocyte-Neuron Differences." *Biophys. J.*, 95(5), 2583-2598 (2008).
88. Wilson JD, Cottrell WJ, Foster TH. "Index-of-refraction-dependent subcellular light scattering observed with organelle-specific dyes." *J. Biomed. Opt.*, 12:014010, (2007).
89. Youle RJ, Karbowski M. "Mitochondrial fission in apoptosis." *Nat. Rev. Mol. Cell Biol.* 6, 657-663, (2005).
90. Rabin B, Pasternack R, Boustany N. "Automated Fourier microscopy with a liquid crystal device." In Preparation, (2011).
91. Pasternack RM, Zheng J-Y, Boustany NN. "Detection of mitochondrial fission with orientation-dependent optical Fourier filters", *Cytometry Part A*. 79A(2):137-148, (2011).
92. Pasternack RM, Rabin B, Zheng J, Boustany NN. "Quantifying subcellular dynamics in apoptotic cells with two-dimensional Gabor filters." *Biomed. Opt. Expr.* 1(2), 720-728 (2010).
93. Szabadkai G, Simoni A, Chami M, Wieckowski MR, Youle RJ, Rizutto R. "Drp-1-Dependent Division of the Mitochondrial Network Blocks Intraorganellar Ca²⁺ Waves and Protects against Ca²⁺ Mediated Apoptosis." *Molecular Cell*, 16: 59-68, (2004).

94. Boustany NN, Drezek R, Thakor NN. "Calcium-Induced Alterations in Mitochondrial Morphology Quantified in Situ with Optical Scatter Imaging." *Biophys. J.*, 83: 1691-1700, (2002).
95. Chalut KJ, Ostrander JH, Giacomelli MG, Wax A. "Light Scattering Measurements of Subcellular Structure Provide Noninvasive Early Detection of Chemotherapy-Induced Apoptosis." *Cancer Res.*, 69: 1199-1204, (2009).
96. Loud AV. "A quantitative stereological description of the ultrastructure of normal rat liver parenchymal cells." *J. Cell Biol.* 37, 27-46 (1968).
97. Pasternack RM, Zheng J-Y, Boustany NN. "Optical Scatter Changes at the Onset of Apoptosis Are Spatially Associated with Mitochondria", *J. Biomed. Opt. Lett.* 15, 040504; doi:10.1117/1.3467501, (2010).
98. Pasternack RM, Zheng J-Y, Qian Z, Zhou J, Metaxas DN, White E, Boustany NN. "Optical Processing of Cell and Tissue Structure", Workshop on Microscopic Image Analysis with Applications in Biology (MIAAB2009), NIH Campus, Bethesda, MD, Sep 3-4 2009.
99. Shore GC, Nguyen M. "Bcl-2 proteins and apoptosis: choose your partner." *Cell* 135: 1004–1006, (2008).
100. Perez D, White E. "TNF- α Signals Apoptosis through a Bid-Dependent Conformational Change in Bax that Is Inhibited by E1B 19K." *Molec Cell* 6(1)L 53-63, (2000).

CURRICULUM VITAE

Robert M Pasternack

EDUCATION:

- May 2007 **Rutgers University**, New Brunswick NJ, USA
Bachelor of Science in Biomedical Engineering: GPA 3.992/4.0
- May 2011 **Rutgers University**, New Brunswick, NJ, USA
Candidate for Ph. D. Biomedical Engineering
 - Develop an optical Fourier microscopy method based on Gabor filtering to non-invasively track real-time changes in particle morphology with sub-micron resolution in situ.

EXPERIENCE:

- 09/07-09/09 **Graduate Fellow**
Department of Biomedical Engineering, Rutgers University, Piscataway, NJ
- 01/08-01/09 **President**, BioEngineering Student Society
- 01/10-05/10 **Graduate Course Development (Optical Microscopy Laboratory Course (16:125:564, Rutgers) (2010))**, Developed lab manuals, ran lab sections
Department of Biomedical Engineering, Rutgers University, Piscataway, NJ

PEER-REVIEWED PUBLICATIONS:

1. **R.M. Pasternack**, J-Y. Zheng, N.N. Boustany, "Detection of mitochondrial fission with orientation-dependent optical Fourier filters", *Cytometry Part A*. 79A(2):137-148, doi: 10.1002/cyto.a.21011. (2011).
2. **R.M. Pasternack**, J-Y. Zheng, N.N. Boustany, "Optical Scatter Changes at the Onset of Apoptosis Are Spatially Associated with Mitochondria", *J. Biomed. Opt. Lett.* 15, 040504; doi:10.1117/1.3467501, (2010).
3. N.N. Boustany, **R.M. Pasternack**, J-Y. Zheng "Optical scatter microscopy based on two-dimensional Gabor filters", *Journal of Visualized Experiments*, <http://www.jove.com/index/details.stp?id=1915>, (2010)
4. J-Y. Zheng, **R.M. Pasternack**, N.N. Boustany, "Optical scatter imaging with a digital micromirror device", *Optics Express*, 17 (22), 20401-20414 (2009). doi:10.1364/OE.17.020401
5. **R.M. Pasternack**, Z. Qian, J-Y. Zheng, D.N. Metaxas, N.N. Boustany, " Highly sensitive size discrimination of submicron objects using optical Fourier filtering based on two dimensional Gabor filters", *Optics Express*, 17(14), 12001-12012 (2009). **On Aug. 7 2009, results of this article were featured on the Technical Insights, Sensor Technology Alert Services, of the Frost & Sullivan Website.** doi:10.1364/OE.17.01200
6. **R.M. Pasternack**, Z. Qian, J-Y. Zheng, D.N. Metaxas, E. White, N.N. Boustany, " Measurement of Subcellular Texture by Optical Gabor-Like Filtering with a Digital Micromirror Device", *Optics Letters*, 33(19), 2209-2211 (2008). Erratum in *Optics Letters*, 34(13), 1939 (2009). **This article was selected for the Nov. 1 2008 issue of Virtual Journal of Biological Physics Research, and for the Dec. 2008 issue (Vol 3 Issue 12) of The Virtual Journal for Biomedical Optics.** doi:10.1364/OL.33.002209, erratum doi:10.1364/OL.34.001939